



University of Cagliari  
Department of Mathematics and Computer Science

---

# *Numerical treatment for inverse problems in applied Geophysics*

PhD Course in Mathematics and Computer Science

PhD Coordinator: Giuseppe Rodriguez

SDS: MAT/08 Numerical Analysis

Ciclo XXIX

## **Author**

Patricia Díaz de Alba

## **Supervisors**

Giuseppe Rodriguez  
Luisa Fermo

Academic year 2015 – 2016  
Thesis defence March – April, 2017

---

*“The enchanting charms of this sublime science, mathematics, reveal only to those who have the courage to go deeply into it”.*

Carl Friedrich Gauss



# Acknowledgements

First of all, I would like to offer my special thanks to Prof. Giuseppe Rodriguez, my research supervisor, for his patient guidance, enthusiastic encouragement and useful critiques of this research work. You made me feel like home from the first day. It wouldn't have been the same without you.

I also would like to express my deep gratitude to Dr. Luisa Fermo not only for her advice and constructive suggestions during the planning and development of this work, but also for being there when I really needed her. You are more than a colleague, you are a friend.

My grateful thanks are also extended to Prof. James Nagy, who was my supervisor for three months in Atlanta (USA), for his help and his recommendations.

I wish to acknowledge the staff of *Centro di Ricerca, Sviluppo e Studi Superiori in Sardegna (CRS4)* for enabling me to work in their offices.

I am extremely grateful for the support given by the whole department of Viale Merello, specially Giuseppe Vigliano, considering me as a part of their group, and for being part of my family in Cagliari. Thanks to all of you for giving me this opportunity. You made this experience a wonderful one.

Finally, but not less important, I want to thank my parents, my sister, my brother-in-law, my dog Roby (I know he's with me), and my whole family because I couldn't get my PhD without their support and encouragement. Also Celia, Cristina and Belén because they are part of my family and they have been by my side for many years. Anna N., Arianna, Mario, Alba, Edu, Anto, Giulia, Marina, Anna C., Chicchi, Teresa, Ale and Tommy for all and every moment we spent together because I couldn't imagine my stay in Cagliari without you...

My thanks are also to all the people I met during these 3 years, specially to the people I met in Atlanta; sometimes you "click" with some people even if you have been getting to know them for a little. I hope to have all of you in my life for a long time.

Thank you very much. This work is also yours.



# Contents

<b>List of Figures</b>	<b>ix</b>
<b>List of Tables</b>	<b>xiii</b>
<b>List of Symbols</b>	<b>xv</b>
<b>Introduction, motivation and overall objectives</b>	<b>1</b>
<b>1 Some necessary preparatory tools</b>	<b>5</b>
1.1 Ill-posed problems . . . . .	5
1.1.1 Linear least squares problem . . . . .	7
1.1.2 Nonlinear least squares problem . . . . .	9
1.2 SVD and Generalized SVD . . . . .	12
1.2.1 The Singular Value Decomposition . . . . .	12
1.2.2 The Generalized Singular Value Decomposition . . . . .	13
1.3 Regularization Methods . . . . .	14
1.3.1 The Tikhonov Regularization . . . . .	15
1.3.2 TSVD and TGSVD . . . . .	16
1.3.3 Total Variation regularization . . . . .	17
1.3.4 Choosing the regularization parameter . . . . .	17
<b>2 Linear model for frequency domain electromagnetic (FDEM) data inversion</b>	<b>23</b>
2.1 The linear model . . . . .	24
2.2 Numerical methods for the solution of the inverse problem	25
2.2.1 Approximation by a piecewise constant function . . . . .	26
2.2.2 Approximation by a linear spline . . . . .	28
2.2.3 Truncation error . . . . .	30
2.3 Numerical results . . . . .	31
<b>3 Nonlinear model for frequency domain electromagnetic (FDEM) data inversion</b>	<b>41</b>
3.1 The nonlinear model . . . . .	42
3.2 The inverse problem . . . . .	44
3.2.1 Computing the Jacobian matrix . . . . .	48

3.3	Software implementation . . . . .	51
3.4	Numerical results . . . . .	52
<b>4</b>	<b>Time domain electromagnetic (TDEM) response of a conductive permeable sphere</b>	<b>67</b>
4.1	Setting of the problem . . . . .	68
4.2	A nonlinear approximation problem . . . . .	72
4.3	Some numerical results . . . . .	77
	<b>Summary conclusion and further work</b>	<b>81</b>
	<b>Bibliography</b>	<b>83</b>

## List of Figures

1.1	Representation of the GCV function and its minimum for the Tikhonov regularization on the left-hand side and for the TSVD on the right-hand side. . . . .	19
1.2	Representation of the L-curve and its corner. . . . .	20
1.3	L-curve for some real experiments. . . . .	20
2.1	The sensitivity functions $\phi^V$ and $\phi^H$ . . . . .	25
2.2	Test function used to model conductivity with respect to depth in S/m. . . . .	31
2.3	Representation of the TSVD (left-hand side) and Tikhonov (right-hand side) solutions for different choices of the regularization parameter and for $n = 40$ , $m = 20$ , a noise level $\zeta = 10^{-4}$ and an approximation of $\sigma$ by a spline of order 1. The second row is a zoom of the plots of the first row. . . .	33
2.4	Best solutions for the conductivity for $n = 40$ , $m = 20$ , a noise level $\zeta = 10^{-4}$ , and an approximation of $\sigma$ by a spline of order 1. . . . .	34
2.5	Representation of the TSVD (left-hand side) and Tikhonov (right-hand side) solutions for different choices of the regularization parameter and for $n = 40$ , $m = 20$ , a noise level $\zeta = 10^{-4}$ and an approximation of $\sigma$ by a spline of order 2. The second row is a zoom of the plots of the first row. . . .	34
2.6	Best solutions for the conductivity for $n = 40$ , $m = 20$ , a noise level $\zeta = 10^{-4}$ , and an approximation of $\sigma$ by a spline of order 2. The second row is a zoom of the plots of the first row. . . . .	35
2.7	Representation of the TSVD (left-hand side) and Tikhonov (right-hand side) solutions for different choices of the regularization parameter and for $n = 40$ , $m = 20$ , a noise level $\zeta = 10^{-2}$ and an approximation of $\sigma$ by a spline of order 1. The second row is a zoom of the plots of the first row. . . .	35

2.8	Best solutions for the conductivity for $n = 40$ , $m = 20$ , a noise level $\zeta = 10^{-2}$ , and an approximation of $\sigma$ by a spline of order 1. The second row is a zoom of the plots of the first row. . . . .	36
2.9	On the left side, the data vector $\mathbf{M}$ as from the linear system (2.6) (with $n = 40$ ; $m = 20$ ), compared against the corresponding approximation calculated by using the Gauss-Kronrod quadrature for the profile of $\sigma(z) = e^{-(z-1)^2}$ in Fig. 2.2. On the right side, the same comparison for the profile of $\sigma(z) = e^{-(z-1)^2} + 1$ . . . . .	37
2.10	Profile of $\sigma$ with maximal value 100 mS/m and the representation of the data obtained by the nonlinear model and the linear model for $n = 80$ , $m = 20$ and the magnetic permeability equal to the one of the free space. . . . .	38
2.11	Profile of $\sigma$ with maximal value $2 \cdot 10^4$ mS/m and the synthetic data obtained by the nonlinear and the linear models for $n = 80$ , $m = 20$ and the magnetic permeability the one of the free space. . . . .	38
2.12	Profile of $\sigma$ with maximal value $2 \cdot 10^4$ mS/m and the representation of the data obtained by the nonlinear model and the linear model for $n = 80$ , $m = 20$ and the magnetic permeability equal to $\mu = \sigma\mu_0$ . . . . .	39
3.1	Discretization and representation of the subsol. . . . .	42
3.2	Graphical user interface using GUIDE, the graphical user interface development environment of Matlab. . . . .	52
3.3	Graph of the test function used to model conductivity with respect to depth. . . . .	53
3.4	Plot of the first 4 regularized solutions, computed by minimizing the real part of the signal, compared to the exact solution. The magnetic permeability $\mu = \mu_0$ is constant, the noise level is $\zeta = 10^{-3}$ . . . . .	56
3.5	Solution obtained by minimizing the real part of the data (left) or the imaginary part (right); $\zeta = 10^{-3}$ , $\mu_r = 10$ in the top row, $\mu_r = 10^2$ in the bottom row. The value of $\ell$ is chosen either optimally or by the L-curve. . . . .	57

3.6	Average of the singular values of the Jacobian $J(\boldsymbol{\mu})$ computed on 100 random points in $\mathbb{R}^n$ , for $m = n = 10, 20, 30, 40$ (left-hand side); each component of $\boldsymbol{\mu}$ is in $[\mu_0, 100\mu_0]$ . The right-hand side graph shows the average singular values for $n = 20$ together with their maximum and minimum value across the random tests. . . . .	58
3.7	Average of the singular values of the Jacobian $J(\boldsymbol{\mu})$ computed on 100 random points in $\mathbb{R}^n$ , for $m = n = 20$ ; each component of $\boldsymbol{\mu}$ is in $[\mu_0, \mu_r\mu_0]$ , with $\mu_r = 10, 10^2, 10^3, 10^4$ . . . . .	59
3.8	Efficiency in the evaluation of the Jacobian $J$ of size $n = 10, 20, \dots, 100$ , compared to a finite difference approximation. The left-hand side graph displays the computing time in seconds for the two approaches; the right-hand side graph reports the speedup factor, i.e., the ratio between the timings of finite difference and the exact Jacobian. . . . .	60
3.9	The “spy plot” on the left shows the pattern of the nonzero elements for the Jacobian $J$ of size $40 \times 20$ , as computed by the formulas in Section 3.2.1. The central graph displays the same information for $\tilde{J}$ , obtained by the approximation (3.16). The right-hand side plot represents the relative error for the first two singular values with respect to the variation of $\delta$ in (3.16). . . . .	61
3.10	Regularized solution obtained by fixing $\theta = 2$ , $m_h = 10$ , $m_\omega = 1$ , $n = 40$ , and $\xi = 10^{-3}$ . On the left, the result obtained by inverting the in-phase component of the data; on the right, the solution corresponding to the quadrature component. . . . .	63
3.11	Measured (circles) and predicted (asterisks) data values for the two solutions displayed in Fig. 3.10; we display the data for both the vertical and the horizontal orientation of the device. The graphs on the left are obtained by inverting the in-phase component of the measured signal; the graphs on the right correspond to the quadrature component. . . . .	63
3.12	Regularized solution obtained by fixing $\theta = 20$ , $m_h = 20$ , $m_\omega = 1$ , $n = 40$ , and $\xi = 10^{-3}$ . On the left, the result obtained by inverting the in-phase component of the data; on the right, the solution corresponding to the quadrature component. . . . .	64

3.13	Regularized solution obtained by fixing $\theta = 20$ , $m_h = 1$ , $m_\omega = 6$ , $n = 40$ , and $\zeta = 10^{-3}$ . On the left, the result obtained by inverting the in-phase component of the data; on the right, the solution corresponding to the quadrature component. . . . .	65
4.1	The coordinate system for the conducting sphere. . . . .	68
4.2	The behavior of the sum $h(t)$ for different materials for $N = 10$ . . . . .	73
4.3	The behavior of the sum $h(t)$ for different materials for $N = 100$ . . . . .	74
4.4	The behavior of the sum as function of $N$ for different materials at $t = 2 \times 10^{-6}$ . . . . .	74
4.5	Plot of $f(x) = \tan x$ (blue line) and $g(x) = \frac{(\mu_r - 1)x}{(\mu_r - 1) + x^2}$ for $\mu_r - 1 = 1, 10, 50$ (pink, yellow and green lines, respectively). . . . .	78
4.6	$\delta_n$ as a function of $n$ and parametrically as a function of the relative permeability $\mu_r$ . . . . .	79
4.7	The singular values of the involved matrices. . . . .	80

## List of Tables

2.1	Best errors attainable by the method for selected choices of the regularization parameter applying the TSVD and the Tikhonov regularization, and for an approximation of the solution by a spline of order 1. Profile for $\sigma$ depicted in Fig. 2.2.	32
2.2	Best errors attainable by the method for selected choices of the regularization parameter applying the TSVD and the Tikhonov regularization, and for an approximation of the solution by a spline of order 2. Profile for $\sigma$ depicted in Fig. 2.2.	32
3.1	Best accuracy attainable by the method for both the real part, $\mathcal{R}$ , and the imaginary part, $\mathcal{I}$ , of the signal and for selected choices of the parameters. Each entry of the table is the average of $E_{\ell_{\text{opt}}}$ across 40 experiments, with two noise levels and 20 noise realizations.	54
3.2	Results for different values of the relative magnetic permeability $\mu_r$ . Each row displays the average error and the number of <i>failures</i> across 40 experiments; see text. The upper block concerns the optimal choice of $\ell$ , the bottom block the choice by the L-curve.	55
4.1	Electrical conductivity $\sigma$ and magnetic permeability $\mu$ of some metallic materials.	73
4.2	Comparison of the exact $d_n$ and its approximation $\tilde{d}_n$ , and the corresponding relative error $\epsilon_n$ for $N = 10$ .	79



# List of Symbols

The next list describes several symbols that will be later used within this thesis.

## Mathematical Symbols

$\mathbf{e}$	Noise vector
$\mathbf{r}(\mathbf{x})$	Residual function
$\delta$	Regularization parameter for Tikhonov
$\ell$	Truncation parameter for TSVD
$\mathcal{N}(A)$	Kernel of $A$
$\nabla$	Gradient
$\ \cdot\ $	Euclidean norm
$\partial$	Partial derivative
$\Sigma$	Diagonal matrix of singular values
$\tau$	User-supplied constant for the Discrepancy Principle
$\mathbf{u}_i$	Left singular vector
$\mathbf{v}_i$	Right singular vector
$\widehat{I}_n, I_n$	Modified spherical and modified Bessel functions of the first kind
$\widehat{K}_n, K_n$	Modified spherical and modified Bessel functions of the second kind
$\zeta$	Noise level
$A^\dagger$	Moore–Penrose pseudoinverse
$A^T$	$A$ transpose
$a_i$	Singular values of the matrix $A$

$J$	Jacobian matrix
$J_s$	Bessel functions of the first kind of order $s$
$P_n$	Legendre polynomials of degree $n$
$U$	Matrix of left singular values
$V$	Matrix of right singular values

### **Physics Symbols**

$[F]_z$	Magnetic potential vector (A/m)
$\chi(s)$	Induced magnetic dipole moment factor (dimensionless)
$\epsilon$	Dielectric constant (F/m)
$\gamma$	Propagation constant (dimensionless)
$\mu$	Magnetic permeability (H/m)
$\mu_0$	Magnetic permeability of free space (H/m)
$\mu_r$	Relative magnetic permeability (H/m)
$\omega$	Angular frequency ( $s^{-1}$ )
$\sigma$	Electrical conductivity (S/m)
$d_k$	Thickness of each layer of the subsoil (m)
$H$	Uniform magnetic field (A/m)
$h$	Heights above the ground (m)
$H_0$	Intensity of the magnetic field (A/m)
$M_\nu$	Apparent conductivity of orientation $\nu$ (S/m)
$\rho$	Distance between the coils of the GCM (m)
$r_e$	Distance between the center of the sphere and the point $P$ (m)
$r_s$	Radius of the sphere (m)

*Dedicated to the people who have always supported me...*

---

# Introduction, motivation and overall objectives

This thesis is concerned with numerical methods for inverse problems in applied Geophysics<sup>1</sup>. Its main purpose is to reconstruct the electrical conductivity and the magnetic permeability of the soil by *Electromagnetic induction* (EMI).

Electromagnetic induction is an established, noninvasive technique for measuring the apparent electrical conductivity of soils and has been used to characterize the spatial variability of soil properties since the late 1970s. Initially used to assess soil salinity, the use of EMI in soil studies has expanded to include hydrological and hydrogeological characterizations [43, 52, 63], hazardous waste characterization studies [24, 45], precision–agriculture applications [6, 21, 84], archaeological surveys [42, 50, 68], geotechnical investigations [53] and unexploded ordnance (UXO) detection [36, 37, 66].

In all cases the soil property being investigated must influence soil apparent electrical conductivity either directly or indirectly for EMI techniques to be effective. An increasing number and diversity of EMI sensors have been developed in response to users' needs and the availability of allied technologies, which have greatly improved the functionality of these tools. EMI investigations provide several benefits for soil studies, for instance, the large amount of georeferenced data that can be rapidly and inexpensively collected with EMI providing more complete characterization of the spatial variations in soil properties than traditional sampling techniques. EMI theory and foundations of measurement systems are described in the applied geophysics literature [46, 67, 81]. In addition, compared to traditional soil survey methods, EMI can more effectively characterize diffuse soil boundaries and identify areas of dissimilar soils within mapped soil units, giving soil scientists greater confidence when collecting spatial soil information. EMI techniques do have limitations as their efficacy highly depends on the complex interactions among multiple and variable soil properties. Despite this, EMI techniques are increasingly being used to investigate the spatial

---

<sup>1</sup>Subject of natural science concerned with the physical processes and physical properties of the Earth and its surrounding space environment, and the use of quantitative methods for their analysis.

variability of soil properties at field and landscape scales.

The main device used for this kind of techniques is the *Ground Conductivity Meter* (GCM). It contains two coils (a transmitter and a receiver) placed at a fixed distance. An alternating sinusoidal current in the transmitter produces a primary magnetic field, which induces small eddy currents in the subsurface. These currents produce a secondary magnetic field, which is sensed by the receiver. A meter that senses the voltage across this coil is calibrated in units of milliSiemens per meter. The ratio of the secondary to the primary magnetic fields is then used, along with the instrumental parameters, to estimate electrical properties of the subsurface. It can be used on the ground or at heights above the ground; at greater heights, the instrument is less sensitive to electrical conductivity at greater depths. Thus by taking measurements at several heights, we can gain information about the depth profile of electrical conductivity. The orientation of the coils also affects the response of the instrument to variations in the soil electrical conductivity profile. Therefore, by holding the instrument so that the coils are in vertical or horizontal positions, we can gain additional information about the electrical conductivity profile.

Nevertheless, the noninvasive determination of electrical conductivity depth profiles, using a finite number of noisy aboveground electromagnetic induction measurements, remains difficult since it is an inverse problem. In the last two decades, the field of *inverse problems* has certainly been one of the fastest growing areas in applied mathematics. This growth has largely been driven by the needs of applications both in other sciences and in industry.

The aim of collecting data is to gain meaningful information about a physical system or phenomenon of interest. However, in many situations the quantities that we wish to determine are different from those we are able to measure, or have measured. If the measured data depends, in some way, on the quantities we want, then the data at least contains some information about those quantities. Starting with the data that we have measured, the problem of trying to reconstruct the quantities that we really want is called an inverse problem. Loosely speaking, we often say an inverse problem is where we measure an effect and want to determine the cause. Some typical inverse problems also arise in other different applications:

- **Deblurring Images** [31]. When we use a camera, we want the recorded image to be a faithful representation of the scene that we see. Thus, image deblurring is fundamental in making pictures sharp and useful. A digital image is composed of picture elements called *pixels*. Each pixel is assigned an intensity, mean to characterize the color

---

of a small rectangular segment of the scene. Some blurring always arises in the recording of a digital image, because of the unavoidable presence of noise. For example, the optical system in a camera lens may be out of focus, so that the incoming light is smeared out.

In image deblurring, we seek to recover the original, sharp image by using a mathematical model of the deblurring process.

- **Radio–astronomical imaging.** When using a multi–element interferometer as a radio telescope, it turns out that the measured data is not the distribution of radio sources in the sky (called the “sky brightness” function) but is rather the Fourier transform of the sky brightness. It is not possible to measure the entire Fourier transform spectrum, but only a limited range. From that limited piece of information (even disregarding the inherent noise), how is it possible to reconstruct the desired sky brightness?
- **Navigation.** When travelling in a boat or plane, it is useful to have an idea of the current location in close to real time. This is often done by making a variety of measurements, for example by using bearings to landmarks, stellar or satellite positions, and also by considering one’s previous position and using information such as records of speed and heading. How should all of these separate pieces of information be combined together to give a coherent description of the vessel’s motion?

Inverse problems typically lead to mathematical models that are not well–posed in the sense of Hadamard [25], i.e., to *ill–posed problems*. This means especially that their solution is unstable under data perturbations. Numerical methods that can cope with this problem are the so–called *Regularization methods*. For linear problems, this theory can be considered to be relatively complete and we will study a linear case in Chapter. 2. For nonlinear problems, the theory is, so far, developed to a much lesser extent. We will see an example in Chapter. 3.

This thesis reports distinct algorithms and techniques to overpass these difficulties since mathematical problems having these undesirable properties pose severe numerical adversities.

Along the thesis we present some cases that involve the solution of ill–conditioned problems for reconstructing the electrical conductivity and the magnetic permeability of the soil, and we propose for each of these problems an inversion procedure to get a good approximation of the solution.

The structure of this thesis is the following:

Chapter 1 introduces some preliminary notions which will be useful for the rest of the thesis. We remind the definition of ill-posed problems, and we describe some numerical tools, iterative methods and regularization methods.

Chapter 2 studies a linear ill-posed problem for recovering the electrical conductivity through an inversion procedure based on an approximation of the solution by means of both first and second order B-splines.

Chapter 3 presents a nonlinear ill-posed problem and we find the approximation of the electrical conductivity and the magnetic permeability of the soil by a regularized inversion procedure applying the Gauss-Newton method, and the Truncated Singular Value Decomposition and the Generalized Truncated Singular Decomposition. In addition, we are working on a graphical user interface (GUI) using GUIDE, the graphical user interface development environment of Matlab.

Chapter 4 describes the problem of a sphere under the influence of an electromagnetic field. We try to estimate the radius of the sphere and both its electrical conductivity and magnetic permeability via exponential sums.

# Some necessary preparatory tools **1**

In this chapter we present a brief introduction to discrete ill-posed problems. Specifically, we introduce some numerical tools such as the Singular Value Decomposition (SVD) and the Generalized Singular Value Decomposition (GSVD), and we also discuss some iterative methods as the Newton method and the Gauss–Newton method. Moreover, we will describe the Tikhonov regularization, the Truncated Singular Value Decomposition (TSVD) and the Truncated Generalized Singular Value Decomposition (TGSVD) as regularization methods.

A more complete information of these aspects is given in [28].

## 1.1 Ill-posed problems

Let us consider the following problem: Finding  $\mathbf{x}$  such that

$$F(\mathbf{x}, \mathbf{d}) = 0, \quad (1.1)$$

where  $\mathbf{d}$  is a data set from which the solution depends on, and  $F$  is the functional relation between  $\mathbf{x}$  and  $\mathbf{d}$ . Typically, problem (1.1) is called *direct problem* if  $F$  and  $\mathbf{x}$  are known and  $\mathbf{d}$  is unknown. Whereas (1.1) is called *inverse problem* if  $F$  and  $\mathbf{d}$  are known and  $\mathbf{x}$  is unknown.

In 1923, Jacques Hadamard [25] defined the inverse problem (1.1) to be *well-posed* if

- The solution exists.
- The solution is unique.
- The solution's behavior changes continuously with the initial conditions. More precisely, if we consider the following problem

$$F(\mathbf{x} + \delta\mathbf{x}, \mathbf{d} + \delta\mathbf{d}) = 0,$$

where  $\delta \mathbf{d}$  is the perturbation of the data  $\mathbf{d}$  and  $\delta \mathbf{x}$  is the resulting perturbation of the solution  $\mathbf{x}$ , then

$$\exists \eta_0 = \eta_0(\mathbf{d}) > 0, \quad \exists K_0 = K_0(\mathbf{d}) > 0 \quad \text{s.t.}$$

$$\text{if } \|\delta \mathbf{d}\| \leq \eta_0 \quad \text{then} \quad \|\delta \mathbf{x}\| \leq K_0 \|\delta \mathbf{d}\|.$$

Problems for which at least one of the properties above is not true, are termed *ill-posed*.

Inverse problems are often ill-posed. For example, the inverse heat equation, according to a formulation dating to Hadamard, must be ill-posed in  $L^2(\mathbb{R})$ , since solutions do not exist for all data. Moreover, even if the initial data is smooth enough that a solution exists for all data, there is no continuous dependence on it. An arbitrarily small perturbation of the initial data will preclude the existence of a solution for any data. In a word, the backward heat equation is ill-posed because all solutions are instantly swamped by high-frequency noise. Another example of ill-posed problem is Fredholm integral equation of the first kind<sup>1</sup> which is an integral equation in which the unknown function only appear under the integral sign.

Continuous models must often be discretized in order to obtain a numerical solution. While solutions may be continuous with respect to the initial conditions, they may suffer from numerical instability when solved with finite precision, or with errors in the data. Even if a problem is well-posed, it may still be *ill-conditioned*, meaning that a small error in the initial data can result in much larger errors in the answers. An ill-conditioned problem is indicated by a large condition number [28].

If the problem is well-posed, then it stands a good chance of solution on a computer using a stable algorithm. If it is not, it needs to be re-formulated for numerical treatment including *a priori* information concerning the expected solution, such as smoothness properties or the presence of blocky structures. This process is known as *regularization* and we will study some regularization methods in Section 1.3.

Theoretically, to be ill-posed the problem must be infinite dimensional. However, there are some finite dimensional discrete problems which have

---

<sup>1</sup>Fredholm integral equation is defined by

$$\int_a^b K(x, y)\varphi(y)dy = f(x), \quad x \in [a, b],$$

in which  $\varphi$  is the unknown, and the so-called kernel  $K$  and the right-hand side  $f$  are given functions.

similar properties like being highly sensitive to high-frequency perturbations. They are called *discrete ill-posed problems*.

We can distinguish between a linear system of equations or a nonlinear system of equations depending on the operator of the problem, that is

$$F(\mathbf{x}) = \mathbf{b}, \quad \mathbf{x} \in \mathbb{R}^n, \quad \mathbf{b} \in \mathbb{R}^m,$$

where  $F$  can be either a linear or a nonlinear operator. Since now on the finite dimensional problem is studied.

There are many possible ways of defining a “practical solution” to the original problem. A choice which leads to a simple computational problem is to let  $\mathbf{x}$  be a solution to the minimization linear problem

$$\min_{\mathbf{x}} \|F(\mathbf{x}) - \mathbf{b}\|, \quad (1.2)$$

where  $\|\cdot\|$  represents the Euclidean norm and  $\mathbf{r}(\mathbf{x}) = F(\mathbf{x}) - \mathbf{b}$  is called the *residual*. We call (1.2) a *least squares problem*.

### 1.1.1 Linear least squares problem

Suppose  $A\mathbf{x} = \mathbf{b}$  where  $A$  is a  $m \times n$  matrix,  $\mathbf{b} \in \mathbb{R}^m$  and  $\mathbf{x} \in \mathbb{R}^n$ . For simplicity, we assume  $A$  to be full-rank.

In the case in which  $m > n$ , there are more constraints than unknowns, and the system is *overdetermined* with no solutions (except for degenerate cases). We can find a least-squares solution that minimizes the error  $A\mathbf{x} - \mathbf{b}$ , i.e. we want to find  $\mathbf{x}$  that minimizes

$$\|A\mathbf{x} - \mathbf{b}\|^2$$

or

$$(A\mathbf{x} - \mathbf{b})^T(A\mathbf{x} - \mathbf{b})$$

or

$$\mathbf{x}^T A^T A \mathbf{x} - \mathbf{x}^T A^T \mathbf{b} - \mathbf{b}^T A \mathbf{x} + \mathbf{b}^T \mathbf{b}.$$

Differentiating w.r.t  $\mathbf{x}$  and setting the result equal to zero yields

$$2A^T A \mathbf{x} - 2A^T \mathbf{b} = 0,$$

from which we deduce that the solution is given by

$$\mathbf{x} = (A^T A)^{-1} A^T \mathbf{b},$$

where  $(A^T A)^{-1} A^T = A^\dagger$  is the *Moore–Penrose pseudoinverse* of  $A$  [2].

Assuming that  $m < n$ , we have fewer constraints than unknowns, and the system is *underdetermined* with an infinite number of solutions. A classical way to introduce unicity is to select the minimum norm solution. That is we will minimize  $\|\mathbf{x}\|$  subject to the constraint  $\mathbf{b} = A\mathbf{x}$ . The method of Lagrange multipliers let us add a term to the quantity to be minimized:

$$\|\mathbf{x}\|^2 + \lambda^T(\mathbf{b} - A\mathbf{x}),$$

where  $\lambda \in \mathbb{R}^n$  is a vector of parameters. Differentiating w.r.t  $\mathbf{x}$  and setting the result equal to zero yields

$$2\mathbf{x} - A^T\lambda = 0.$$

We cannot just solve for  $\lambda$  since  $A$  is not a square matrix, but we can premultiply by  $A$  to obtain

$$2A\mathbf{x} - AA^T\lambda = 0,$$

and using  $\mathbf{b} = A\mathbf{x}$  gives us

$$2\mathbf{b} = AA^T\lambda,$$

so

$$\lambda = 2(AA^T)^{-1}\mathbf{b}$$

and hence

$$\mathbf{x} = A^T(AA^T)^{-1}\mathbf{b}.$$

If  $m = n$  and  $A$  is nonsingular, the solution of (1.2) is simply  $\mathbf{x} = A^{-1}\mathbf{b}$ . Linear least squares problems are discrete ill-posed problems if:

- The singular values of  $A$  decay gradually to zero.
- The ratio between the largest and the smallest nonzero singular values of  $A$  is large.

The ill-conditioning of the matrix  $A$  does not mean that an approximate solution cannot be computed. It implies that some classical numerical methods for linear systems, such as LU, Cholesky or QR factorization [2] cannot be used to solve (1.2) since these basic and all-purpose methods suffer from high instability in such ill-discrete ill-posed problems due to the “unbounded inversion” of the vanishing eigenvalues of  $A^T A$  or  $AA^T$ .

### 1.1.2 Nonlinear least squares problem

All the methods for solving a nonlinear least squares problem are iterative and each iteration step usually requires the solution of a related linear least squares problem. This means that the problem is linearized at each step to produce an approximate solution.

The aim of a nonlinear least squares problem is to find a global minimizer of the sum of squares of  $m$  nonlinear functions,

$$\min_{\mathbf{x} \in \mathbb{R}^n} F(\mathbf{x}), \quad F(\mathbf{x}) = \frac{1}{2} \sum_{i=1}^m r_i^2(\mathbf{x}), \quad (1.3)$$

where  $r_i(\mathbf{x})$  are the components of the residual  $\mathbf{r}(\mathbf{x})$  introduced before.

We will present two methods for solving this kind of problems.

#### The Newton method

Let us consider the problem of finding the zeros of a function of  $n$  variables, that is we want to solve equations of the form

$$G(\mathbf{x}) = 0,$$

where  $G : D \rightarrow \mathbb{R}^n$  is a continuously differentiable function defined on some open subset  $D \subset \mathbb{R}^n$ .

Let  $\mathbf{x}_0$  be an approximation to a zero of the function  $G$ . In a neighborhood of  $\mathbf{x}_0$ , by Taylor's formula, we have that

$$G(\mathbf{x}) \approx G(\mathbf{x}_0) + G'(\mathbf{x}_0)(\mathbf{x} - \mathbf{x}_0) + \dots,$$

where

$$G'(\mathbf{x}) = \left( \frac{\partial G_j}{\partial \mathbf{x}_k}(\mathbf{x}) \right)_{j,k=1,\dots,n}$$

denotes the Jacobian matrix of  $G$ . We obtain a new approximation  $\mathbf{x}_1$  for the solution of  $G(\mathbf{x}) = 0$  by solving the linearized equation

$$G(\mathbf{x}_0) + G'(\mathbf{x}_0)(\mathbf{x} - \mathbf{x}_0) = 0,$$

which is

$$\mathbf{x}_1 = \mathbf{x}_0 - [G'(\mathbf{x}_0)]^{-1}G(\mathbf{x}_0).$$

Iterating this procedure leads to *Newton's method*, as described in the following definition.

**Definition 1.1.1** Let  $D \subset \mathbb{R}^n$  be open and let  $G : D \rightarrow \mathbb{R}^n$  be a continuously differentiable function such that the Jacobian matrix  $G'(\mathbf{x})$  is nonsingular for all  $\mathbf{x} \in D$ . Then Newton's method for the solution of the equation

$$G(\mathbf{x}) = 0$$

is given by the iteration scheme

$$\mathbf{x}_{k+1} := \mathbf{x}_k - [G'(\mathbf{x}_k)]^{-1}G(\mathbf{x}_k), \quad k = 0, 1, \dots,$$

starting with some  $\mathbf{x}_0 \in D$ .

We explicitly note that  $\mathbf{x}_{k+1}$  is obtained by solving the system of linear equations

$$G'(\mathbf{x}_k)(\mathbf{x}_k - \mathbf{x}_{k+1}) = G(\mathbf{x}_k).$$

Of course, we cannot expect that Newton's method will always converge. However, we can assure local convergence; see [40].

Although Newton's method is very attractive, it has to be observed that one step of the Newton iteration for nonlinear systems can be very costly both because the need for evaluating the entries of the Jacobian  $G'(\mathbf{x}_k)$  and the cost of solving the linear system to arrive at the iteration  $\mathbf{x}_{k+1}$ .

Let us come back to problem (1.3). Minimizing the function  $F$  requires the solution of  $\nabla F(\mathbf{x}) = 0$ . To achieve this goal, we set  $G(\mathbf{x}) = \nabla F(\mathbf{x})$  and then, we apply the Newton method to the function  $G$ . This procedure involves the computation (or the approximation) of both the gradient vector  $G(\mathbf{x}_k)$  and the Hessian matrix  $G'(\mathbf{x}_k)$  of the function to be minimized, leading to an algorithm characterized by a large computational complexity. To overcome this difficulty, we resort to the Gauss–Newton method which is described in the following subsection.

### The Gauss–Newton method

The *Gauss–Newton* method for problem (1.3) is based on a sequence of linear approximations of  $\mathbf{r}(\mathbf{x})$ . The method minimizes, at the  $k$ th iteration step, the norm of a linear approximation of the residual  $\mathbf{r}(\mathbf{x}_k + \mathbf{s}_k)$  with respect to the step size  $\mathbf{s}_k$ . So we can write

$$\mathbf{r}(\mathbf{x}_{k+1}) \simeq \mathbf{r}(\mathbf{x}_k) + J(\mathbf{x}_k)\mathbf{s}_k.$$

If  $\mathbf{x}_k$  denotes the current approximation, then the step  $\mathbf{s}_k$  is computed as a solution of the linear least squares problem

$$\min_{\mathbf{s}} \|\mathbf{r}(\mathbf{x}_k) + J(\mathbf{x}_k)\mathbf{s}\|, \quad \mathbf{s} \in \mathbb{R}^n, \quad (1.4)$$

where  $J(\mathbf{x}_k)$  is the Jacobian matrix of  $\mathbf{r}(\mathbf{x})$ . The new approximation is  $\mathbf{x}_{k+1} = \mathbf{x}_k + \mathbf{s}_k$ .

The Gauss–Newton method as described above has the advantage that it solves linear problems in just one iteration and has fast local convergence on mildly nonlinear and nearly consistent problems. However, it may not even be locally convergent on problems that are strongly nonlinear or have large residuals. In these cases we apply the *damped Gauss–Newton method*, that is

$$\mathbf{x}_{k+1} = \mathbf{x}_k + \alpha_k \mathbf{s}_k,$$

where  $\mathbf{s}_k$  is the solution of (1.4) and  $\alpha_k$  is a parameter to be determined. When  $J(\mathbf{x}_k)$  is rank deficient  $\mathbf{s}_k$  can be chosen as the minimum norm solution of the linear least squares problem (1.4). Properties about this method are presented in [2] and a discussion on the local convergence of Gauss–Newton method can be found in [59].

Two strategies for choosing  $\alpha_k$  are:

- *Armijo–Goldstein principle* [49]. Since

$$\mathbf{r}(\mathbf{x}_k + \alpha_k \mathbf{s}_k) \simeq \mathbf{r}(\mathbf{x}_k) + \alpha_k J(\mathbf{x}_k) \mathbf{s}_k,$$

or equivalently

$$\mathbf{r}(\mathbf{x}_k) - \mathbf{r}(\mathbf{x}_k + \alpha_k \mathbf{s}_k) \simeq -\alpha_k J(\mathbf{x}_k) \mathbf{s}_k,$$

we want to decrease the objective function which verifies

$$\|r(\mathbf{x}_k) - r(\mathbf{x}_k + \alpha_k \mathbf{s}_k)\|^2 \geq \|r(\mathbf{x}_k)\|^2 - \|r(\mathbf{x}_k + \alpha_k \mathbf{s}_k)\|^2.$$

In order to do it this method takes  $\alpha_k$  as the largest number in the sequence  $2^{-i}$ ,  $i = 0, 1, \dots$  for which the inequality

$$\|r(\mathbf{x}_k)\|^2 - \|r(\mathbf{x}_k + \alpha_k \mathbf{s}_k)\|^2 \geq \frac{1}{2} \alpha_k \|J(\mathbf{x}_k) \mathbf{s}_k\|^2$$

is satisfied. This choice ensures the convergence of the method provided that  $\mathbf{x}_k$  is not a critical point, while the unrelaxed iteration may not converge at all.

- Taking  $\alpha_k$  as the solution to the one–dimensional minimization problem

$$\min_{\alpha} \|r(\mathbf{x}_k + \alpha \mathbf{s}_k)\|^2.$$

## 1.2 SVD and Generalized SVD

One of the most relevant tools for the analysis of discrete ill-posed problems are the *Singular Value Decomposition* (SVD) of the coefficient matrix  $A$  of the problem and its generalization to two matrices, the *Generalized Singular Value Decomposition* (GSVD) of the matrix pair  $(A, L)$ , where  $L$  is a *regularization matrix*.

The SVD reveals all the difficulties associated with the ill-conditioning of the matrix  $A$  while the GSVD of  $(A, L)$  yields important insight into the regularization problem involving both the coefficient matrix  $A$  and the regularization matrix  $L$ .

In the next subsections we will present both methods.

### 1.2.1 The Singular Value Decomposition

The Singular Value Decomposition (SVD) has many useful applications in numerous areas such as signal and image processing, statistics, pattern recognition, etc.

The SVD of a rectangular matrix is a matrix decomposition for the treatment of least squares problems since the unitary matrices that transform  $A$  to diagonal form do not change the  $l_2$ -norm of vectors.

**Theorem 1.2.1 Singular Value Decomposition.** *Let  $A \in \mathbb{R}^{m \times n}$  be a rectangular matrix with  $m \geq n$ . Then the matrix  $A$  can be broken down into the product of three matrices*

$$A = U\Sigma V^T = \sum_{i=1}^n \mathbf{u}_i a_i \mathbf{v}_i^T, \quad (1.5)$$

where  $U = (\mathbf{u}_1, \dots, \mathbf{u}_m) \in \mathbb{R}^{m \times m}$  and  $V = (\mathbf{v}_1, \dots, \mathbf{v}_n) \in \mathbb{R}^{n \times n}$  are orthogonal matrices, and where  $\Sigma \in \mathbb{R}^{m \times n}$  is a diagonal matrix whose elements are nonnegative and appear in non-increasing order

$$a_1 \geq \dots \geq a_r > 0, \quad r \leq n.$$

The quantities  $a_i$  are called the *singular values* of  $A$ , and its rank  $r$  is equal to the number of positive singular values. The vectors  $\mathbf{u}_i$  and  $\mathbf{v}_i$  are the *left and right singular vectors* of  $A$ , respectively, and the *condition number* of  $A$  is equal to the ratio  $a_1/a_r$ .

Every matrix  $A \in \mathbb{R}^{m \times n}$  has a unique Singular Value Decomposition, except for singular vectors associated with multiple singular values or null singular values, since the SVD is strongly linked to the eigenvalue

decomposition of the symmetric positive semi-definite matrices  $A^T A$  and  $AA^T$ .

Two characteristic features of the SVD of a matrix are very often found in practical applications concerning discrete ill-posed problems.

- The singular values decay gradually to zero. As the dimension of  $A$  increases, then a growth in the number of small singular values can be appreciated.
- The vectors  $\mathbf{u}_i$  and  $\mathbf{v}_i$  tend to have more sign changes in their elements as the index  $i$  increases (like high frequencies Fourier vectors).

The content of this section can be extended to the case in which the matrices has complex elements [2].

### 1.2.2 The Generalized Singular Value Decomposition

We introduce the generalization of the Singular Value Decomposition (GSVD) for two matrices  $A \in \mathbb{R}^{m \times n}$  and  $L \in \mathbb{R}^{p \times n}$ , with the same number of columns, under the assumption  $\mathcal{N}(A) \cap \mathcal{N}(L) = \{0\}$ , where  $\mathcal{N}(A)$ ,  $\mathcal{N}(L)$  represent the kernels of the matrices  $A$  and  $L$ , respectively. The GSVD and its application to certain constrained least squares problems were first studied by Van Loan [72]. Paige and Saunders [51] extended the GSVD to handle all possible cases, and gave a computationally more amenable form.

The generalized singular values of  $(A, L)$  are the square roots of the generalized eigenvalues of the matrix pair  $(A^T A, L^T L)$ .

**Theorem 1.2.2 Generalized Singular Value Decomposition.** *We assume that the dimensions of  $A \in \mathbb{R}^{m \times n}$  and  $L \in \mathbb{R}^{p \times n}$  satisfy  $m \geq n \geq p$ . Then the GSVD is the decomposition of  $A$  and  $L$  in the form*

$$A = U \begin{pmatrix} \Sigma_A & 0 \\ 0 & I_{n-p} \end{pmatrix} Z^{-1}, \quad L = V \begin{pmatrix} \Sigma_L & 0 \end{pmatrix} Z^{-1}, \quad (1.6)$$

where the columns of  $U \in \mathbb{R}^{m \times n}$  and  $V \in \mathbb{R}^{p \times p}$  are orthonormal,  $Z \in \mathbb{R}^{n \times n}$  is non singular, and  $\Sigma_A$  and  $\Sigma_L$  are  $p \times p$  diagonal matrices:

$$\Sigma_A = \text{diag}(a_1, \dots, a_p), \quad \Sigma_L = \text{diag}(l_1, \dots, l_p).$$

Further, we have

$$0 \leq a_1 \leq \dots \leq a_p \leq 1, \quad 1 \geq l_1 \geq \dots \geq l_p \geq 0,$$

normalized such that  $a_i^2 + l_i^2 = 1$  for  $i = 1, \dots, p$ .

A complete treatment of the GSVD is given in [2].

### 1.3 Regularization Methods

In general terms, *regularization* is the approximation of an ill-posed problem by a family of neighboring well-posed problems. Firstly, let us focus on the linear case.

We want to find a suitable approximation of the generalized solution  $\mathbf{x}^\dagger = A^\dagger \mathbf{b}$  of

$$A\mathbf{x} = \mathbf{b}$$

for a specific right-hand side  $\mathbf{b}$  in the case when we do not know the “exact data”  $\mathbf{b}$  but we have an its approximation such that

$$\|\mathbf{b}^\zeta - \mathbf{b}\| \leq \zeta$$

is available. We will call  $\mathbf{b}^\zeta$  the “noisy data” and  $\zeta$  the “noise level”.

In the ill-posed case,  $A^\dagger \mathbf{b}^\zeta$  is certainly not a good approximation of  $A^\dagger \mathbf{b}$  due to the unboundedness of  $A^\dagger$  even if it exists. We are looking for some approximation  $\mathbf{x}_\delta^\zeta$  of  $\mathbf{x}^\dagger$  which, on the one hand, depends continuously on the (noisy) data  $\mathbf{b}^\zeta$ , so that it can be computed in a stable way, and has, on the other hand, the property that as the noise level  $\zeta$  decreases to zero and the *regularization parameter*  $\delta$  is chosen appropriately, then  $\mathbf{x}_\delta^\zeta$  tends to  $\mathbf{x}^\dagger$ .

Taking some considerations mentioned in [17] into account we can give the following definition.

**Definition 1.3.1** Let  $A : \mathcal{X} \rightarrow \mathcal{Y}$  be a bounded linear operator between the Hilbert spaces  $\mathcal{X}$  and  $\mathcal{Y}$ ,  $\delta_0 \in (0, +\infty]$ . For every  $\delta \in (0, \delta_0)$ , let

$$R_\delta : \mathcal{Y} \rightarrow \mathcal{X}$$

be a continuous (not necessarily linear) operator. The family  $\{R_\delta\}$  is called a *regularization* or a *regularization operator* (for  $A^\dagger$ ), if, for all  $\mathbf{b} \in D(A^\dagger)$ , there exists a parameter choice rule  $\delta = \delta(\delta, \mathbf{b}^\zeta)$  such that

$$\limsup_{\zeta \rightarrow 0} \{\|R_{\delta(\zeta, \mathbf{b}^\zeta)} \mathbf{b}^\zeta - A^\dagger \mathbf{b}\| \mid \mathbf{b}^\zeta \in \mathcal{Y}, \|\mathbf{b}^\zeta - \mathbf{b}\| \leq \zeta\} = 0 \quad (1.7)$$

holds true. Here,

$$\delta : \mathbb{R}^+ \times \mathcal{Y} \rightarrow (0, \delta_0)$$

is such that

$$\limsup_{\zeta \rightarrow 0} \{\delta(\zeta, \mathbf{b}^\zeta) \mid \mathbf{b}^\zeta \in \mathcal{Y}, \|\mathbf{b}^\zeta - \mathbf{b}\| \leq \zeta\} = 0. \quad (1.8)$$

For a specific  $\mathbf{b} \in D(A^\dagger)$ , a pair  $(R_\delta, \delta)$  is called a (convergent) *regularization method* (for solving  $A\mathbf{x} = \mathbf{b}$ ) if (1.7) and (1.8) hold true.

A regularization method consists of a regularization operator and a parameter choice rule which is convergent in the sense that, if the regularization parameter is chosen according to (1.7), then the regularized solutions  $R_{\delta(\xi, \mathbf{b}^\xi)} \mathbf{b}^\xi$  converge to  $A^\dagger \mathbf{b}$  as the noise level  $\xi$  tends to zero.

It is not required the regularization operator  $\{R_\delta\}$  to be a family of linear operators. If the  $R_\delta$  are linear, then we call the corresponding method a *linear regularization method*, and the family  $\{R_\delta\}$  a *linear regularization operator*. However, it also makes sense to consider nonlinear regularization methods for solving linear problems.

Similarly to the linear case, if we consider the operator equation

$$F(\mathbf{x}) = \mathbf{b},$$

where  $F : D(F) \subset \mathcal{X} \rightarrow \mathcal{Y}$  is a nonlinear operator between Hilbert spaces  $\mathcal{X}$  and  $\mathcal{Y}$ , we are interested in the situation that a solution  $\mathbf{x}^\dagger$  does not depend continuously on the data. Since in practice only approximate data  $\mathbf{b}^\xi$  with

$$\|\mathbf{b}^\xi - \mathbf{b}\| \leq \xi$$

are available, the problem has to be regularized. For more complete information see [69].

In the following subsections we briefly describe the most commonly regularization methods when ill-posed inverse problems are treated.

### 1.3.1 The Tikhonov Regularization

In the numerical solution of the equation  $A\mathbf{x} = \mathbf{b}$ , problems occur when the singular values of the operator  $A$  tend to zero rapidly, causing the norm of the approximate solution  $\mathbf{x}_k$  to go to infinity when  $k \rightarrow \infty$ . The idea in the basic regularization scheme discussed in this section is to control simultaneously the norm of the residual  $\mathbf{r} = A\mathbf{x} - \mathbf{b}$  and a regularization term, replacing the minimization problem (1.2) by a penalized least-squares problem.

A typical approach for the solution of ill-posed problems is the *Tikhonov regularization*. It has been applied by various authors to the inversion of geophysical data; see, for example, [4, 11, 33]

**Definition 1.3.2** Let  $\delta > 0$  be a given constant. The Tikhonov regularized solution  $\mathbf{x}_\delta \in \mathbb{R}^n$  is the minimizer of the following least squares problem

$$\|A\mathbf{x} - \mathbf{b}\|^2 + \delta \|L\mathbf{x}\|^2,$$

provided that a minimizer exists. The parameter  $\delta > 0$  is called the regularization parameter and the matrix  $L$  is the regularization matrix.

The matrix  $L$  is chosen so that the null spaces of  $A$  and  $L$  intersect trivially. Common regularization matrices are either the identity matrix  $I$  or finite difference matrices, such as

$$L = \begin{bmatrix} 1 & -1 & & & 0 \\ & 1 & -1 & & \\ & & \ddots & \ddots & \\ 0 & & & 1 & -1 \end{bmatrix} \in \mathbb{R}^{(n-1) \times n}$$

or

$$L = \begin{bmatrix} -1 & 2 & -1 & & 0 \\ & -1 & 2 & -1 & \\ & & \ddots & \ddots & \\ 0 & & & -1 & 2 & -1 \end{bmatrix} \in \mathbb{R}^{(n-2) \times n}.$$

The null spaces of these matrices are

$$N(L_1) = \text{span}\{[1, 1, \dots, 1]^T\}$$

and

$$N(L_2) = \text{span}\{[1, 1, \dots, 1]^T, [1, 2, \dots, n]^T\}.$$

These matrices therefore are referred to as *smoothing regularization matrices*. The use of a smoothing regularization matrix can be beneficial when the desired solution is a discretization of a smooth function.

The Tikhonov regularized solution exists, is unique, and is given by the formula

$$\mathbf{x}_\delta = (A^T A + \delta^2 L^T L)^{-1} A^T \mathbf{b}.$$

### 1.3.2 TSVD and TGSVD

A different way to treat the ill-conditioning of  $A$  is to derive a new problem with a well-conditioned *rank-deficient* coefficient matrix. The closest *rank- $\ell$*  approximation,  $A_\ell$ , is obtained by truncating the SVD expansion in (1.5) at  $\ell$ . Then,  $A_\ell$  is given by

$$A_\ell = \sum_{i=1}^{\ell} \mathbf{u}_i a_i \mathbf{v}_i^T, \quad \ell \leq n. \quad (1.9)$$

The truncated SVD regularization solves the problem

$$\min \|\mathbf{x}\| \quad \text{subject to} \quad \min \|A_\ell \mathbf{x} - \mathbf{b}\|$$

and solution of this problem [27] is

$$\mathbf{x}_\ell = \sum_{i=1}^{\ell} \frac{\mathbf{u}_i^T \mathbf{b}}{a_i} \mathbf{v}_i,$$

where  $\ell$  is the truncation parameter.

As an alternative, we can generalize the TSVD method to the TGSVD in order to introduce a regularization matrix  $L$ . The generalized singular value decomposition (1.6) of the matrix pair  $(A, L)$  is

$$A = U \Sigma_A Z^{-1}, \quad L = V \Sigma_L Z^{-1},$$

and the TGSVD solution is

$$\mathbf{x}_{\ell,L} = \sum_{i=p-\ell+1}^p \frac{\mathbf{u}_i^T \mathbf{b}}{a_i} \mathbf{z}_i + \sum_{i=p+1}^n (\mathbf{u}_i^T \mathbf{b}) \mathbf{z}_i.$$

### 1.3.3 Total Variation regularization

For a  $N$ -dimensional function  $u$ , i.e.  $u : [a, b]^N \rightarrow \mathbb{R}$  with  $\Omega = [a, b]^N$ , we define the Total Variation of  $u$  [74] as

$$TV(u) = \sup \left\{ \int_{\Omega} u \operatorname{div} \vec{v} \, dx : \vec{v} \in C_0^1(\Omega, \mathbb{R}^N), |\vec{v}(x)|_2 \leq 1 \text{ for } \forall x \in \Omega \right\},$$

where  $\vec{v} = (v_1, \dots, v_N)^T$ ,  $\operatorname{div} \vec{v} = \sum_{i=1}^N \frac{\partial v_i}{\partial x_i}$ , and  $C_0^1(\Omega, \mathbb{R}^N)$  is the space of continuously differentiable functions with compact support in  $\Omega$ .

If  $u$  is differentiable, then  $TV(u) = \int_{\Omega} |\nabla u|_2 \, dx$ . In discrete case,  $TV(u) = \sum_i |[\nabla u]_i|_2$ .

So, Total Variation regularization consists of solving

$$\min_u \|A\mathbf{u} - \mathbf{b}\|^2 + \gamma \sum_i |[\nabla u]_i|_2.$$

### 1.3.4 Choosing the regularization parameter

The choice of the regularization parameter is crucial in order to obtain a good approximation of the solution. In our case, this decision is taken to determine the truncation index in the TSVD and the regularization parameter in the Tikhonov regularization.

Again, to get a meaningful solution it is essential to correctly estimate the value of the regularization parameter. Several criteria are available for this task, some requiring the knowledge of the standard deviation of the noise affecting the data and some not requiring it.

The regularization parameter can be determined in a variety of ways [17, 27, 28]. We will concentrate on the Discrepancy Principle, the Generalized Cross Validation, and the L-curve; see [60].

### Discrepancy principle

When an accurate estimate of the norm of the error  $\mathbf{e} = \mathbf{b}^{\xi} - \mathbf{b}$  is known, an appropriate value of the parameter often can be determined with the aid of the *discrepancy principle* due to Morozov [48], which chooses it as the smallest index such that

$$\|A\mathbf{x}_\ell - \mathbf{b}\| \leq \tau\|\mathbf{e}\|,$$

where  $\tau > 1$  is a user-supplied constant independent of  $\|\mathbf{e}\|$ . Properties of the discrepancy principle are discussed in [17].

### Generalized Cross Validation and Mallows' criterion

The *Generalized Cross Validation* (GCV) [9, 22, 75, 76] is a statistical method which estimates the optimal value of the regularization parameter  $\lambda$ , under the assumption that the data vector  $\mathbf{b}$  is affected by normally distributed noise, by minimizing the functional

$$G(\lambda) = \frac{\frac{1}{m} \|(I - A(\lambda))\mathbf{b}\|_2^2}{\left[ \frac{1}{m} \text{trace}(I_m - A(\lambda)) \right]^2},$$

where  $m$  is the size of  $\mathbf{b}$  and the influence matrix  $A(\lambda)$  is defined by the identity

$$A\mathbf{x}_\lambda = A(\lambda)\mathbf{b}.$$

In Fig. 1.1 we represent the GCV function and its minimum for the Tikhonov regularization and for the TSVD corresponding to a  $128 \times 128$  matrix generated by the function `deriv2` from Hansen's Regtools package in Matlab.

We can see from the figure that the value of the regularization parameter for Tikhonov is  $\lambda = 5.19 \cdot 10^{-6}$  while the truncation parameter for the TSVD is  $\lambda = 93$  which correspond with the minimum of both of the functions.

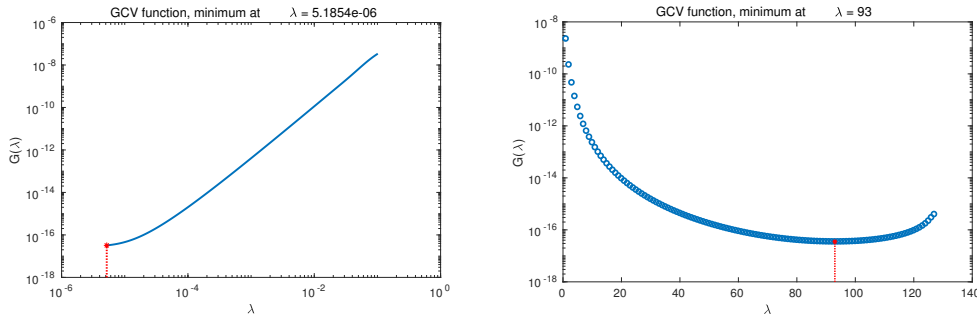


**Figure 1.1:** Representation of the GCV function and its minimum for the Tikhonov regularization on the left-hand side and for the TSVD on the right-hand side.

The GCV has some computationally relevant properties and, moreover, is a *predictive mean-square error criterion* [76], in the sense that it estimates the minimizer of the residual function

$$T(\lambda) = \frac{1}{m} \|A(\mathbf{x}_\lambda - \mathbf{x})\|^2.$$

If the standard deviation  $\hat{\sigma}$  of the noise on the data is known, the following unbiased estimate for the function  $T(\lambda)$  is also available

$$\hat{T}(\lambda) = \frac{1}{m} \|(I - A(\lambda))\mathbf{b}\|^2 - \frac{\hat{\sigma}^2}{m} \text{trace}(I_m - A(\lambda)) + \frac{\sigma^2}{m} \text{trace}(A^2(\lambda)).$$

*Mallows' criterion* chooses the value of  $\lambda$  which minimizes  $\hat{T}(\lambda)$ . Another technique which makes use of the value of  $\hat{\sigma}$  is *Morozov discrepancy principle* [47].

However, numerical experiments reported in the literature (see [9, 61]) showed that these two procedures do not give better results than GCV, even when  $\sigma$  is exactly known.

### L-curve method

The L-curve method, introduced by Hansen [28], consists of the analysis of the piecewise linear curve

$$(\log \|A\mathbf{x}_\lambda - \mathbf{b}\|, \log \|L\mathbf{x}_\lambda\|).$$

In many discrete ill-posed problems this curve exhibits a typical “L” shape and the optimal value of the regularization parameter  $\lambda$  is considered to be the one corresponding to the corner of the “L” (see Fig. 1.2 and Fig. 1.3).

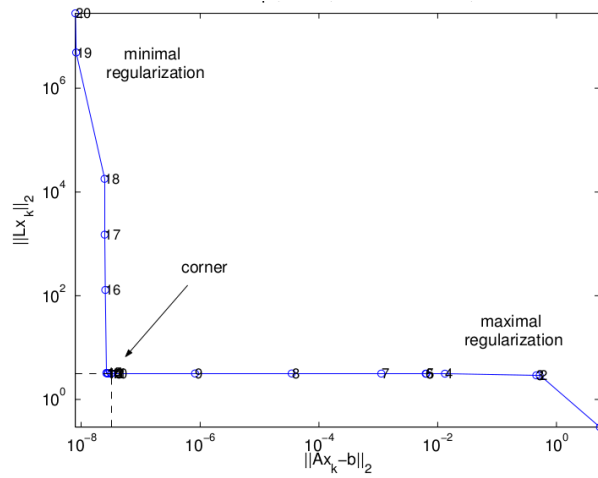


Figure 1.2: Representation of the L-curve and its corner.

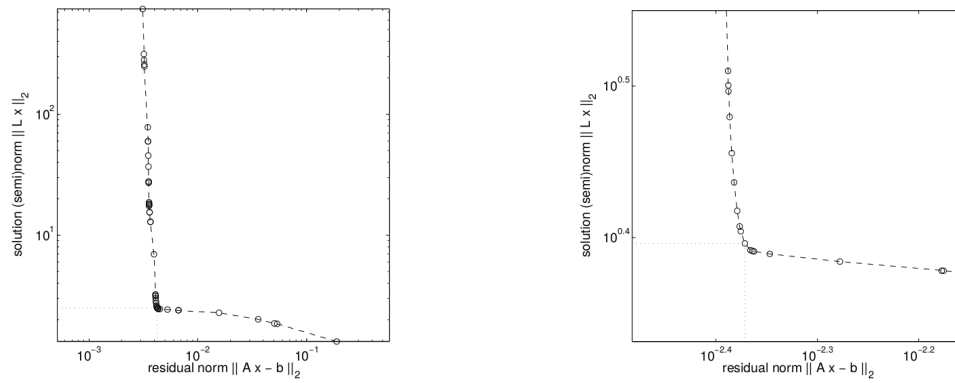


Figure 1.3: L-curve for some real experiments.

This choice is justified by the fact that while the regularized solution  $x_\lambda$  coincides with the least-squares solution  $x$  when  $\lambda = p$  (being  $p$  the number of rows of the regularization matrix  $L$ ), the ill-conditioning of  $A$  causes a strong growth in the weighted semi-norm  $\|Lx_\lambda\|$  when  $\lambda$  exceeds a certain threshold. The corner of the L-curve marks this transition, since it represents a compromise between the minimization of the norm of the residual and the semi-norm of the solution. This choice produces a solution for which both the norm and the residual are fairly small. There are several

papers showing examples in which the L-curve method systematically fails; see [26, 73]. Nevertheless, it has been shown by numerical experiments that it provides a good estimation of the optimal regularization parameter in many inverse problems of applicative interest [30, 60].

A numerical algorithm for the detection of the corner of the L-curve has been introduced in [32]. When the regularization method depends on a continuous parameter  $\lambda$ , like in the Tikhonov regularization, then the L-curve is a smooth function, possibly twice differentiable, and this method selects the value which maximizes the curvature  $\kappa(\lambda)$  of the L-curve. If, on the contrary, the regularization parameter is discrete, like in T(G)SVD or in iterative regularization methods, the algorithm selects the parameter closest to the point of maximum curvature of a cubic spline curve with knots resulting from a local smoothing of the L-curve points. The L-corner method is currently implemented in [29]. More details of this method are also given in [62].

A new approach based on the comparison of regularized solutions computed by both TSVD and the Tikhonov method, has been recently proposed in [34].



# 2

## Linear model for frequency domain electromagnetic (FDEM) data inversion

Assuming a linear dependence between the GCM response and the sub-surface electrical conductivity, McNeill [46] presented a model to estimate conductivities for simple multilayered earth models, which is applicable for low induction numbers

$$B = \frac{r}{\delta} = r \sqrt{\frac{\mu_0 \omega \sigma}{2}} \ll 1,$$

under the assumption of uniform electrical conductivity  $\sigma$  measured in Siemens/meter (S/m). Here  $r$  is the inter-coil distance,  $\delta$  represents the skin depth,  $\mu_0 = 4\pi 10^{-7}$  is the magnetic permeability of free space measured in Henries/meter (H/m) and  $\omega = 2\pi f$  is the angular frequency with  $f$  the operating frequency of the device in Hertz.

Adopting this linear model, that we will study in the next section, a Tikhonov inverse procedure was implemented in [4] with a finite difference approximation of the second derivative as a regularization matrix to reconstruct the electrical conductivity with respect to depth. In [11] a least squares inverse procedure with the Tikhonov regularization, optimized with a projected conjugate gradient algorithm, has been proposed.

In [13], we propose a numerical method based on the approximation of the electrical conductivity of the soil by either a piecewise constant function or a linear spline, and then we apply both the TSVD (see Section 1.3.2) and the Tikhonov regularization (see Section 1.3.1) to the linear inverse problem. In this chapter we describe this technique and we show some numerical results.

Two among the most well known devices for this kind of measurements are the Geonics EM-38 and EM-31; see [4, 46]. Both provide measurements of both the conductivity and magnetic susceptibility components. The EM-31 and EM-38 are used for different applications because of the difference

in inter-coil spacing, which affects the effective depth of exploration. The EM-31 has a coil spacing of 3.7 meters that allows it to reach depths of approximately 6 meters in the vertical dipole mode and approximately 3 meters in the horizontal dipole mode. These depths make the EM-31 great for maps geologic variations, groundwater contaminants, or any subsurface feature associated with changes in ground conductivity using an electromagnetic inductive technique that allows measurements without electrodes or ground contact. With this inductive method, surveys can be carried out under most geologic conditions including those of high surface resistivity such as sand, gravel, and asphalt. They can be also used to perform sounding surveys when several measurements (at different heights/frequencies) are provided at each location to get quantitative estimates of depth variations in true electrical conductivity. The EM-38, on the other hand, has a much smaller inter-coil spacing of either 1 meter or 0.5 meters. This means its depth of exploration ranges from about 1.5 meters to 0.375 meters, depending on coil selection and dipole mode. The shallow nature of the EM-38 makes it suitable for applications in agriculture, archaeology and general soil sciences.

## 2.1 The linear model

The linear model developed by McNeill in 1980 [46] consists of the following system of two Fredholm integral equations of the first kind; see [39, 41],

$$\begin{cases} M^V(h) = \int_0^\infty \phi^V(z+h) \sigma(z) dz, \\ M^H(h) = \int_0^\infty \phi^H(z+h) \sigma(z) dz, \end{cases} \quad (2.1)$$

where  $\sigma(z)$  denotes the conductivity at depth  $z$  (measured in meters),  $h$  is the height at which the measurements are taken,  $M^V(h)$  and  $M^H(h)$  denote the *apparent conductivity* for the vertical and horizontal orientation of the coils, respectively, and the kernels  $\phi^V$  and  $\phi^H$  are the *sensitive functions* for the vertical and horizontal orientation, respectively defined as

$$\phi^V(z) = \frac{4z}{(4z^2 + 1)^{3/2}}, \quad \phi^H(z) = 2 - \frac{4z}{(4z^2 + 1)^{1/2}}.$$

Let us remark than the kernels above introduced are integrable, being

$$\phi^V(z) = \frac{d}{dz} \left( -\frac{1}{\sqrt{4z^2 + 1}} \right), \quad \phi^H(z) = \frac{d}{dz} \left( 2z - \sqrt{4z^2 + 1} \right).$$

This model is appropriate when the conductivity of the soil is relatively low ( $\sigma \simeq 100$  mS/m). However, the model breaks down and errors become significant as the average soil conductivity increases.

Fig. 2.1 shows the behavior of the functions  $\phi^V$  and  $\phi^H$ . It reflects the relative contribution of the electrical conductivity at depth  $z$  to a certain measurement. We see from this figure that, for the vertical orientation ( $\phi^V$ ), material located at a depth  $z = 0.4$  (that is approximately 0.4 times the distance between the coils) gives maximum contribution to the secondary magnetic field but that material at a depth of  $z = 1.5$  (1.5 times the inter-coil distance) still contributes significantly. However, with the coils in the horizontal orientation ( $\phi^H$ ), the instrument is most sensitive to the conductivity of the soil near the surface. If we hold the instrument above the ground at height  $h$ , the sensitivity functions become  $\phi^V(z + h)$  and  $\phi^H(z + h)$ .

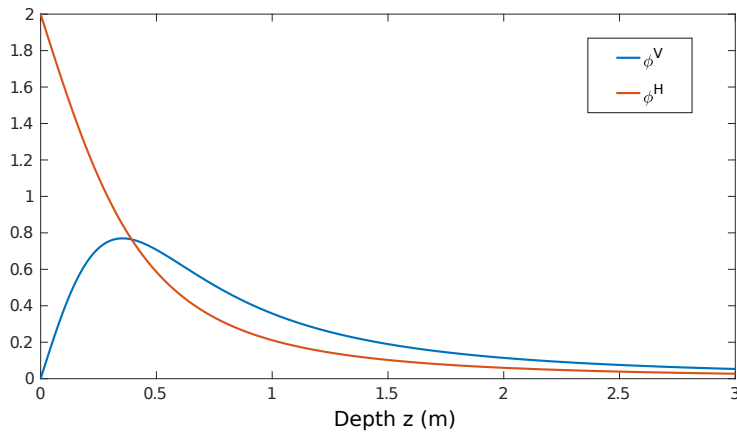


Figure 2.1: The sensitivity functions  $\phi^V$  and  $\phi^H$ .

## 2.2 Numerical methods for the solution of the inverse problem

Let us consider (2.1) and assume that the apparent conductivities  $M^V$  and  $M^H$  are known, and the conductivity  $\sigma$  is unknown. We will reconstruct the electrical conductivity  $\sigma$  of the soil by discretizing Fredholm integral equations (2.1) for turning the given equations into a linear system that can

be solved numerically to provide an approximate discrete solution of the equations.

In order to discretize (2.1) we will propose two different procedures. The first one is based on the approximation of the unknown function  $\sigma$  by using a piecewise constant function, while, in the second one, we approximate the conductivity  $\sigma$  by using a linear spline.

Once these discretizations are introduced, the problem is clearly a linear discrete ill-posed problem and being that, it will be necessary to apply some regularization techniques.

### 2.2.1 Approximation by a piecewise constant function

We represent  $\sigma(z)$  by means of B-splines of order 1 [40, 65] as

$$\sigma(z) \simeq \sum_{j=0}^{\infty} \alpha_j B_j(z), \quad (2.2)$$

with

$$B_j(z) = \begin{cases} 1, & z_j \leq z < z_{j+1}, \\ 0, & \text{otherwise.} \end{cases} \quad (2.3)$$

By replacing (2.2) in (2.1) we get

$$\begin{cases} \sum_{j=0}^{\infty} \alpha_j \int_0^{\infty} \phi^V(z+h) B_j(z) dz = M^V(h), \\ \sum_{j=0}^{\infty} \alpha_j \int_0^{\infty} \phi^H(z+h) B_j(z) dz = M^H(h), \end{cases}$$

from which, by collocating each equation in the  $m$  points  $h_i$  for  $i = 0, \dots, m-1$  corresponding to different heights of the device, we have

$$\begin{cases} \sum_{j=0}^{\infty} \alpha_j \int_0^{\infty} \phi^V(z+h_i) B_j(z) dz = M^V(h_i), \\ \sum_{j=0}^{\infty} \alpha_j \int_0^{\infty} \phi^H(z+h_i) B_j(z) dz = M^H(h_i), \end{cases} \quad i = 0, \dots, m-1.$$

Taking (2.3) into account, we have

$$\begin{aligned}\phi_{ij}^V &:= \int_0^\infty \phi^V(z+h_i)B_j(z)dz = \int_{z_j}^{z_{j+1}} \phi^V(h_i+z) dz \\ &= \frac{1}{\sqrt{4(h_i+z_j)^2+1}} - \frac{1}{\sqrt{4(h_i+z_{j+1})^2+1}}.\end{aligned}\quad (2.4)$$

$$\begin{aligned}\phi_{ij}^H &:= \int_0^\infty \phi^H(z+h_i)B_j(z)dz = \int_{z_j}^{z_{j+1}} \phi^H(h_i+z) dz \\ &= 2(z_{j+1}-z_j) + \sqrt{4(h_i+z_j)^2+1} - \sqrt{4(h_i+z_{j+1})^2+1},\end{aligned}\quad (2.5)$$

and setting  $M^V(h_i) = M_i^V$  and  $M^H(h_i) = M_i^H$ , we can write

$$\begin{cases} \sum_{j=0}^{\infty} \alpha_j \phi_{ij}^V = M_i^V, \\ \sum_{j=0}^{\infty} \alpha_j \phi_{ij}^H = M_i^H. \end{cases}$$

The previous system can be also written as a linear system  $\Phi\alpha = \mathbf{M}$ , with  $m$  rows and infinite columns. To overcome this fact, we need to truncate both the sums above considering them as sums of  $n$  terms. We will see in Section 2.2.3 how to choose the value of  $n$ .

Once we determine  $n$ , we can consider the linear system

$$\Phi\alpha = \mathbf{M}, \quad (2.6)$$

where  $\alpha = [\alpha_j]_{j=0,\dots,n}$  is the array of the unknowns,  $\Phi$  is the matrix of coefficients defined as

$$\Phi = \begin{bmatrix} \phi^V \\ \phi^H \end{bmatrix}, \quad \phi^V = [\phi_{ij}^V]_{\substack{i=1,\dots,m \\ j=0,\dots,n-1}}, \quad \phi^H = [\phi_{ij}^H]_{\substack{i=1,\dots,m \\ j=0,\dots,n-1}},$$

and  $\mathbf{M}$  is the array of the right-hand side

$$\mathbf{M} = \begin{bmatrix} M^V \\ M^H \end{bmatrix}, \quad M^V = [M_0^V, \dots, M_m^V]^T, \quad M^H = [M_0^H, \dots, M_m^H]^T.$$

If we adopt a uniformly spaced discretization both in  $h$  and in  $z$ , with constant step size  $\delta$ , that is

$$h_i = i\delta, \quad z_j = j\delta, \quad \forall i = 0, \dots, m-1, \quad \forall j = 0, \dots, n, \quad (2.7)$$

we get that the entries of our matrices  $\phi_{ij}^V$  and  $\phi_{ij}^H$  defined in (2.4) and (2.5), respectively, become

$$\phi_{ij}^V = \psi_{ij} - \psi_{i,j+1}, \quad \phi_{ij}^H = \frac{1}{\psi_{ij}} - \frac{1}{\psi_{i,j+1}} + 2\delta,$$

where

$$\psi_{ij} = \frac{1}{\sqrt{4(i+j)^2\delta^2 + 1}}.$$

This means that, in this specific case, the blocks of the matrices  $\phi^V$  and  $\phi^H$  are Hankel matrices (or Toeplitz matrices if we invert the rows order).

### 2.2.2 Approximation by a linear spline

Let us now approximate the solution of system (2.1) by using a linear combination of linear B-splines [40, 65],

$$\sigma(z) \simeq \sum_{j=0}^{\infty} \alpha_j B_j(z),$$

where

$$B_j(z) = \begin{cases} \frac{1}{\delta_j}(z - z_{j-1}), & z_{j-1} \leq z < z_j, \\ \frac{1}{\delta_{j+1}}(z_{j+1} - z), & z_j \leq z < z_{j+1}, \\ 0, & \text{otherwise,} \end{cases} \quad \text{if } j \geq 1 \quad (2.8)$$

with  $\delta_j = z_j - z_{j-1}$  and  $j = 0, 1, \dots$  and

$$B_0(z) = \begin{cases} \frac{1}{\delta_1}(z_1 - z), & z_0 \leq z < z_1, \\ 0, & \text{otherwise.} \end{cases}$$

By applying the same procedure as before, we reach the linear system (2.6), where the entries of the blocks of the matrices  $\phi^V$  and  $\phi^H$  are defined as

$$\phi_{ij}^V = \begin{cases} \frac{1}{\sqrt{4(h_i + z_0)^2 + 1}} - \frac{1}{\delta_1}\psi^V(h_i + z_0, h_i + z_1), & \text{if } j = 0 \\ \frac{1}{\delta_j}\psi^V(h_i + z_{j-1}, h_i + z_j) - \frac{1}{\delta_{j+1}}\psi^V(h_i + z_j, h_i + z_{j+1}), & \text{if } j \geq 1, \end{cases} \quad (2.9)$$

where

$$\psi^V(a, b) = \frac{\sinh^{-1}(2b) - \sinh^{-1}(2a)}{2},$$

and

$$\phi_{ij}^H = \begin{cases} \frac{\sqrt{4(z_0 + h_i)^2 + 1}}{2} + \frac{1}{\delta_1} \psi^H(h_i + z_1, h_i + z_0), & \text{if } j = 0 \\ \frac{1}{\delta_j} \psi^H(h_i + z_{j-1}, h_i + z_j) + \frac{1}{\delta_{j+1}} \psi^H(h_i + z_{j+1}, h_i + z_j), & \text{if } j \geq 1, \end{cases} \quad (2.10)$$

with

$$\psi^H(a, b) = \frac{\sinh^{-1}(2b) - \sinh^{-1}(2a)}{4} + \frac{2a(a+b)(b-a)}{\sqrt{4a^2+1} + \sqrt{4b^2+1}} + (b-a)^2.$$

We recall that the linear system to solve is

$$\Phi \alpha = \mathbf{M},$$

where  $\alpha = [\alpha_j]_{j=0, \dots, n}$  is the array of the unknowns,  $\Phi$  is the matrix of coefficients defined as

$$\Phi = \begin{bmatrix} \phi^V \\ \phi^H \end{bmatrix}, \quad \phi^V = [\phi_{ij}^V]_{\substack{i=1, \dots, m \\ j=0, \dots, n}}, \quad \phi^H = [\phi_{ij}^H]_{\substack{i=1, \dots, m \\ j=0, \dots, n}}$$

and  $\mathbf{M}$  is the array of the right-hand side

$$\mathbf{M} = \begin{bmatrix} \mathbf{M}^V \\ \mathbf{M}^H \end{bmatrix}, \quad \mathbf{M}^V = [M_0^V, \dots, M_m^V]^T, \quad \mathbf{M}^H = [M_0^H, \dots, M_m^H]^T.$$

Moreover, taking the discretization (2.7) into account, from (2.9), we can write

$$\phi_{ij}^V = \begin{cases} \frac{1}{\sqrt{4i^2\delta^2 + 1}} - \frac{1}{\delta} \psi^V(i\delta, (i+1)\delta), & \text{if } j = 0 \\ \frac{1}{\delta} \psi^V((i+j-1)\delta, (i+j)\delta) - \frac{1}{\delta} \psi^V((i+j)\delta, (i+j+1)\delta), & \text{if } j \geq 1, \end{cases}$$

and, from (2.10), we obtain

$$\phi_{ij}^H = \begin{cases} \frac{\sqrt{4i^2\delta^2 + 1}}{2} + \frac{1}{\delta} \psi^H((i+1)\delta, i\delta), & \text{if } j = 0 \\ \frac{1}{\delta} \psi^H((i+j-1)\delta, (i+j)\delta) + \frac{1}{\delta} \psi^H((i+j+1)\delta, (i+j)\delta), & \text{if } j \geq 1. \end{cases}$$

This means that, also in this case, the blocks of the matrices  $\phi^V$  and  $\phi^H$  are Hankel matrices (or Toeplitz matrices if we invert the rows order).

### 2.2.3 Truncation error

As we mentioned before, we want to truncate and approximate the sums by finite sums so, to do it, we introduce a truncation parameter  $z_n$ , so that

$$\begin{aligned} \int_0^\infty \phi^V(h_i + z) \sigma(z) dz &= \int_0^{z_n} \phi^V(h_i + z) \sigma(z) dz + \int_{z_n}^\infty \phi^V(h_i + z) \sigma(z) dz \\ &\simeq \sum_{j=0}^{n-1} \phi_{ij}^V \alpha_j + \sum_{j=n}^\infty \phi_{ij}^V \alpha_j, \end{aligned}$$

and aim to determine  $z_n$  so that

$$\left| \sum_{j=n}^\infty \phi_{ij}^V \alpha_j \right| \simeq \left| \int_{z_n}^\infty \phi^V(h_i + z) \sigma(z) dz \right| < \tau.$$

We assume that  $|\sigma(z)| \leq M$ , for  $z \geq 0$ , which implies

$$\left| \int_{z_n}^\infty \phi^V(h_i + z) \sigma(z) dz \right| \leq M \int_{z_n}^\infty \phi^V(h_i + z) dz = \frac{M}{\sqrt{4(h_i + z_n)^2 + 1}}.$$

By requiring that the last quantity is lesser or equal than  $\tau$ , we obtain

$$h_i + z_n > \frac{\sqrt{M^2 - \tau^2}}{2\tau} \simeq \frac{M}{2\tau},$$

from which, for  $h_i \geq 0$  and  $z_n = n\delta$ , it follows

$$n > \frac{M}{2\delta\tau}. \quad (2.11)$$

Under the same assumptions, from

$$\int_{z_n}^\infty \phi^H(h_i + z) dz = \sqrt{4(h_i + z_n)^2 + 1} - 2(h_i + z_n) < \frac{\tau}{M},$$

we obtain

$$n > \frac{M}{4\delta\tau},$$

which is contained in (2.11). This is telling us that the parametrization we should use is also a function of the maximum conductivity in the subsurface. Clearly, at the same time, we would need to take into account that  $M$  must be small enough to make the linear approximation valid.

We remark that the matrix  $\Phi$  of the system (2.6) is a Hankel matrix and is severely ill-conditioned so we need a regularization. For our numerical experiments we will apply both the TSVD (see Section 1.3.2) and the Tikhonov regularization (see Section 1.3.1), and we will choose the regularization parameter by the Discrepancy Principle (see Section 1.3.4), the Generalized Cross Validation criterion (See Section 1.3.4) and the L-curve method (see Section 1.3.4).

## 2.3 Numerical results

In order to verify the inversion procedure, we assume the both orientations of the instrument and we let  $n = 30, 40, 50$  and  $m = 10, 15, 20$ . This means that we simulate a data set with measurements collected at heights  $h_i$ ,  $i = 1, \dots, m$ , starting from the ground level up to 0.1 times the value of  $m$  and that we consider a discretization below the surface with  $n$  layers, to the depth of  $0.1(n - 1)$  meters.

We consider the following model for the electrical conductivity as a function of depth  $z \geq 0$ ,

$$f(z) = e^{-(z-1)^2},$$

which has a maximum at  $z = 1$ ; see Fig. 2.2.

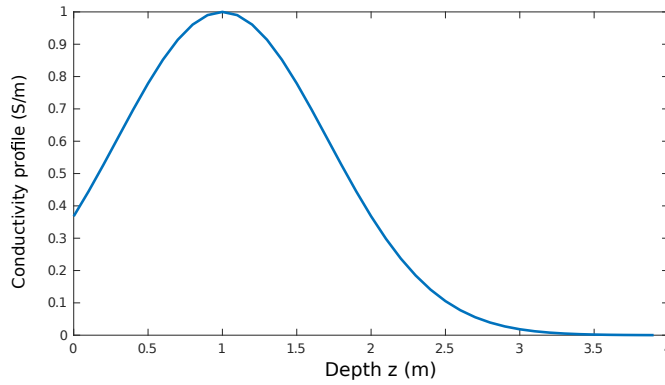


**Figure 2.2:** Test function used to model conductivity with respect to depth in S/m.

A synthetic data set  $\widehat{\mathbf{M}}$  is constructed by applying the linear model (2.1) at the depths  $z_i$ ,  $i = 1, \dots, n$  starting from the ground level down to  $0.1(n - 1)$  meters. Finally, we add white Gaussian noise to the synthetic data by the formula

$$\mathbf{M} = \widehat{\mathbf{M}} + \frac{\xi \|\widehat{\mathbf{M}}\|}{\sqrt{m}} \mathbf{w},$$

where  $\mathbf{w}$  is a vector with normally distributed entries with zero mean and unitary variance, and  $\xi$  is the noise level.

To reconstruct the electrical conductivity  $\sigma$  of the soil we apply the TSVD and the Tikhonov regularization for different choices of the regularization

parameters, as the L-corner method, the Generalized Cross Validation (GCV) and the Discrepancy principle.

n	m	TSVD	Tikhonov
30	10	1.3e-01	1.7e-01
	15	8.9e-02	1.4e-01
	20	5.5e-02	5.9e-02
40	10	1.3e-01	1.0e-01
	15	9.7e-02	1.2e-01
	20	7.9e-02	9.8e-02
50	10	1.8e-01	1.2e-01
	15	1.0e-01	1.1e-01
	20	1.0e-01	1.0e-01

**Table 2.1:** Best errors attainable by the method for selected choices of the regularization parameter applying the TSVD and the Tikhonov regularization, and for an approximation of the solution by a spline of order 1. Profile for  $\sigma$  depicted in Fig. 2.2.

n	m	TSVD	Tikhonov
30	10	1.7e-01	1.3e-01
	15	1.6e-01	1.5e-01
	20	6.6e-02	1.0e-01
40	10	1.3e-01	1.5e-01
	15	1.1e-01	7.9e-02
	20	7.5e-02	8.4e-02
50	10	1.8e-01	1.7e-01
	15	9.6e-02	1.2e-01
	20	1.0e-01	1.1e-01

**Table 2.2:** Best errors attainable by the method for selected choices of the regularization parameter applying the TSVD and the Tikhonov regularization, and for an approximation of the solution by a spline of order 2. Profile for  $\sigma$  depicted in Fig. 2.2.

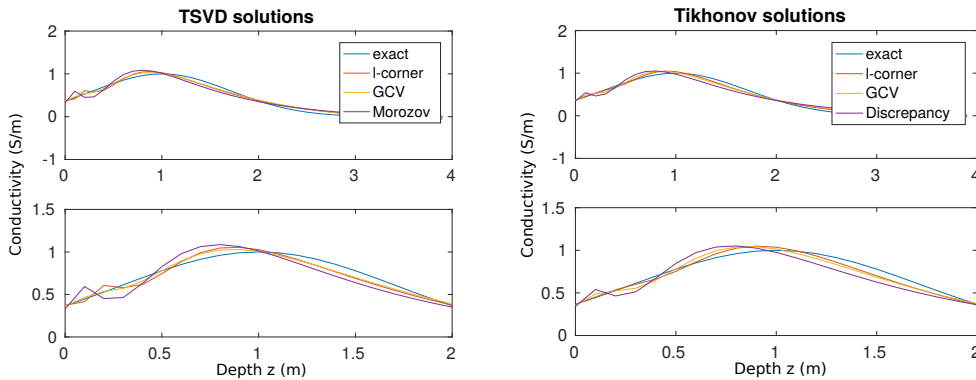
We report in the Table 2.1 and in Table 2.2 the best absolute errors with the infinite norm between the exact solution and its approximation for different numbers of layers,  $n = 30, 40, 50$ , different heights,  $m = 10, 15, 20$  and a noise level  $\zeta = 10^{-4}$ . Table 2.1 shows the results using

an approximation of the electrical conductivity  $\sigma$  by a piecewise constant approximation; see (2.2) and (2.3). In Table 2.2 we can see the results for the same choices of parameters but this time, the conductivity  $\sigma$  is approximated by a linear spline; see (2.2) and (2.8).

We remark that the profile selected for  $\sigma$  takes  $10^3$  mS/m as the maximal value because, as we said at the beginning of this chapter, the linear model is valid only for small values of the conductivity.

We compare the TSVD with the Tikhonov errors reported in Table 2.1 and in Table 2.2, and we can see that both methods are equivalent. Moreover, the tables show that the method is not very sensitive upon the number of layers, the number of heights and the order of the approximation spline for the conductivity  $\sigma$ .

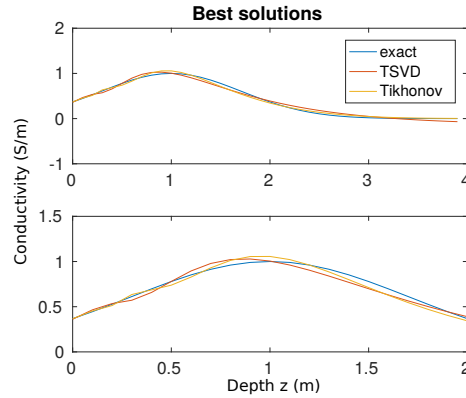
In Fig. 2.3 we depict the graphs of the solutions for the TSVD on the left-hand side and for the Tikhonov regularization on the right-hand side of the figure. This graphs are made approximating the conductivity  $\sigma$  by a spline of order 1 and for  $n = 40$ ,  $m = 20$ ,  $\zeta = 10^{-4}$  choosing the regularization parameter by the L-corner, the GCV and the Discrepancy principle.



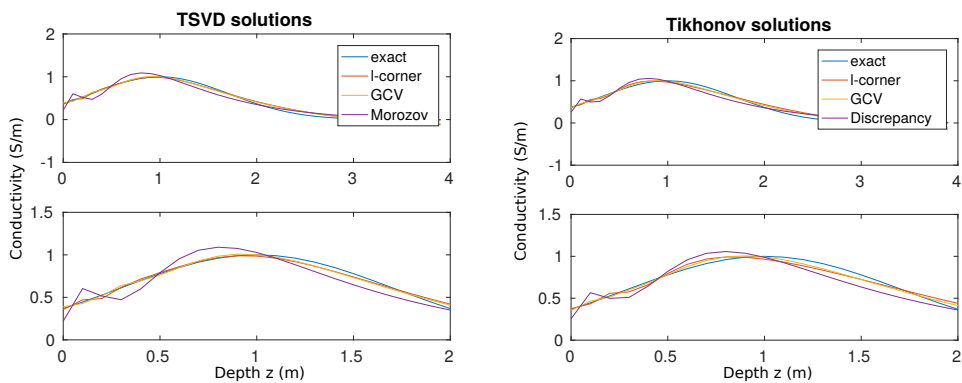
**Figure 2.3:** Representation of the TSVD (left-hand side) and Tikhonov (right-hand side) solutions for different choices of the regularization parameter and for  $n = 40$ ,  $m = 20$ , a noise level  $\zeta = 10^{-4}$  and an approximation of  $\sigma$  by a spline of order 1. The second row is a zoom of the plots of the first row.

Fig. 2.4 shows the best solution (i.e. the one which is “closest” in some sense to the true conductivity profile), applying the TSVD and the best solution applying the Tikhonov regularization taken from Fig. 2.3. The

TSVD takes as the best solution the one that chooses the regularization parameter by the GCV. However, Tikhonov takes as the best solution the one that chooses the parameter by the L-corner.



**Figure 2.4:** Best solutions for the conductivity for  $n = 40$ ,  $m = 20$ , a noise level  $\zeta = 10^{-4}$ , and an approximation of  $\sigma$  by a spline of order 1.



**Figure 2.5:** Representation of the TSVD (left-hand side) and Tikhonov (right-hand side) solutions for different choices of the regularization parameter and for  $n = 40$ ,  $m = 20$ , a noise level  $\zeta = 10^{-4}$  and an approximation of  $\sigma$  by a spline of order 2. The second row is a zoom of the plots of the first row.

In Fig. 2.5 we depict the results for the same values of the parameters but this time we use as approximation of the conductivity  $\sigma$  a spline of

order 2. In this case, the TSVD and the Tikhonov regularization takes as the best solution the one that chooses the regularization parameter by the GCV (see Fig. 2.6).

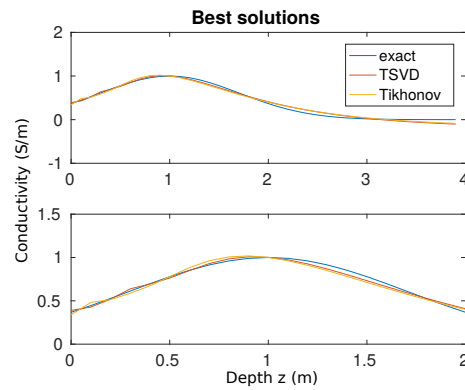


**Figure 2.6:** Best solutions for the conductivity for  $n = 40$ ,  $m = 20$ , a noise level  $\zeta = 10^{-4}$ , and an approximation of  $\sigma$  by a spline of order 2. The second row is a zoom of the plots of the first row.

Now, we want to know what happens if we increase a little the noise level from  $10^{-4}$  to  $10^{-2}$ . In this case, the approximation works worse but still the reconstruction could be acceptable (see Fig. 2.7).

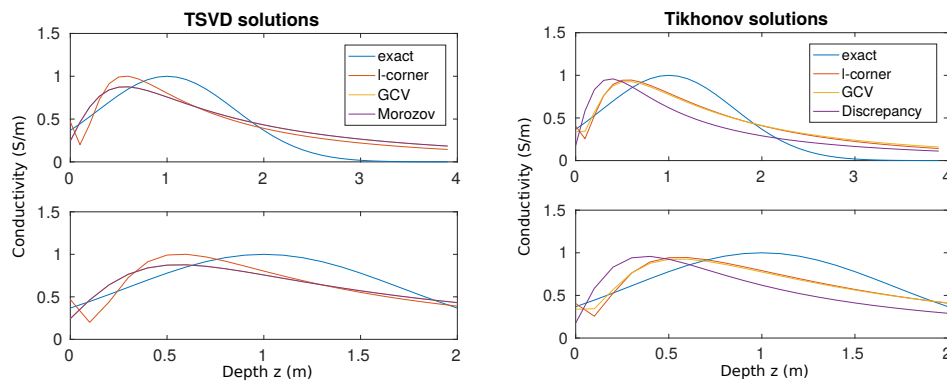


**Figure 2.7:** Representation of the TSVD (left-hand side) and Tikhonov (right-hand side) solutions for different choices of the regularization parameter and for  $n = 40$ ,  $m = 20$ , a noise level  $\zeta = 10^{-2}$  and an approximation of  $\sigma$  by a spline of order 1. The second row is a zoom of the plots of the first row.

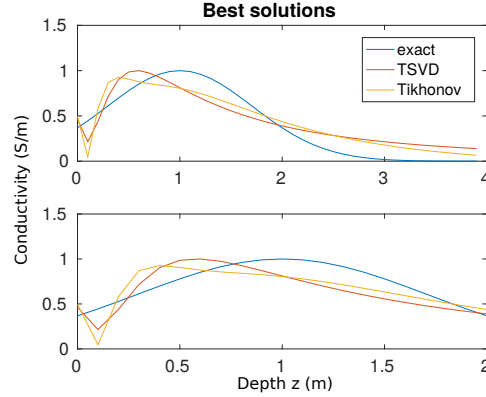


**Figure 2.8:** Best solutions for the conductivity for  $n = 40$ ,  $m = 20$ , a noise level  $\zeta = 10^{-2}$ , and an approximation of  $\sigma$  by a spline of order 1. The second row is a zoom of the plots of the first row.

In Fig. 2.8 are reported the best solutions for the TSVD and the Tikhonov regularization. The best choice of the regularization parameter for both the TSVD and Tikhonov is the L–corner. We decided to depict just the results using the spline of order 1 since the results for the spline of order 2 are similar, making the approximation by the spline of order 1 equivalent to the one by the spline of order 2.

Until now, for our numerical experiments, we took the synthetic data vector  $\widehat{\mathbf{M}}$  as the exact right–hand side of our linear system (2.6). Now, we want compare the data vector obtained from the linear system with the one obtained by a numerical integration. More precisely, we use the *Gauss–Kronrod quadrature* (see [20]).

On the left–hand side of Fig. 2.9, we depict the data vector  $\widehat{\mathbf{M}}$  as the data vector of our linear system (2.6) and its approximation by the Gauss–Kronrod quadrature for the profile  $f(z) = e^{-(z-1)^2}$  of  $\sigma$ , as represented in Fig. 2.2. On the right side we compare this data vector and its approximation for a profile of  $\sigma f(z) = e^{-(z-1)^2} + 1$ .

The left panel in Fig. 2.9 demonstrates that, for small  $\sigma(z)$ , we can simulate the corresponding electrical responses (i.e., the vertical and horizontal apparent conductivities) equally well by using the truncation approximation and the quadrature integration. As it is clear from the right side of Fig. 2.9, this is not true anymore for higher values of  $\sigma$ . At this point, we need to

modify in some way the procedure by using other kinds of approximations for the integrals of the linear model (2.1). This would be the next step of the research on the linear model.

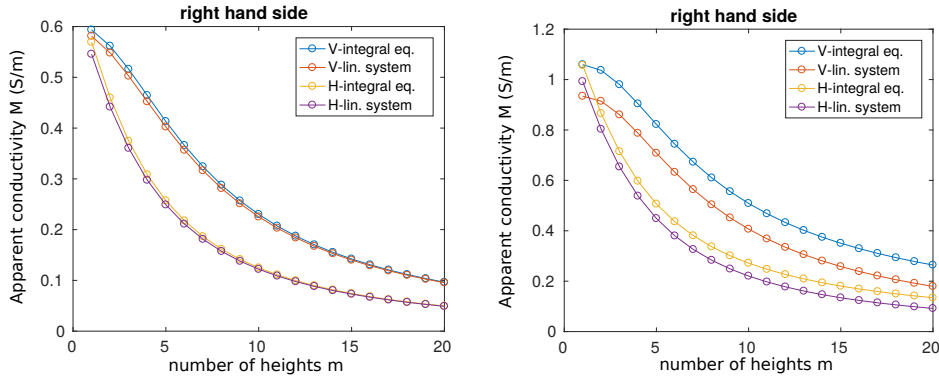


**Figure 2.9:** On the left side, the data vector  $\mathbf{M}$  as from the linear system (2.6) (with  $n = 40$ ;  $m = 20$ ), compared against the corresponding approximation calculated by using the Gauss–Kronrod quadrature for the profile of  $\sigma(z) = e^{-(z-1)^2}$  in Fig. 2.2. On the right side, the same comparison for the profile of  $\sigma(z) = e^{-(z-1)^2} + 1$ .

At the beginning of this chapter, we said that this linear model to reconstruct the conductivity of the soil with respect to depth is valid for small values of  $\sigma$ . To conclude this section, we want to show what happens when  $\sigma$  takes bigger values. In the next chapter we will describe a nonlinear model for reconstructing the conductivity of the soil which is more efficient than the linear one. In the following figures we will compare the synthetic data vector obtained by both the linear model and the nonlinear model.

In Fig. 2.10 we represent a profile of  $\sigma$  which has a maximum at 100 mS/m. Under this profile we depict the synthetic data vector by using both the linear and the nonlinear model for  $n = 80$  and  $m = 20$ . We see, as expected, that they are relatively similar.

However, for the same values of  $n$  and  $m$ , if we choose a profile of  $\sigma$  which has as maximal value  $2 \cdot 10^4$  (Fig. 2.11), we see that the data vectors are very different. This proves the fact for which the linear model does not work well for high values of  $\sigma$ .

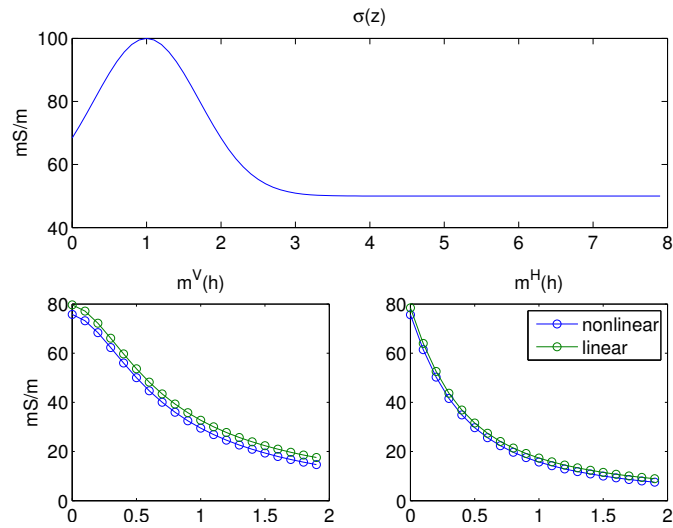


**Figure 2.10:** Profile of  $\sigma$  with maximal value 100 mS/m and the representation of the data obtained by the nonlinear model and the linear model for  $n = 80$ ,  $m = 20$  and the magnetic permeability equal to the one of the free space.

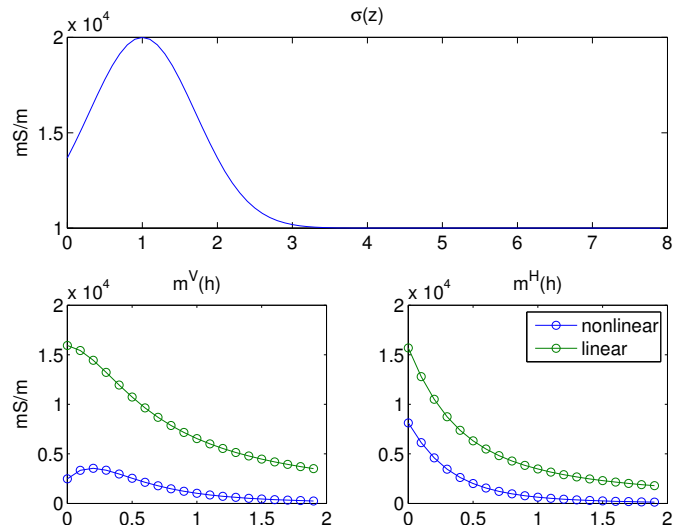


**Figure 2.11:** Profile of  $\sigma$  with maximal value  $2 \cdot 10^4$  mS/m and the synthetic data obtained by the nonlinear and the linear models for  $n = 80$ ,  $m = 20$  and the magnetic permeability the one of the free space.

If we consider the magnetic permeability of the soil to be  $\mu = \sigma\mu_0$ , we obtain the data vectors depicted in Fig. 2.12. To overcome the difficulties of the linear model previously described, we resort to a nonlinear model that we will describe in the next chapter.

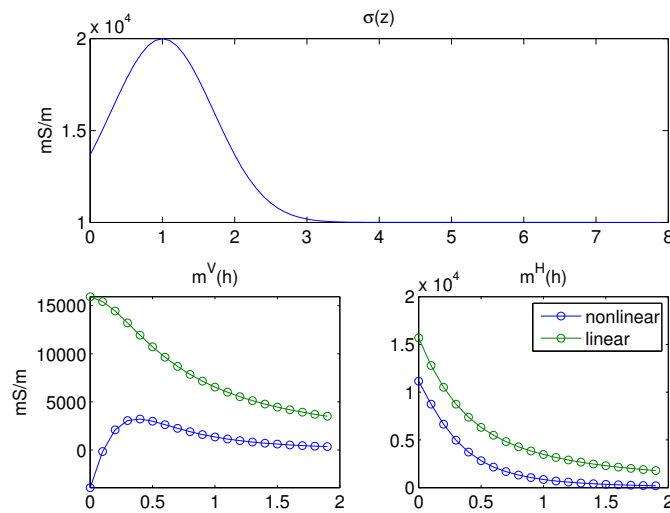


**Figure 2.12:** Profile of  $\sigma$  with maximal value  $2 \cdot 10^4$  mS/m and the representation of the data obtained by the nonlinear model and the linear model for  $n = 80$ ,  $m = 20$  and the magnetic permeability equal to  $\mu = \sigma\mu_0$ .



# 3

## **Nonlinear model for frequency domain electromagnetic (FDEM) data inversion**

In this chapter we try to detect or infer, by non destructive investigation of soil properties, inhomogeneities in the ground or the presence of particular conductive substances such as metals, minerals and other geological structures.

A nonlinear model, presented in [81] for high values of the induction number, is used to describe the interaction of an electromagnetic field with the soil. As we said in Chapter 2, a least squares inverse procedure, implementing a projected conjugate gradient algorithm, is described in [11]. With respect to the data collection strategy previously discussed, recently, new generations of GCMs have been developed. They are designed to record data at multiple coil spacing and orientations using multiple frequencies simultaneously. So there is no need for time-consuming surveys characterized by measurements at different heights for each sounding location.

Accordingly, starting from electromagnetic data collected by a multi-frequency Ground Conductivity Meter (GCM), we try to reconstruct both the electrical conductivity (see [15]) and the magnetic permeability of the soil with respect to depth (see [16]), with a damped Gauss-Newton method with either the Truncated Singular Value Decomposition (TSVD) and the Truncated Generalized Singular Value Decomposition (TGSVD); see Section. 1.3.2, and explicit representation of the Jacobian to solve the nonlinear inverse problem. We propose an inversion method, based on the low-rank approximation of the Jacobian of the nonlinear model, which depends on a relaxation parameter and a regularization parameter chosen by automatic procedures.

We will finish this chapter with some numerical results that show the approximate solution of our nonlinear problem.

### 3.1 The nonlinear model

We briefly recall here the forward model which describes the data measured by an EM device, when the distribution of the conductivity and the magnetic permeability in the subsoil layers are known. It is based on Maxwell's equations, after introducing suitable simplifications to account for the symmetry of the problem. It has been described firstly in [78] and [81], and then has been adapted to the case of a GCM in [33]. The input quantities are the distribution of the electrical conductivity and the magnetic permeability in the subsurface; the output is the instrument reading at height  $h$ .

Following [78], the soil is assumed to possess a layered structure with  $n$  layers, each of thickness  $d_k$ ,  $k = 1, \dots, n$ ; see Fig. 3.1. The thickness of the deeper layer,  $d_n$ , is assumed to be infinite. Let  $\sigma_k$  and  $\mu_k$  be the electrical conductivity and the magnetic permeability in the  $k$ th layer, respectively, which are assumed to be constant inside any layer. The two coils of the measuring device are at height  $h$  above the ground, their distance is  $\rho$ .

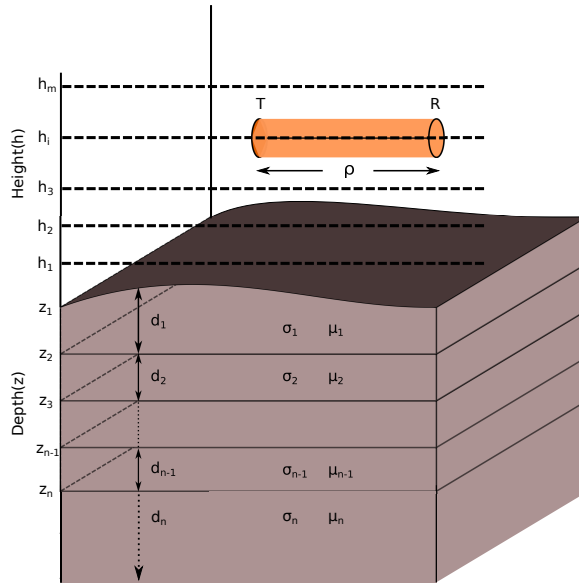


Figure 3.1: Discretization and representation of the subsoil.

Let  $u_k(\lambda) = \sqrt{\lambda^2 + i\sigma_k\mu_k\omega}$ , where  $\omega$  is the angular frequency of the instrument, that is  $2\pi$  times the frequency in Hertz, and the integration variable  $\lambda$  ranges from zero to infinity, and it measures the ratio between the depth below the ground surface and the inter-coil distance  $\rho$ .

If we denote the characteristic admittance of the  $k$ th layer by

$$N_k(\lambda) = \frac{u_k(\lambda)}{i\mu_k\omega}, \quad k = 1, \dots, n,$$

then it is shown in [78] that the surface admittance  $Y_k(\lambda)$  at the top of the same layer verifies the following recursion

$$Y_k(\lambda) = N_k(\lambda) \frac{Y_{k+1}(\lambda) + N_k(\lambda) \tanh(d_k u_k(\lambda))}{N_k(\lambda) + Y_{k+1}(\lambda) \tanh(d_k u_k(\lambda))}, \quad (3.1)$$

for  $k = n - 1, \dots, 1$ . This recursion is initialized by setting  $Y_n(\lambda) = N_n(\lambda)$  at the lowest layer. Notice that both the characteristic and the surface admittances are functions of the frequency  $\omega$  via the functions  $u_k(\lambda)$ .

Assuming that the instrument coils are vertically aligned, the ratio of the secondary to the primary field [12, 33] is given by

$$M_1(\boldsymbol{\sigma}, \boldsymbol{\mu}; h, \omega) = -\rho^3 \int_0^\infty \lambda^2 e^{-2h\lambda} R_{\omega,0}(\lambda) J_0(\rho\lambda) d\lambda, \quad (3.2)$$

where  $\boldsymbol{\sigma} = (\sigma_1, \dots, \sigma_n)^T$ ,  $\boldsymbol{\mu} = (\mu_1, \dots, \mu_n)^T$ ,  $J_s(\lambda)$  denotes the Bessel functions of the first kind of order  $s$ ,

$$R_{\omega,0}(\lambda) = \frac{N_0(\lambda) - Y_1(\lambda)}{N_0(\lambda) + Y_1(\lambda)}, \quad (3.3)$$

$N_0(\lambda) = \lambda / (i\mu_0\omega)$ , where  $\mu_0$  is the magnetic permeability of free space, and  $Y_1(\lambda)$  is computed by the recursion (3.1). We have explicitly highlighted the dependence upon the frequency  $\omega$  in  $R_{\omega,0}(\lambda)$ , since it will be useful in the following.

For the horizontal orientation of the coils, (3.2) is replaced by

$$M_2(\boldsymbol{\sigma}, \boldsymbol{\mu}; h, \omega) = -\rho^2 \int_0^\infty \lambda e^{-2h\lambda} R_{\omega,0}(\lambda) J_1(\rho\lambda) d\lambda. \quad (3.4)$$

We remark that both (3.2) and (3.4) are complex valued functions which can be expressed in terms of the Hankel transform

$$\mathcal{H}_\nu[f](\rho) = \int_0^\infty f(\lambda) J_\nu(\rho\lambda) \lambda d\lambda. \quad (3.5)$$

The available measuring devices, in general, return both the real and the imaginary part of the fields ratio, often referred to as the *in-phase* and the *quadrature* components, respectively.

In many previous works, only the quadrature component of (3.2) and (3.4) have been considered; see [12]. This is justified by the fact that

the imaginary part of  $M_1$  and  $M_2$ , scaled by the constant  $4/(\mu_0\omega r^2)$ , can be interpreted as an electrical conductivity, and is generally referred to as the *apparent conductivity*.

In this thesis we consider both the in-phase and the quadrature component of the fields ratio, since they are both measured by a GCM.

### 3.2 The inverse problem

Some of the more recent EM devices allow for simultaneous measurement by means of a set of different operating frequencies, and the acquisition can be repeated at different heights. So we set  $h = h_1, \dots, h_{m_h}$  and the different frequencies  $\omega = \omega_1, \dots, \omega_{m_\omega}$ , and consider the corresponding  $2m_h m_\omega$  data points  $b_{ij}^v$ , where  $i = 1, \dots, m_h$ ,  $j = 1, \dots, m_\omega$ , and  $v = 1, 2$  represents the two possible orientations of the coils, horizontal and vertical, respectively.

The inverse problem consists of finding the electrical conductivity vector  $\sigma$  and the magnetic permeability vector  $\mu$  which produce the best approximation

$$M_v(\sigma, \mu; h_i, \omega_j) \approx b_{ij}^v, \quad v = 1, 2, \quad i = 1, \dots, m_h, \quad j = 1, \dots, m_\omega.$$

Specifically, we vectorize the data values  $b_{ij}^v$  in lexicographical order into a unique vector  $\mathbf{b} \in \mathbb{C}^m$ ,  $m = 2m_h m_\omega$ . We proceed similarly for the model predictions, obtaining the vector  $\mathbf{M}(\sigma, \mu) \in \mathbb{C}^m$ , and minimize the Euclidean norm of either the in-phase or the quadrature component of the residual between the data and the model, that is

$$(\sigma^*, \mu^*) = \arg \min_{\sigma, \mu \in \mathbb{R}^n} \frac{1}{2} \|\mathbf{r}(\sigma, \mu)\|^2, \quad (3.6)$$

where  $\mathbf{r}(\sigma, \mu) = \text{Re}(\mathbf{b} - \mathbf{M}(\sigma, \mu))$  or  $\mathbf{r}(\sigma, \mu) = \text{Im}(\mathbf{b} - \mathbf{M}(\sigma, \mu))$ . We will denote the components of the residual either by  $r_i(\sigma, \mu)$ ,  $i = 1, \dots, m$  to emphasize their position in the vector  $\mathbf{r}(\sigma, \mu)$ , or by  $r_{ij}^v(\sigma, \mu)$ , when it is important to underline their dependence upon the height  $h_i$  ( $i = 1, \dots, m_h$ ), the frequency  $\omega_j$  ( $j = 1, \dots, m_\omega$ ), and the vertical or horizontal orientation ( $v = 1, 2$ ).

As we said in Section 1.1.2, Newton's method requires the computation of both the gradient vector and the Hessian matrix of the residual, which have a large computational complexity. So, to overcome this difficulty, following [12], we resort to the Gauss-Newton method described in Section 1.1.2, which minimizes, at the  $k$ th iteration step, the norm of a linear approximation of the residual  $\mathbf{r}$  of (3.6).

Let  $\mathbf{r}(\boldsymbol{\sigma}, \boldsymbol{\mu})$  be Fréchet differentiable and let  $(\boldsymbol{\sigma}_k, \boldsymbol{\mu}_k)$  denote the current approximation. Then we can write

$$\mathbf{r}(\boldsymbol{\sigma}_{k+1}, \boldsymbol{\mu}_{k+1}) \simeq \mathbf{r}(\boldsymbol{\sigma}_k, \boldsymbol{\mu}_k) + J(\boldsymbol{\sigma}_k, \boldsymbol{\mu}_k) \mathbf{q}_k,$$

where

$$\mathbf{q}_k = \begin{bmatrix} \mathbf{s}_k \\ \mathbf{t}_k \end{bmatrix}, \quad \mathbf{s}_k \in \mathbb{R}^n, \quad \mathbf{t}_k \in \mathbb{R}^n$$

and  $J(\boldsymbol{\sigma}, \boldsymbol{\mu})$  is the Jacobian of  $\mathbf{r}(\boldsymbol{\sigma}, \boldsymbol{\mu}) = (r_1(\boldsymbol{\sigma}, \boldsymbol{\mu}), \dots, r_m(\boldsymbol{\sigma}, \boldsymbol{\mu}))^T$ , defined by

$$J(\boldsymbol{\sigma}, \boldsymbol{\mu}) = \begin{bmatrix} \frac{\partial \mathbf{r}(\boldsymbol{\sigma}, \boldsymbol{\mu})}{\partial \boldsymbol{\sigma}} & \frac{\partial \mathbf{r}(\boldsymbol{\sigma}, \boldsymbol{\mu})}{\partial \boldsymbol{\mu}} \end{bmatrix},$$

with

$$\left[ \frac{\partial \mathbf{r}(\boldsymbol{\sigma}, \boldsymbol{\mu})}{\partial \boldsymbol{\sigma}} \right] = \frac{\partial r_i(\boldsymbol{\sigma}, \boldsymbol{\mu})}{\partial \sigma_j}, \quad \left[ \frac{\partial \mathbf{r}(\boldsymbol{\sigma}, \boldsymbol{\mu})}{\partial \boldsymbol{\mu}} \right] = \frac{\partial r_i(\boldsymbol{\sigma}, \boldsymbol{\mu})}{\partial \mu_j},$$

for  $i = 1, \dots, m$  and  $j = 1, \dots, n$ . The exact expression of the Jacobian matrix is given in the next Section 3.2.1.

At each iteration  $k$ , the step length  $\mathbf{q}_k$  is the solution of the linear least squares problem

$$\min_{\mathbf{q} \in \mathbb{R}^{2n}} \|\mathbf{r}(\boldsymbol{\sigma}_k, \boldsymbol{\mu}_k) + J_k \mathbf{q}\|, \quad (3.7)$$

with  $J_k = J(\boldsymbol{\sigma}_k, \boldsymbol{\mu}_k)$  or some approximation, leading to the following iterative method namely Gauss–Newton method,

$$\begin{aligned} (\boldsymbol{\sigma}_{k+1}, \boldsymbol{\mu}_{k+1}) &= (\boldsymbol{\sigma}_k + \mathbf{s}_k, \boldsymbol{\mu}_k + \mathbf{t}_k) \\ &= (\boldsymbol{\sigma}_k - J_k^\dagger \mathbf{r}(\boldsymbol{\sigma}_k, \boldsymbol{\mu}_k), \boldsymbol{\mu}_k - J_k^\dagger \mathbf{r}(\boldsymbol{\sigma}_k, \boldsymbol{\mu}_k)). \end{aligned} \quad (3.8)$$

Let us note that by using the generalized inverse of  $J$ , the least squares approach is implicitly applied.

When the residuals  $r_i(\boldsymbol{\sigma}_k, \boldsymbol{\mu}_k)$  are small or mildly nonlinear in a neighborhood of the solution, the Gauss–Newton method is expected to behave similarly to Newton’s method [2]. We remark that, while the physical problem is obviously consistent, this is not necessarily true in our applicative case, where in the presence of noise in the data the problem will generally be inconsistent. In the case of a mildly nonlinear problem, a linear model is available; see Chapter 2 and [4, 46].

To ensure convergence, we resort to the damped Gauss–Newton method which starts with an initial point  $\mathbf{x}_0$ , then computes the step direction  $\mathbf{q}$  and calculates the new iterate replacing the approximation (3.8) by

$$(\boldsymbol{\sigma}_{k+1}, \boldsymbol{\mu}_{k+1}) = (\boldsymbol{\sigma}_k + \alpha_k \mathbf{s}_k, \boldsymbol{\mu}_k + \alpha_k \mathbf{t}_k), \quad (3.9)$$

where  $\alpha_k$  is a step length so that there is enough descent. To choose it, we use the Armijo–Goldstein principle [49], which chooses  $\alpha_k$  as the largest step size in the sequence  $2^{-i}$ ,  $i = 0, 1, \dots$  that satisfies

$$\|r(\sigma_k, \boldsymbol{\mu}_k)\|^2 - \|r(\sigma_k + \alpha_k \mathbf{s}_k, \boldsymbol{\mu}_k + \alpha_k \mathbf{t}_k)\|^2 \geq \frac{1}{2} \alpha_k \|J_k \mathbf{q}_k\|^2$$

This choice of  $\alpha_k$  ensures convergence of the method, provided that  $(\sigma_k, \boldsymbol{\mu}_k)$  is not a critical point [2], and allows us to include an important physical constraint in the inversion algorithm, i.e. the positivity of the solution.

It is well known that the minimization of (3.6) is an extremely ill-conditioned problem. In particular, it has been observed in [12, Fig. 2] that the Jacobian matrix  $J$ , expressed as a function of  $\sigma$ , has a large condition number virtually for each value of  $\sigma$  in the solution domain. We will investigate the behavior of the condition number with respect to the variation of  $(\sigma, \boldsymbol{\mu})$  in Section 3.2.1.

A common remedy to face ill-conditioning consists of regularization, replacing the least-squares problem (3.7) by a nearby problem, whose solution is less sensitive to the error present in the data.

A regularization method which particularly suits our problem, given the size of the matrices involved, is the Truncated Singular Value Decomposition (TSVD); see Section 1.3.2. This method is well suited because the Jacobian matrix  $J_k$  is ill-conditioned and has a well-determined numerical rank; (see [27]). The best rank  $\ell$  approximation ( $\ell \leq p = \text{rank}(J_k)$ ) to the Jacobian matrix, according to the Euclidean norm, can be obtained by the SVD decomposition; see Section 1.2.1. This factorization allows us to replace the ill-conditioned Jacobian  $J_k$  by a well-conditioned low-rank matrix  $A_\ell$ , such that

$$\|J_k - A_\ell\| = \min_{\text{rank}(A)=\ell} \|J_k - A\|.$$

Then, the regularized solution to (3.7) can be expressed as

$$\mathbf{q}^{(\ell)} = -A_\ell^\dagger \mathbf{r} = -\sum_{i=1}^{\ell} \frac{\mathbf{u}_i^T \mathbf{r}}{\gamma_i} \mathbf{v}_i,$$

where  $\mathbf{r} = \mathbf{r}(\sigma_k, \boldsymbol{\mu}_k)$ ,  $\gamma_i$  are the elements of the diagonal matrix  $\Sigma$  in the SVD decomposition, and  $\ell = 1, \dots, p$  is the regularization parameter.

When some kind of *a priori* information on the problem is available, e.g., the solution is a step function, we can apply either the Total Variation regularization (see Section 1.3.3) or some regularization methods in Banach spaces (i.e., complete vector spaces endowed with a norm that only allow

“length” and “distances” between its elements to be measured, without any scalar product). Due to the geometrical properties of Banach spaces, these regularization methods allow to obtain solutions endowed with lower over-smoothness. Another useful property of the regularization in Banach spaces is that the solutions are sparse, that is, in general they can be represented by few values. Indeed, it has been shown that the Banach spaces, with resolution of functional equations in  $L^p$  Banach spaces, with  $1 \leq p < 2$ , leads to solutions which usually have few components. This is very useful when dealing with large scale problems, where sparsity gives rise to low numerical cost in computation and storage [18].

On the other hand, if the solution is a smooth function, it is sometimes useful to introduce a regularization matrix  $L \in \mathbb{R}^{t \times 2n}$  ( $t \leq 2n$ ), whose kernel approximately contains the sought solution [33]. Under the assumption  $\mathcal{N}(J_k) \cap \mathcal{N}(L) = \{0\}$ , problem (3.7) is replaced by

$$\min_{\mathbf{q} \in \mathcal{S}} \|L\mathbf{q}\|, \quad \mathcal{S} = \{\mathbf{q} \in \mathbb{R}^{2n} : J_k^T J_k \mathbf{q} = -J_k^T \mathbf{r}(\sigma_k, \boldsymbol{\mu}_k)\},$$

Very common choices for  $L$  are the discretization of the first and second derivative operators (see Section 1.3.1), which we will denote by  $D_1$  and  $D_2$ , respectively.

The Generalized Singular Value Decomposition (GSVD) of the matrix pair  $(J_k, L)$  is the factorization

$$J_k = \tilde{U} \Sigma_J Z^{-1}, \quad L = \tilde{V} \Sigma_L Z^{-1}. \quad (3.10)$$

By the simultaneous factorization (3.10) it is possible to define a truncated GSVD (TGSVD) solution  $\mathbf{q}^{(\ell)}$ ; see Section 1.2.2 and [28] for details.

In order to find a regularized solution of (3.6), we apply the damped Gauss–Newton method (3.9) which requires at each step the solution of the linear least squares problem (3.7). To solve the latter, our algorithm applies either the TSVD or TGSVD. For a fixed value of the regularization parameter  $\ell$ , we substitute the truncated SVD or GSVD solution of (3.7)  $\mathbf{q}^{(\ell)}$ , obtaining the following iterative method

$$(\sigma_{k+1}^{(\ell)}, \boldsymbol{\mu}_{k+1}^{(\ell)}) = (\sigma_k^{(\ell)} + \alpha_k \mathbf{s}_k^{(\ell)}, \boldsymbol{\mu}_k^{(\ell)} + \alpha_k \mathbf{t}_k^{(\ell)}). \quad (3.11)$$

We denote by  $(\sigma_k^{(\ell)}, \boldsymbol{\mu}_k^{(\ell)})$  the solution at convergence.

In real applications, experimental data are affected by noise, so the data vector in the residual function (3.6) must be expressed as  $\mathbf{b} = \hat{\mathbf{b}} + \mathbf{e}$ , where  $\hat{\mathbf{b}}$  contains the exact data and  $\mathbf{e}$  is the noise vector. If the noise is Gaussian and an accurate estimate of  $\|\mathbf{e}\|$  is available, we can determine  $\ell$  by the Discrepancy Principle [28]; see Section 1.3.4.

In the absence of a trustful estimation of the noise level, many *heuristic methods* have been introduced to approximate a regularization parameter; see Section 1.3.4.

### 3.2.1 Computing the Jacobian matrix

As we saw in the previous section, being able to compute or to approximate the Jacobian matrix  $J$  of  $\mathbf{r}$  is crucial for the implementation of an effective inversion algorithm.

In this section we give the explicit expression of the Jacobian matrix with respect to both the electrical conductivity  $\sigma$  and the magnetic permeability  $\mu$ , which is a completely new contribution. We will show that the complexity of this computation is smaller than required by the finite difference approximation.

#### Jacobian matrix with respect to $\sigma$

Since the following calculus have been done and presented in [12], we will just write two main results that will be useful for our work.

**Lemma 3.2.1** *The derivatives  $Y'_{kj} = \frac{\partial Y_k}{\partial \sigma_j}$ ,  $k, j = 1, \dots, n$ , of the surface admittance (3.1) can be obtained starting from*

$$Y'_{nn} = \frac{1}{2u_n}, \quad Y'_{nj} = 0, \quad j = 1, \dots, n-1,$$

and proceeding recursively for  $k = n-1, n-2, \dots, 1$  by

$$\begin{aligned} Y'_{kj} &= N_k^2 b_k Y'_{k+1,j}, \quad j = n, n-1, \dots, k+1, \\ Y'_{kk} &= \frac{a_k}{2u_k} + \frac{b_k}{2} \left[ N_k^2 d_k - Y_{k+1} \left( d_k Y_{k+1} + \frac{1}{i\mu_k \omega} \right) \right], \\ Y'_{kj} &= 0, \quad j = k-1, k-2, \dots, 1, \end{aligned}$$

where

$$\begin{aligned} a_k &= \frac{Y_{k+1} + N_k \tanh(d_k u_k)}{N_k + Y_{k+1} \tanh(d_k u_k)}, \\ b_k &= \frac{1}{[N_k + Y_{k+1} \tanh(d_k u_k)]^2 \cosh^2(d_k u_k)}. \end{aligned}$$

**Proof 3.2.1** See [12].

**Theorem 3.2.1** The partial derivatives of the residual function  $\mathbf{r}(\boldsymbol{\sigma})$  are given by

$$\frac{\partial r_{ij}^v(\boldsymbol{\sigma})}{\partial \sigma_k} = \begin{cases} \frac{4\rho}{\mu_0\omega_j} \mathcal{H}_0 \left[ \lambda e^{-2h_i\lambda} \frac{\partial R_{\omega_j,0}(\lambda)}{\partial \sigma_k} \right] (\rho), & v = 1, \\ \frac{4}{\mu_0\omega_j} \mathcal{H}_1 \left[ e^{-2h_i\lambda} \frac{\partial R_{\omega_j,0}(\lambda)}{\partial \sigma_k} \right] (\rho), & v = 2, \end{cases}$$

for  $i = 1, \dots, m_h$ ,  $j = 1, \dots, m_\omega$ , and  $k = 1, \dots, n$ . Here  $\mathcal{H}_v$  ( $v = 1, 2$ ) denotes the Hankel transform,  $\rho$  is the inter-coil distance,  $\frac{\partial R_{\omega,0}(\lambda)}{\partial \mu_k}$  is the  $k$ th component of the gradient of the function (3.3)

$$\frac{\partial R_{\omega,0}(\lambda)}{\partial \sigma_k} = \frac{-2\lambda i \mu_0 \omega}{(\lambda + i \mu_0 \omega Y_1(\lambda))^2} \cdot \frac{\partial Y_1(\lambda)}{\partial \sigma_k},$$

and the partial derivatives  $\frac{\partial Y_1(\lambda)}{\partial \sigma_k}$  are given by Lemma 3.2.1.

**Proof 3.2.2** See [12].

#### Jacobian matrix with respect to $\mu$

In its statement we omit, for clarity, the variable  $\lambda$ , [16].

**Lemma 3.2.2** The derivatives  $Y'_{kj} = \frac{\partial Y_k}{\partial \mu_j}$ ,  $k, j = 1, \dots, n$ , of the surface admittance (3.1) can be obtained starting from

$$Y'_{mn} = \frac{\sigma_n}{2\mu_n u_n} - \frac{N_n}{\mu_n}, \quad Y'_{nj} = 0, \quad j = 1, \dots, n-1, \quad (3.12)$$

and proceeding recursively for  $k = n-1, n-2, \dots, 1$  by

$$\begin{aligned} Y'_{kj} &= N_k^2 b_k Y'_{k+1,j}, \quad j = n, n-1, \dots, k+1, \\ Y'_{kk} &= \frac{a_k - b_k N_k Y_{k+1}}{\mu_k^2 \omega} \left( u_k - \frac{\sigma_k}{2N_k} \right) i + \frac{b_k d_k \sigma_k}{2\mu_k} (N_k^2 - Y_{k+1}^2), \\ Y'_{kj} &= 0, \quad j = k-1, k-2, \dots, 1, \end{aligned} \quad (3.13)$$

where

$$\begin{aligned} a_k &= \frac{Y_{k+1} + N_k \tanh(d_k u_k)}{N_k + Y_{k+1} \tanh(d_k u_k)}, \\ b_k &= \frac{1}{[N_k + Y_{k+1} \tanh(d_k u_k)]^2 \cosh^2(d_k u_k)}. \end{aligned} \quad (3.14)$$

**Proof 3.2.3** From the definition of  $N_k(\lambda)$  we obtain

$$\begin{aligned}\frac{\partial u_k}{\partial \mu_j} &= \frac{\partial}{\partial \mu_j} \sqrt{\lambda^2 + i\sigma_k \mu_k \omega} = \frac{1}{2N_k} \frac{\sigma_k}{\mu_k} \delta_{kj}, \\ \frac{\partial N_k}{\partial \mu_j} &= \frac{\partial}{\partial \mu_j} \frac{u_k}{i\mu_k \omega} = \frac{u_k - \frac{\sigma_k}{2N_k}}{\mu_k^2 \omega} i\delta_{kj},\end{aligned}\tag{3.15}$$

where  $\delta_{kj}$  is the Kronecker delta, that is 1 if  $k = j$  and 0 otherwise. The recursion initialization (3.12) follows from  $Y_n = N_n$ ; see Section 3.1. We have

$$\begin{aligned}Y'_{kj} &= \frac{\partial N_k}{\partial \mu_j} a_k + N_k \cdot \frac{\frac{\partial Y_{k+1}}{\partial \mu_j} + \frac{\partial N_k}{\partial \mu_j} \tanh(d_k u_k) + N_k \frac{\partial \tanh(d_k u_k)}{\partial \mu_j}}{N_k + Y_{k+1} \tanh(d_k u_k)} \\ &\quad - N_k a_k \cdot \frac{\frac{\partial N_k}{\partial \mu_j} + \frac{\partial Y_{k+1}}{\partial \mu_j} \tanh(d_k u_k) + Y_{k+1} \frac{\partial \tanh(d_k u_k)}{\partial \mu_j}}{N_k + Y_{k+1} \tanh(d_k u_k)},\end{aligned}$$

with  $a_k$  defined as in (3.14). If  $j \neq k$ , then  $\frac{\partial N_k}{\partial \mu_j} = \frac{\partial u_k}{\partial \mu_j} = 0$  and we obtain

$$Y'_{kj} = N_k^2 \frac{\frac{\partial Y_{k+1}}{\partial \mu_j} (1 - \tanh^2(d_k u_k))}{[N_k + Y_{k+1} \tanh(d_k u_k)]^2} = N_k^2 b_k Y'_{k+1,j}.$$

The last formula, with  $b_k$  given by (3.14), avoids the cancellation in  $1 - \tanh^2(d_k u_k)$ .

If  $j = k$ , after some straightforward simplifications, we get

$$\begin{aligned}Y'_{kk} &= \frac{\partial N_k}{\partial \mu_k} a_k + \frac{N_k}{N_k + Y_{k+1} \tanh(d_k u_k)} \left[ Y'_{k+1,k} (1 - a_k \tanh(d_k u_k)) \right. \\ &\quad \left. + \frac{\partial N_k}{\partial \mu_k} (\tanh(d_k u_k) - a_k) + \frac{d_k \sigma_k}{2 \mu_k} \left( 1 - a_k \frac{Y_{k+1}}{N_k} \right) (1 - \tanh^2(d_k u_k)) \right].\end{aligned}$$

This formula, using (3.14) and (3.15), leads to

$$Y'_{kk} = \frac{\partial N_k}{\partial \mu_k} (a_k - b_k N_k Y_{k+1}) + b_k \frac{d_k \sigma_k}{2 \mu_k} [N_k^2 - Y_{k+1}^2].$$

The initialization (3.12) implies that  $Y'_{kj} = 0$  for any  $j < k$ . In particular  $Y'_{k+1,k} = 0$  and, since  $N_k/u_k$  is constant one obtains the expression of  $Y'_{kk}$  given in (3.13). This completes the proof.

**Theorem 3.2.2** *The partial derivatives of the residual function  $\mathbf{r}(\boldsymbol{\mu})$  are given by*

$$\frac{\partial r_{ij}^v(\boldsymbol{\mu})}{\partial \mu_k} = \begin{cases} \rho^3 \mathcal{H}_0 \left[ \lambda e^{-2h_i \lambda} \frac{\partial R_{\omega_j, 0}(\lambda)}{\partial \mu_k} \right] (\rho), & v = 1, \\ \rho^2 \mathcal{H}_1 \left[ e^{-2h_i \lambda} \frac{\partial R_{\omega_j, 0}(\lambda)}{\partial \mu_k} \right] (\rho), & v = 2, \end{cases}$$

for  $i = 1, \dots, m_h$ ,  $j = 1, \dots, m_\omega$ , and  $k = 1, \dots, n$ . Here  $\mathcal{H}_v$  ( $v = 1, 2$ ) denotes the Hankel transform,  $\rho$  is the inter-coil distance,  $\frac{\partial R_{\omega, 0}(\lambda)}{\partial \mu_k}$  is the  $k$ th component of the gradient of the function (3.3)

$$\frac{\partial R_{\omega, 0}(\lambda)}{\partial \mu_k} = \frac{-2\lambda i \mu_0 \omega}{(\lambda + i \mu_0 \omega Y_1(\lambda))^2} \cdot \frac{\partial Y_1(\lambda)}{\partial \mu_k},$$

and the partial derivatives  $\frac{\partial Y_1(\lambda)}{\partial \mu_k}$  are given by Lemma 3.2.2.

**Proof 3.2.4** *The proof follows easily from Lemma 3.2.2 and from equations (3.3), (3.2), (3.4), and (3.6).*

### 3.3 Software implementation

The inversion algorithm described in the previous sections has been implemented in the Matlab programming language. The numerical experiments were performed on a dual Xeon CPU E5//2620 system (12 cores), running the Debian GNU/Linux operating system and Matlab 9.1.

The main Matlab script driver deals with the reconstruction of the electrical conductivity and the magnetic permeability of the soil. It is based, principally, on a further routine, `emsolvenl`, which solves the non linear model for FDEM with respect to either the conductivity or the permeability. Using the smaller code `tsvdnewt` which applies the Gauss–Newton method for TSVD regularization, `emsolvenl` provides us the following output: the regularization parameter, the regularized solutions, the residuals and the weighted norm for each regularized solution, the errors with respect to the true solution, and the number of failures on the regularization identification. For the forward problem driver calls these other routines: `hratio`, `inphase` and `quadracomp`. The first one computes the complex value of the ratio between the secondary and principal field at the height  $h$  above the ground in a layered conductivity model, while the second and the third ones calculate the in-phase and the quadrature components of the ratio, respectively.

For simplicity's sake, we are working on a graphical user interface (GUI) using GUIDE, the graphical user interface development environment of Matlab. In Fig. 3.2 we show the appearance of this interface.

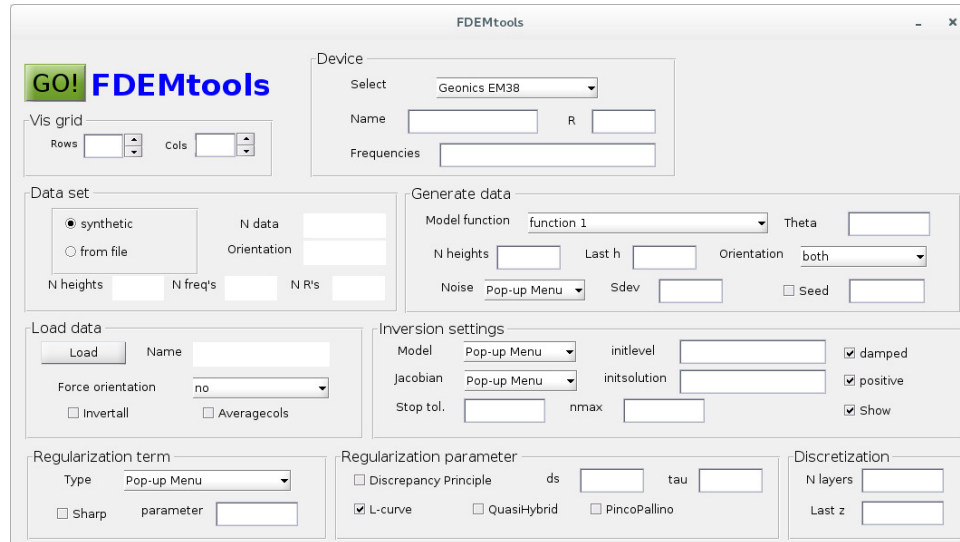


**Figure 3.2:** Graphical user interface using GUIDE, the graphical user interface development environment of Matlab.

Once the graphical interface will be finished, it will be available as a free Matlab package for Analysis and Solution of Inverse problems in Electromagnetic Sounding.

### 3.4 Numerical results

The numerical experiments were performed on a dual Xeon CPU E5//2620 system (12 cores), running the Debian GNU/Linux operating system and Matlab 9.1.

We will study in the next subsections the behavior of the electrical conductivity when the permeability is known and vice versa.

#### Electrical conductivity

To model the conductivity of the subsoil with respect to depth [15], expressed in meters, we chose the test function  $f(z) = e^{-(z-1)^2}$  depicted in Fig. 3.3.

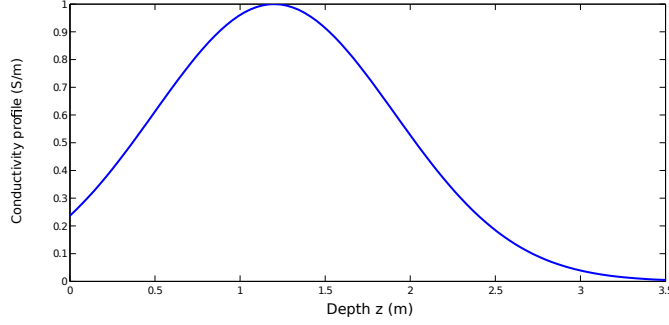


**Figure 3.3:** Graph of the test function used to model conductivity with respect to depth.

For fixed  $n$  and  $d = (3.5 \text{ meters})/n$ , we let  $\sigma_q = f(qd)$  and  $\hat{\mu}_q = \mu_0$  for  $q = 1, \dots, n$ . Then, we apply the forward model described in Section 3.1 to generate the instrument readings

$$\hat{b}_{ij} = M_v(\sigma_q, \hat{\mu}_q; \omega_i, h_j),$$

with  $i = 1, \dots, m_\omega$  and  $j = 1, \dots, m_h$ , corresponding to frequency  $\omega_i = 2\pi f_i$  and height  $h_j$ . Finally, we add Gaussian noise to the synthetic data by the formula

$$\mathbf{b} = \hat{\mathbf{b}} + \frac{\xi \|\hat{\mathbf{b}}\|}{\sqrt{m}} \mathbf{w},$$

where  $\mathbf{w}$  is a vector with normally distributed entries with zero mean and unitary variance,  $m = m_\omega m_h$ , and  $\xi$  is the noise level.

In order to simulate the use of a particular multi-frequency device, the Geophex GEM-2 conductivity meter, we consider the coils to be in the vertical orientation at a fixed distance  $r = 1.66\text{m}$ . The measurement height  $h$  is either  $1\text{m}$  ( $m_h = 1$ ) or  $0.5\text{m}$  and  $1\text{m}$  ( $m_h = 2$ ). Each data set is recorded simultaneously at the operating frequencies  $f_i = 775, 1175, 3925, 9825, 21725, 47025$  (all expressed in Hertz), that is  $m_\omega = 6$ .

In the first experiment we investigate how to choose some of the parameters of the methods, namely, the regularization matrix  $L$ , the heights number  $m_h$ , the number of layers  $n$ , and either the real or the imaginary part of the signal. For each choice of the parameters, we apply the above procedure to compute a synthetic data, we add noise at level  $\xi = 10^{-3}, 10^{-2}$ , and we generate 20 realizations of the random noise vector  $\mathbf{w}$ , to produce 40 test problems. For each test, we measure the relative error

$$E_{\ell_{\text{opt}}} = \frac{\|\sigma - \sigma^{(\ell_{\text{opt}})}\|}{\|\sigma\|},$$

where the regularization parameter  $\ell_{\text{opt}}$  has been chosen in order to minimize the value of  $E_\ell$ ,  $\ell = 1, \dots, p$ , so that the accuracy attained by the method is maximal.

	L	$m_h$	$n = 20$	$n = 30$	$n = 40$
$\mathcal{R}$	$I$	1	3.6e-01	3.7e-01	3.7e-01
		2	4.5e-01	4.5e-01	4.4e-01
	$D_1$	1	3.0e-01	3.3e-01	2.9e-01
		2	2.4e-01	2.4e-01	2.3e-01
	$D_2$	1	2.4e-01	2.1e-01	2.8e-01
		2	2.5e-01	2.5e-01	2.3e-01
$\mathcal{I}$	$I$	1	3.2e-01	3.9e-01	4.0e-01
		2	3.0e-01	3.4e-01	3.4e-01
	$D_1$	1	1.9e-01	2.3e-01	1.9e-01
		2	2.1e-01	1.9e-01	1.9e-01
	$D_2$	1	2.3e-01	2.0e-01	2.4e-01
		2	2.1e-01	2.2e-01	2.1e-01

**Table 3.1:** Best accuracy attainable by the method for both the real part,  $\mathcal{R}$ , and the imaginary part,  $\mathcal{I}$ , of the signal and for selected choices of the parameters. Each entry of the table is the average of  $E_{\ell_{\text{opt}}}$  across 40 experiments, with two noise levels and 20 noise realizations.

For each combination of the selected parameters, we report in Table 3.1 the average of the values of  $E_{\ell_{\text{opt}}}$  across the available 40 test problems. The table confirms that the choice of the regularization matrix  $L = I$  produces the least accurate results mainly because our test function is smooth, as observed in [12], while  $D_1$  and  $D_2$  (see Section 1.3.1) are more or less equivalent. The method is not very sensitive upon the number of layers  $n$  and the accuracy does not improve substantially when  $m_h = 2$ , with respect to  $m_h = 1$ . Since increasing  $m_h$  implies a larger data acquisition time, in our next experiments we will set  $L = D_2$ ,  $m_h = 1$ , and  $n = 30$ . Both the real and imaginary part of the signal seem to contain the same amount of information about the solution, with the quadrature component reaching a slightly better accuracy. This suggests that both components should be considered in the solution of the least squares problem (3.6).

In our next experiment, we consider the presence of electromagnetic materials in the subsoil ( $\mu > \mu_0$  in some layer) and analyze the effectiveness of

the L-curve as a method to choose the regularization parameter  $\ell$ . Table 3.2 is divided into 2 main blocks: the first 2 rows concern the optimal choice  $\ell = \ell_{\text{opt}}$ , the last 2 rows the choice  $\ell = \ell_{\text{L-curve}}$ , produced by the L-curve. The integer number on the bottom of each row represents the number of *failures*, that is how many of the 40 experiments produced a relative error larger than 1.5. We verified that when the error is below this limit it is still possible to recover from the solution significant information, e.g., the localization in depth of the maximal conductivity. The real number on the top of each row represents the average of  $E_{\ell_{\text{opt}}}$  (first two rows) and  $E_{\ell_{\text{L-curve}}}$  (last two rows) across the acceptable errors. The first column contains the result corresponding to  $\hat{\mu}_q = \mu_0$ ,  $q = 1, \dots, n$ , as for the previous experiment. From the second to fourth column, the magnetic permeability of each layer is set to

$$\hat{\mu}_q = \mu_r \mu_0 f(qd) + \mu_0, \quad q = 1, \dots, n,$$

where the relative magnetic permeability  $\mu_r = 10, 10^2, 10^3$  ( $\mu_r = \mu/\mu_0$ ), and  $f(z)$  is the function of Fig. 3.3. The largest value of  $\mu_r$  roughly correspond to the magnetic permeability of iron.

	$\mu_0$	$\mu_r = 10$	$\mu_r = 10^2$	$\mu_r = 10^3$
optimal - $\mathcal{R}$	2.3e-01	4.3e-01	5.3e-01	5.5e-01
	0	13	9	19
optimal - $\mathcal{I}$	2.4e-01	5.3e-01	4.5e-01	7.1e-01
	0	6	4	12
L-curve - $\mathcal{R}$	2.6e-01	6.3e-01	4.7e-01	5.4e-01
	0	20	18	27
L-curve - $\mathcal{I}$	2.6e-01	4.2e-01	5.5e-01	7.4e-01
	0	23	10	16

**Table 3.2:** Results for different values of the relative magnetic permeability  $\mu_r$ . Each row displays the average error and the number of *failures* across 40 experiments; see text. The upper block concerns the optimal choice of  $\ell$ , the bottom block the choice by the L-curve.

From Table 3.2, it is immediately evident that the inversion problem is much harder to solve when  $\mu_r > 1$ . The considerable number of experiments whose relative error is larger than 1.5 (the *failures*) suggests that

the algorithm, originally conceived for constant permeability  $\mu_0$ , should be modified in order to deal with the general situation. Nevertheless, when the algorithm does not fail the error for  $\mu_r > 1$  is only slightly larger than for  $\mu = \mu_0$ . Preliminary results on field data in [3] suggest that the solutions produced by the method are still accurate for moderate values of  $\mu_r$ .

When the regularization parameter  $\ell$  is chosen by the L-curve, rather than optimally, the performance of the method gets worse, in terms of number of failures, but the error is still acceptable. This experiment confirms that both the real and imaginary part of the signal contain substantial information about the solution.

To illustrate the effect of regularization on the computed solutions we depict in Fig. 3.4 the first 4 regularized solutions  $\sigma^{(\ell)}$ , that is the limit solutions of the iterative scheme (3.11) when  $\ell = 1, 2, 3, 4$ . This experiment is characterized by constant permeability  $\mu_0$  and noise level  $\zeta = 10^{-3}$ ; the solution (green line) is computed by minimizing the real part of the signal. The exact solution is displayed in each graph by a blue line. The graphs show that when the parameter is smaller than the optimal value, the solution is over-regularized and it is just a sketch of the correct conductivity profile. On the contrary, when  $\ell$  is too large there are no constraints on the error propagation, and the under-regularized solution exhibits abnormal oscillations.

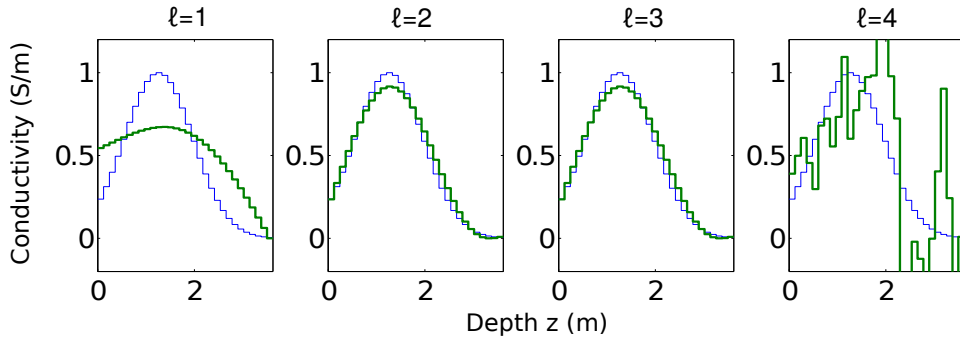


**Figure 3.4:** Plot of the first 4 regularized solutions, computed by minimizing the real part of the signal, compared to the exact solution. The magnetic permeability  $\mu = \mu_0$  is constant, the noise level is  $\zeta = 10^{-3}$ .

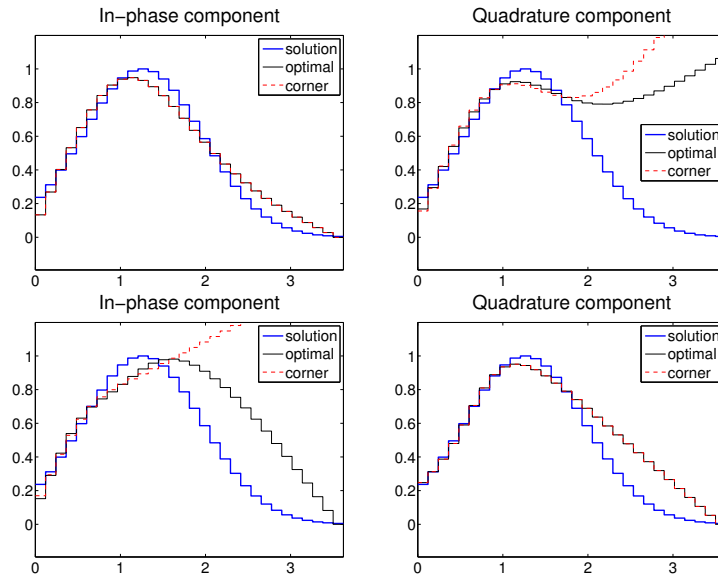


**Figure 3.5:** Solution obtained by minimizing the real part of the data (left) or the imaginary part (right);  $\xi = 10^{-3}$ ,  $\mu_r = 10$  in the top row,  $\mu_r = 10^2$  in the bottom row. The value of  $\ell$  is chosen either optimally or by the L-curve.

In Fig. 3.5 we compare the solution obtained by minimizing the real part of the data (left column) to the one corresponding to the imaginary part (right column). The blue line is the exact solution, the black line is the optimal solution, the dashed line represents the L-curve solution. The graphs in the top row correspond to  $\mu_r = 10$  and  $\xi = 10^{-3}$ . For the real part, the L-curve selects the optimal parameter  $\ell = 2$ , with an error  $E_{\ell_{\text{opt}}} = E_{\ell_{\text{L-curve}}} = 0.37$ ; for the imaginary part, the algorithm fails. The bottom row of Fig. 3.5 displays a similar experiment, with  $\mu_r = 10^2$ . In this case, the L-curve correctly identifies the regularization parameter for the quadrature part minimization ( $\ell = 3$ ), with an error  $E_{\ell_{\text{opt}}} = E_{\ell_{\text{L-curve}}} = 0.70$ . On the contrary, while the optimal error for the real part is  $E_{\ell_{\text{opt}}} = 1.36$  ( $\ell = 3$ ), the L-curve chooses the parameter  $\ell = 2$ , producing an incorrect solution.

Some other numerical experiments for finding the imaginary part of the electrical conductivity have been studied in [12].

### Magnetic permeability

In the first experiment, we investigate the ill-conditioning of the problem. We assume the loop-loop device is in the vertical orientation with a constant

operating frequency  $f = 14600\text{Hz}$  and an inter-coil distance  $\rho = 1\text{m}$ ; these features are typical of one of the most widely used device, the Geonics EM38. We let  $n = m_h = 10, 20, 30, 40$ , that is, we simulate a dataset with measurements detected at heights  $h_i, i = 1, \dots, m_h$ , starting from the ground level up to  $1.9\text{m}$ , and we consider a discretization below the surface with the same number  $n$  of layers, until the depth of  $3\text{m}$ . For each choice of  $n$ , we evaluate the Jacobian matrix  $J$  at 100 random vectors in  $\mathbb{R}^n$ , with entries distributed in the interval  $[\mu_0, \mu_r \mu_0]$ , for a chosen value of  $\mu_r$ . For each example, we record the singular values of  $J$ , as computed by the `svd` function of Matlab. The scaling parameter  $\mu_r$  represents the maximum value allowed for the relative permeability, and is initially set to 100. The layers conductivity is fixed at a constant value.

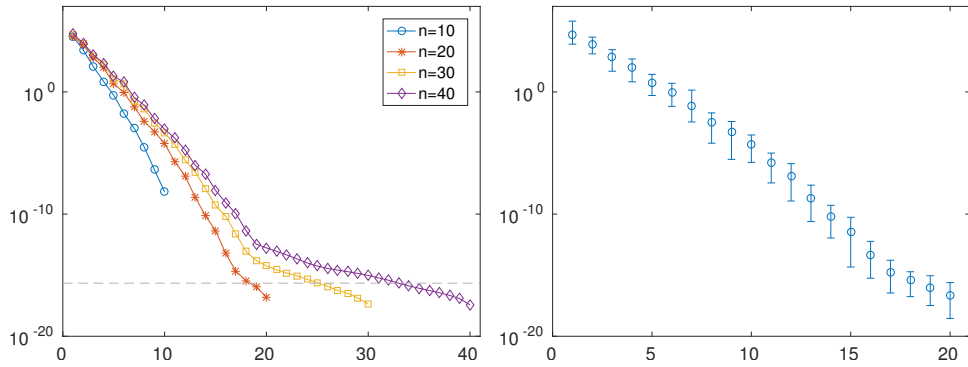


**Figure 3.6:** Average of the singular values of the Jacobian  $J(\mu)$  computed on 100 random points in  $\mathbb{R}^n$ , for  $m = n = 10, 20, 30, 40$  (left-hand side); each component of  $\mu$  is in  $[\mu_0, 100\mu_0]$ . The right-hand side graph shows the average singular values for  $n = 20$  together with their maximum and minimum value across the random tests.

The left-hand side graph in Fig. 3.6 displays the average of the singular values for each choice of  $n$ ; the dashed line marks the value of the machine epsilon  $2.2 \cdot 10^{-16}$ . It is immediate to observe that the singular values decay exponentially. The deviation from the initial decay rate, observed for  $n > 20$ , is likely to be due to the error propagation caused by ill-conditioning, so it is reasonable to conjecture that the condition number increases with the size of the problem. The right-hand side graph in Fig. 3.6 shows the average of the singular values for  $n = 20$ , together with their maximum and minimum value across the 100 performed random tests. The graph

shows that the variance from the average is small, so that the Jacobian is uniformly ill-conditioned for permeabilities in  $[\mu_0, \mu_r \mu_0]$ , when  $\mu_r = 100$ .

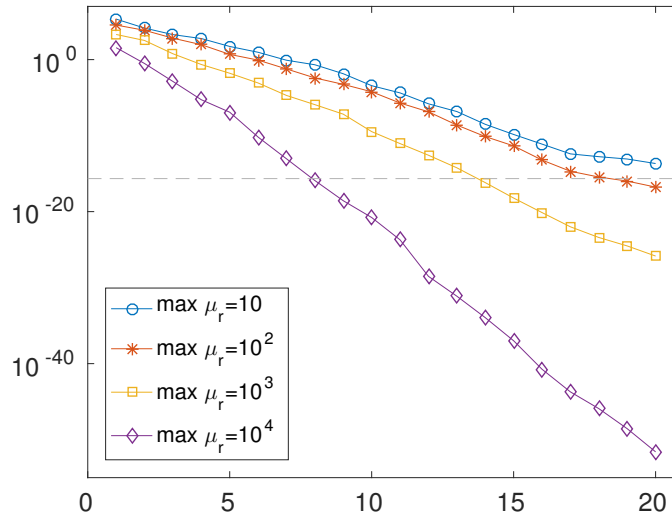


**Figure 3.7:** Average of the singular values of the Jacobian  $J(\mu)$  computed on 100 random points in  $\mathbb{R}^n$ , for  $m = n = 20$ ; each component of  $\mu$  is in  $[\mu_0, \mu_r \mu_0]$ , with  $\mu_r = 10, 10^2, 10^3, 10^4$ .

Fig. 3.7 reports the average of the computed singular values when the maximum relative permeability  $\mu_r$  takes the values  $10, 10^2, 10^3, 10^4$ . The conditioning of the problem increases dramatically when the magnetic permeability is large, making it much harder to solve the inversion problem. This typically happens in the presence of ferromagnetic materials in the subsoil; consider that for iron  $\mu_r \simeq 5 \cdot 10^3$ . The fact that the problem is severely ill-conditioned also for small values of  $\mu_r$  is in accordance with [12, Fig. 2], where  $\mu_r = 1$  and the values of the conductivity are varied.

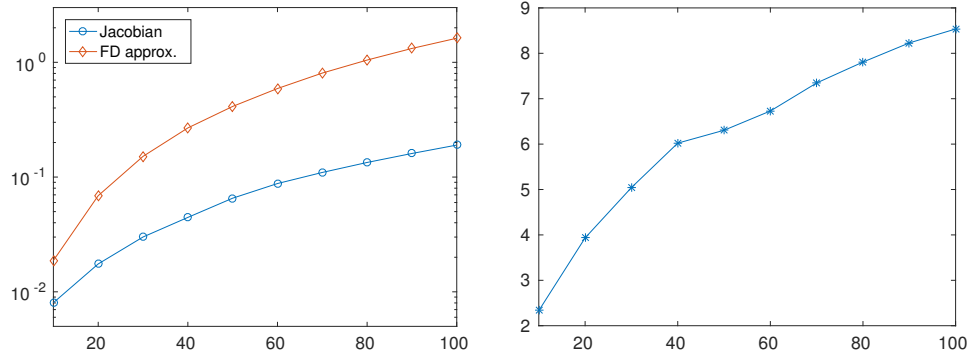


**Figure 3.8:** Efficiency in the evaluation of the Jacobian  $J$  of size  $n = 10, 20, \dots, 100$ , compared to a finite difference approximation. The left-hand side graph displays the computing time in seconds for the two approaches; the right-hand side graph reports the speedup factor, i.e., the ratio between the timings of finite difference and the exact Jacobian.

Let us consider the following approximation of the partial derivatives of the residual components

$$\frac{\partial r_i(\boldsymbol{\mu})}{\partial \mu_j} \simeq \frac{r_i(\boldsymbol{\mu} + \boldsymbol{\delta}_j) - r_i(\boldsymbol{\mu})}{\delta}, \quad i, j = 1, \dots, n, \quad (3.16)$$

where  $\boldsymbol{\delta}_j = \delta \mathbf{e}_j = (0, \dots, 0, \delta, 0, \dots, 0)^T$  and  $\delta$  is a fixed constant. Resorting to a finite difference approximation of the Jacobian is a common approach in the solution of nonlinear problems; see, e.g., [33]. In [12] it was pointed out that the exact computation of the Jacobian of the residual  $\mathbf{r}(\boldsymbol{\sigma})$ , expressed as a function of the conductivity vector  $\boldsymbol{\sigma}$ , has a smaller computational complexity than its finite difference approximation. This was a relevant observation, since in many practical applications it is often assumed that the exact knowledge of the Jacobian is not strictly required, as its approximation leads to an algorithm with equivalent performance. The superiority in term of complexity of the exact evaluation of  $J$  is confirmed also when the residual vector is seen as a function of  $\boldsymbol{\mu}$ . Fig. 3.8 shows how the two approaches perform when the size of the problem increases. For  $m_h = n = 10, 20, \dots, 100$ , we compute  $J$  by the exact formulas of Theorem 3.2.2 and by its finite difference approximation. The execution time is averaged over 100 repetitions of the computation. Fig. 3.8 reports the computing time for the two algorithms (left-hand side graph) together with the speedup factor (on the right), which we define as the ratio between the two timings. It is

clear that the efficiency of the exact computation increases with the size of the problem.

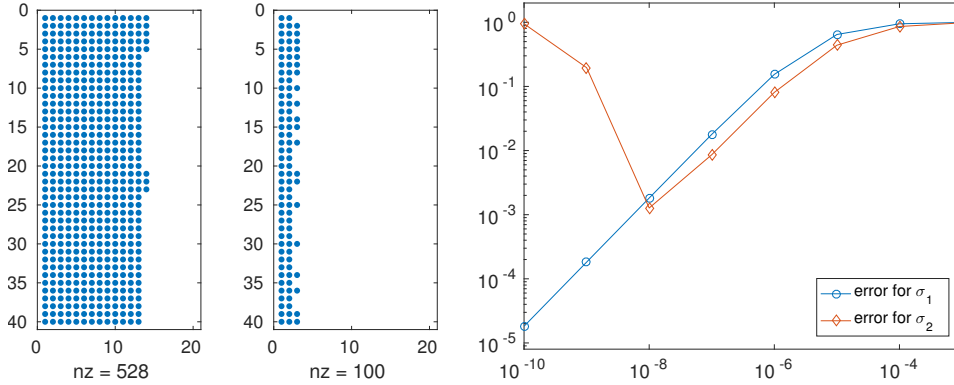


**Figure 3.9:** The “spy plot” on the left shows the pattern of the nonzero elements for the Jacobian  $J$  of size  $40 \times 20$ , as computed by the formulas in Section 3.2.1. The central graph displays the same information for  $\tilde{J}$ , obtained by the approximation (3.16). The right-hand side plot represents the relative error for the first two singular values with respect to the variation of  $\delta$  in (3.16).

The exact Jacobian outperforms the finite difference approximation also from the point of view of accuracy, as the latter suffers from severe error propagation due to numerical cancellation. We let  $\mu_i \in [\mu_0, \mu_r \mu_0]$ ,  $i = 1, \dots, n$ , with  $\mu_r = 10$ , and compare the Jacobian  $J(\mu)$  of size  $40 \times 20$  to its approximation  $\tilde{J}(\mu)$  obtained by (3.16) with  $\delta = 10^{-6}$ . The two left-hand side graphs in Fig. 3.9 display the pattern of the nonzero elements of  $J$  and  $\tilde{J}$ . The norm of the columns of  $J$  decays very quickly, leading to zero-out its entries starting from the 15th column, because of underflow. When we approximate the Jacobian by (3.16) for any  $\delta \leq 10^{-3}$ , cancellation makes the elements drop to zero already from the fourth columns; see the central graph in Fig. 3.9. By computing the singular values  $\sigma_i(J)$  and  $\sigma_i(\tilde{J})$  of the two matrices  $J$  and  $\tilde{J}$ , respectively, we can see that  $\sigma_i(J) = 0$  when  $i \geq 12$  for the exact Jacobian, while only the first three singular values of  $\tilde{J}$  are different from zero, denoting a dramatic loss of information.

The right-hand side of Fig. 3.9 shows the relative differences

$$\frac{\sigma_i(J) - \sigma_i(\tilde{J})}{\sigma_i(J)}, \quad i = 1, 2,$$

when  $\delta$  in (3.16) takes the values  $10^{-3}, 10^{-4}, \dots, 10^{-10}$ . While the approxi-

mation error for the first singular value decays monotonically, the error for the second one diverges when  $\delta < 10^{-8}$ . The situation is even worse for the third singular value, since  $\sigma_3(\tilde{J})$  grows from  $1.2 \cdot 10^{-12}$  to  $1.3 \cdot 10^{-5}$  when  $\delta = 10^{-3}, 10^{-4}, \dots, 10^{-10}$ , while  $\sigma_3(J) = 2.0 \cdot 10^{-20}$ .

The accuracy of the finite difference approximation degrades in the presence of a larger magnetic permeability, as for  $\mu_i \in [\mu_0, \mu_r \mu_0]$  with  $\mu_r \geq 10^2$  only one column (and consequently one singular value) of  $\tilde{J}(\mu)$  is different from zero, while the exact Jacobian preserves a larger number of nonzero columns.

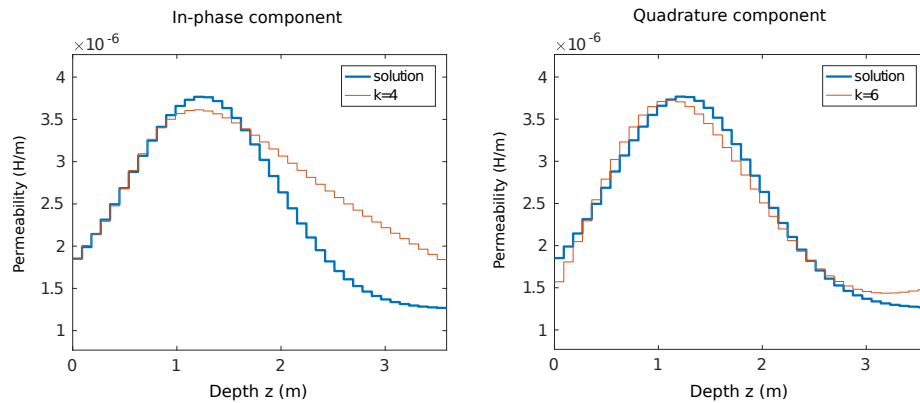
In order to verify the performance of the new formulas for the Jacobian in the inversion of EM data, we considered the following *a priori* model for the magnetic permeability as a function of depth

$$\mu_\theta(z) = \mu_0(\theta e^{-(z-1.2)^2} + 1),$$

where  $\theta$  is a parameter to be chosen. The permeability takes values in  $[\mu_0, (\theta + 1)\mu_0]$  and has a maximum at  $z = 1.2\text{m}$ . The conductivity of the subsoil is assumed to be known in advance and to be strongly correlated to the values of  $\mu_\theta(z)$ ; we represent it by the model function  $\sigma_\theta(z) = \theta e^{-(z-1.2)^2}$ , with values in  $[0, \theta]$ .

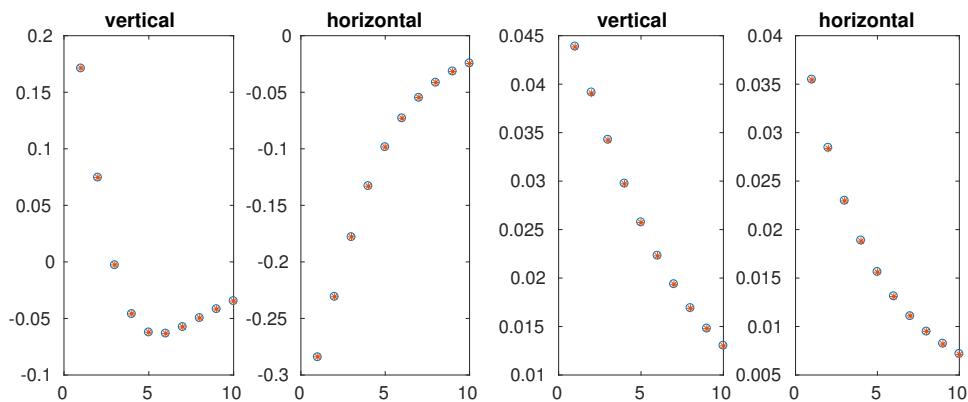
A synthetic data set is constructed by applying the forward model described in Section 3.1 to the sampling of  $\mu_\theta(z)$  and  $\sigma_\theta(z)$  at the depths  $z_i = 3.5(i - 1)/(n - 1)$ ,  $i = 1, \dots, n$ . We initially fix  $m_h = 10$ ,  $n = 40$ , and let the measurement heights be  $h_i = 1.9i/m_h$ ,  $i = 1, \dots, m_h$ . We assume one operating frequency  $f = 14600\text{Hz}$  for the instrument ( $m_\omega = 1$ ), and both the horizontal and the vertical orientations. The data set is contaminated by additive white noise, with mean value zero and standard deviation  $\xi/\sqrt{n}$ . Since the noise level is known, we can estimate the regularization parameter  $\ell$  in (3.11) by the Discrepancy Principle (1.3.4), where we set  $\|\mathbf{e}\| = \xi = 10^{-3}$  and  $\tau = 1.5$ .

Fig. 3.10 shows the model solution compared to the approximated solutions obtained by applying our inversion algorithm either to the real part or to the imaginary part of the data values. We fixed  $\theta = 2$ , corresponding to a moderate variation of the magnetic permeability. The solutions identified by the Discrepancy Principle lead both to a good global reconstruction of the test function and a reasonably accurate localization of its maximum.



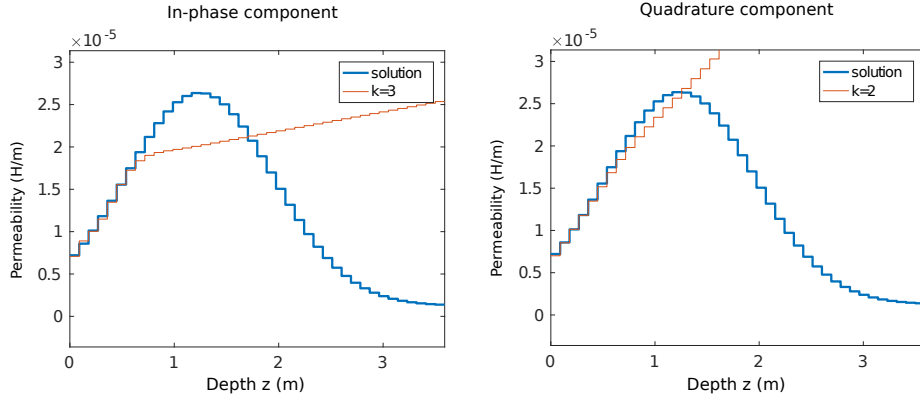
**Figure 3.10:** Regularized solution obtained by fixing  $\theta = 2$ ,  $m_h = 10$ ,  $m_\omega = 1$ ,  $n = 40$ , and  $\zeta = 10^{-3}$ . On the left, the result obtained by inverting the in-phase component of the data; on the right, the solution corresponding to the quadrature component.

Fig. 3.11 displays the data set and the measurement predicted by the model for both the regularized solutions. A good matching between the measured and the predicted data values guarantees a small residual.



**Figure 3.11:** Measured (circles) and predicted (asterisks) data values for the two solutions displayed in Fig. 3.10; we display the data for both the vertical and the horizontal orientation of the device. The graphs on the left are obtained by inverting the in-phase component of the measured signal; the graphs on the right correspond to the quadrature component.

This is, in general, an indication that the chosen initial solution converged to an accurate local solution, and that the algorithm was successful. In these experiments we chose  $\boldsymbol{\mu}^{(0)} = 2\mu_0\mathbf{u}$ , with  $\mathbf{u} = (1, \dots, 1)^T$ .



**Figure 3.12:** Regularized solution obtained by fixing  $\theta = 20$ ,  $m_h = 20$ ,  $m_\omega = 1$ ,  $n = 40$ , and  $\zeta = 10^{-3}$ . On the left, the result obtained by inverting the in-phase component of the data; on the right, the solution corresponding to the quadrature component.

The graphs in Fig. 3.12 show the solutions obtained by fixing  $\theta = 20$ , that is, assuming a wider variation of the magnetic permeability. All the other parameters are unchanged, except  $m_h = 20$ . The solutions displayed in the graphs are obtained by selecting the initial solution which produces in the most significant converged solution, that is,  $\boldsymbol{\mu}^{(0)} = 8\mu_0\mathbf{u}$  for the in-phase component inversion,  $\boldsymbol{\mu}^{(0)} = 10\mu_0\mathbf{u}$  for the quadrature component inversion. Both experiments do not correctly reproduce the behavior of the solution: despite the size of the data is doubled, the algorithm is only able to detect the shape of the solution up to the depth of about 1 meter. We remark that the quality of the approximations does not improve by overestimating the value of the regularization parameter indicated by the Discrepancy Principle.

Varying the instrument height, that is, considering many  $h_i$  values, has been the standard approach with first generation devices, in order to obtain multiple data for each spatial point. This redundant information is required whenever one pretends to reconstruct the distribution of the electromagnetic features of the subsoil with respect to depth. Last generation instruments, however, are either endowed with more than two coils, allowing for multiple values of the inter-coil distance  $\rho$ , or are able to perform simultaneous

measurements with different angular frequencies  $\omega_j = 2\pi f_j$ . The Geophex GEM-2 falls into the last class of devices; it is endowed with two coils at a distance  $\rho = 1.66\text{m}$ , and it can be configured to use up to 10 frequencies for each data acquisition. In the following experiment we assume that each measurement is performed at 6 different frequencies, namely  $f = 775\text{Hz}, 1175\text{Hz}, 3925\text{Hz}, 9825\text{Hz}, 21725\text{Hz}, 47025\text{Hz}$ , with the instrument at the height of 1m, and using both the orientations. This means that we fix  $m_h = 1, m_\omega = 6, \nu = 1, 2$ , and apply the inversion algorithm with  $m = 12$  data values. The noise level is the same than before, i.e.,  $\zeta = 10^{-3}$ , and the regularization parameter is chosen by the Discrepancy Principle (1.3.4), with  $\tau = 1.5$ .

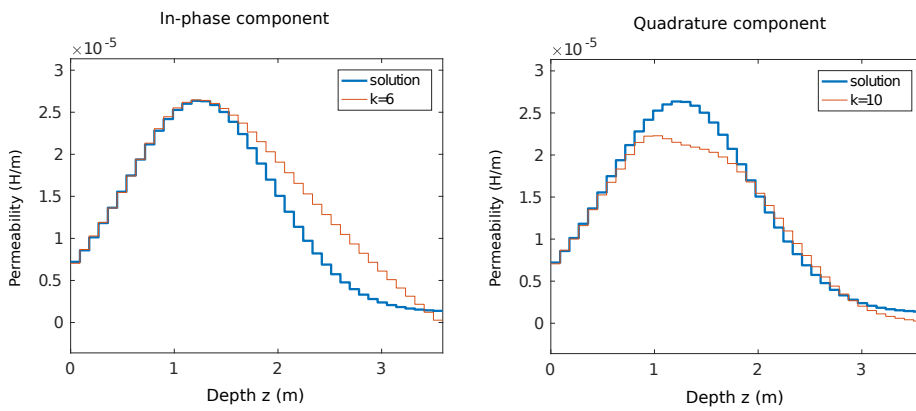


**Figure 3.13:** Regularized solution obtained by fixing  $\theta = 20, m_h = 1, m_\omega = 6, n = 40$ , and  $\zeta = 10^{-3}$ . On the left, the result obtained by inverting the in-phase component of the data; on the right, the solution corresponding to the quadrature component.

We report in Fig. 3.13 the results obtained by assuming the same strong variation of the permeability ( $\theta = 20$ ) of the preceding experiment. The two graphs are computed by inverting either the in-phase or the quadrature component of the signal. The accuracy of the reconstructions demonstrates that varying the operating frequency of the device produces a data set containing much richer information than varying its height, and suggests that this approach should be preferred in practical EM data inversion.



# 4

## Time domain electromagnetic (TDEM) response of a conductive permeable sphere

The reaction of a spherical conducting ore zone to an impressed magnetic field is of great practical importance, e.g., discover of unexploded ordnance. The general problem of a sphere under the influence of an impressed electromagnetic field has been firstly investigated, in a general manner, by Debye [10] in 1909 and a more specific problem of a conducting sphere in the presence of a magnetic dipole has been treated by March [44] in 1929.

When a conducting body is immersed in a time-varying magnetic field, eddy currents are induced. These produce, in turn, a secondary magnetic field which may be detected by an observer external to the sphere. It has been demonstrated that a measurement of the external field can be used to estimate the conductivity of the body if certain assumptions are valid. Ward, in 1953 [80], has shown that the conductivity and permeability of geological core specimens from diamond drill holes may be determined by examining the frequency dependence of the time-harmonic response of the specimen. In principle, the same information should also be available from the time-response of the specimen for a suddenly applied magnetic field [77].

In 1951 Wait [77] dealt with a special case of a conducting sphere embedded in a relatively poorly conducting medium [79]. The applied field was assumed to be uniform in the region of the sphere. The secondary fields for sinusoidally varying primary fields were developed from first principles. This is a special case of the Debye and March solutions when the external medium has a small conductivity. The transient solutions can be obtained directly by suitable integrations of the steady state solutions. The secondary field responses to a step-function type of magnetic applied field are in turn explicitly calculated.

This chapter involves a work in progress which is concerned with estimating the magnetic permeability, the conductivity and the radius of a sphere imbedded in a uniform time-varying magnetic field via exponential sums. We first find a series expansion for the magnetic fields inside and outside the sphere, after that we impose regularity (i.e. continuity of the normal flux and tangential magnetic field) at the boundary in order to explicitly compute coefficients of the series. Then, we find a series expansion for the step-function and finally compute the parameters of the materials by means of the (measured) values of the step-function (i.e. the inverse problem).

#### 4.1 Setting of the problem

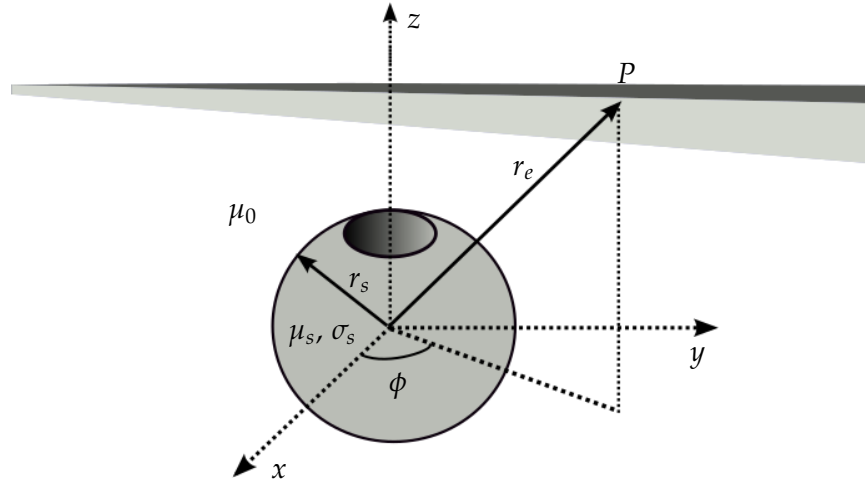


Figure 4.1: The coordinate system for the conducting sphere.

Let us consider a sphere of radius  $r_s$ , conductivity  $\sigma_s$  and permeability  $\mu_s$ , and assume that, in the neighborhood of the sphere, a uniform magnetic field  $H = H_0 e^{i\omega t}$ , with intensity  $H_0$ , is applied at the time  $t$  with a propagation constant

$$\gamma_e = \sqrt{i\mu_e\omega(\sigma_e + i\epsilon_e\omega)}, \quad (4.1)$$

where  $\epsilon_e, \mu_e, \sigma_e$  denotes the dielectric constant, the permeability and the conductivity of the external medium, respectively. Assuming the existence

of a uniform external applied field means that the radius of the sphere is much less than a wavelength in the external medium, i.e. the radius and the above propagation constant satisfy the constrain

$$|\gamma_e r_s| \ll 1. \quad (4.2)$$

We introduce a spherical polar coordinate system centered at the center of the sphere (see Fig. 4.1) and, without loss of the generality, assume that the polar axis (i.e. the  $z$  axis) is taken parallel to the external magnetic field. The magnetic field must be expressible everywhere in terms of the magnetic vector  $[F]_z$  with only the  $z$  component since the resulting circulating or eddy currents are only in the  $\phi$  direction,

$$H = -(\sigma + i\omega)[F]_z + \frac{1}{i\mu\omega} \text{grad div}[F]_z.$$

Hence, the magnetic vector potential for the primary field is given by

$$[F_0]_z = -(\sigma_e + i\epsilon_e\omega)H_0.$$

The magnetic field outside the sphere has a potential vector given by (see [7])

$$[F_e]_z = -(\sigma_e + i\epsilon_e\omega)H_0 + \frac{i\mu_e\omega}{r_e} \sum_{n=0}^{\infty} a_n \widehat{K}_n(\gamma_e r_e) P_n(\cos \theta), \quad (4.3)$$

where  $r_e$  is the distance between the center of the sphere and the observation point  $P \equiv P(x, y, z)$ ,  $P_n$  denotes the Legendre polynomials [23] and  $\widehat{K}_n$  are the modified spherical Bessel functions of the second kind [23] defined as  $\widehat{K}_n = \sqrt{\frac{2z}{\pi}} K_{n+\frac{1}{2}}$ , with  $K_{n+\frac{1}{2}}$  the modified Bessel functions of the second kind [82].

On the other hand, denoting by

$$\gamma_s = \sqrt{i\mu_s\omega(\sigma_s + i\epsilon_s\omega)}$$

the propagation constant of the sphere, the vector magnetic field inside the sphere is

$$[F_s]_z = \frac{i\mu_s\omega}{r_s} \sum_{n=0}^{\infty} b_n \widehat{I}_n(\gamma_s r_s) P_n(\cos \theta) \quad (4.4)$$

where  $\widehat{I}_n$  is the modified spherical Bessel functions of the first kind [23] defined as  $\widehat{I}_n = \sqrt{\frac{\pi z}{2}} I_{n+\frac{1}{2}}$ , with  $I_n$  the modified Bessel functions of the first kind [82].

The two magnetic fields along the boundary, that is when  $r_s = r_e \equiv \rho$ , has to assure that the normal flux density has to be continuous as well as the tangential magnetic field. This implies that in (4.3) and (4.4) all coefficients with  $n \neq 0$  vanish and (4.3) and (4.4) become

$$[F_e]_z = -(\sigma_e + i\omega\epsilon_e)H_0 + a_0 \mu_e i\omega \frac{e^{(-\gamma_e \rho)}}{\rho}, \quad [F_s]_z = ib_0 \mu_s \omega \frac{\sinh(\gamma_s \rho)}{\rho}$$

where  $a_0$  and  $b_0$  satisfy the following system

$$\begin{cases} \frac{1}{\rho} \frac{\partial F_s}{\partial \rho} - \gamma_s^2 F_s = \frac{1}{\rho} \frac{\partial F_e}{\partial \rho} - \gamma_e^2 F_e, \\ \mu_s \left( \frac{\partial^2 F_s}{\partial^2 \rho} - \gamma_s^2 F_s \right) = \mu_e \left( \frac{\partial^2 F_e}{\partial^2 \rho} - \gamma_e^2 F_e \right). \end{cases}$$

By solving the above system we find that the potential outside the sphere shell corresponds to an uniform field  $H_0$  plus a dipole field having the following dipole moment  $a_0$  oriented parallel to  $H_0$ :

$$a_0 = e^{\gamma_e \rho} H_0 \rho^3 \frac{\gamma_e^2 (\epsilon_e i\omega + \sigma_e)}{2\mu_e i\omega} \frac{\gamma_s \rho (2\mu_s + \mu_e) \cosh(\gamma_s \rho) - (2\mu_s + \mu_e + (\gamma_s \rho)^2 \mu_e) \sinh(\gamma_s \rho)}{A \cosh(\gamma_s \rho) + B \sinh(\gamma_s \rho)},$$

with

$$\begin{aligned} A &= \gamma_s \rho (-\mu_e (1 + \gamma_e \rho) + \mu_s (1 + \gamma_e \rho + (\gamma_e \rho)^2)), \\ B &= \mu_e (1 + \gamma_e \rho) (1 + (\gamma_s \rho)^2) - \mu_s (1 + \gamma_e \rho + (\gamma_e \rho)^2). \end{aligned}$$

Inside the sphere, there is a uniform magnetic field parallel to  $H_0$  and equal in magnitude to  $-b_0$  with

$$b_0 = H_0 \rho^3 \frac{\gamma_e^2 (\epsilon_e i\omega + \sigma_e) \mu_e}{2\mu_s i\omega} \frac{(3 + 3\gamma_e \rho + (\gamma_e \rho)^2)}{A \cosh(\gamma_s \rho) + B \sinh(\gamma_s \rho)}.$$

Let us note that under the assumption (4.2), taking (4.1) into account and setting  $\alpha = \gamma_s \rho$ , the previous coefficients can be written as

$$\begin{aligned} a_0 &= H_0 \rho^3 (\epsilon_e i\omega + \sigma_e)^2 \frac{\alpha (2\mu_s + \mu_e) \cosh(\alpha) - (2\mu_s + \mu_e + \alpha^2 \mu_e) \sinh(\alpha)}{2\alpha (\mu_s - \mu_e) \cosh(\alpha) + 2(\mu_e (\alpha^2 + 1) - \mu_s) \sinh(\alpha)}, \\ b_0 &= H_0 \rho^3 (\epsilon_e i\omega + \sigma_e)^2 \mu_e^2 \frac{3}{2\alpha (\mu_s - \mu_e) \cosh(\alpha) + 2(\mu_e (\alpha^2 + 1) - \mu_s) \sinh(\alpha)}. \end{aligned}$$

From now on, we will assume that the conductivity of the external field is zero ( $\sigma_e = 0$ ) and the permeability of the both the sphere and the external field  $\mu_s$  and  $\mu_e$  coincide with the one of free space, that is,  $\mu_0 = 4\pi 10^{-7}$ . So,

$$a_0 = -\frac{3}{2} H_0 \rho^3 (\epsilon_e s)^2 \chi(s), \quad s = i\omega,$$

where the induced magnetic dipole moment factor  $\chi(s)$  is

$$\chi(s) = \frac{1}{\alpha^2} - \frac{\cosh(\alpha)}{\alpha \sinh(\alpha)} + \frac{1}{3}.$$

We can investigate the corresponding transient problem where the approximations are made so that  $|\gamma_e \rho| \ll 1$  and  $\sigma_s \gg \epsilon_e \omega$ , for important frequencies in the spectrum. This will be valid for a step function source magnetic field when the measuring time of the field response is always such that  $t \gg \sigma_e \mu_0 \rho^2$  and  $t \gg \epsilon_e / \sigma_s$ .

The steady state response of the secondary field can be written as follows

$$H(s) = C \left( \frac{1}{\alpha^2} - \frac{\cosh(\alpha)}{\alpha \sinh(\alpha)} + \frac{1}{3} \right) H_0(s),$$

where  $C$  is a constant. The transient field is given by a Fourier Integral as indicated in [77, 79]. A complete study has been done in [5, 38, 77].

We now consider the transient response for the permeable conducting sphere whose permeability  $\mu$  is known. In this case our coefficient  $a_0$  becomes

$$a_0 = -\frac{1}{2} H_0 \rho^3 (\epsilon_e s)^2 \chi(s),$$

where the induced magnetic dipole moment factor  $\chi(s)$  is defined as

$$\chi(s) = -\frac{(2\mu_r + 1)[\sinh(\alpha) - \alpha \cosh(\alpha)] + \alpha^2 \sinh(\alpha)}{(\mu_r - 1)[\sinh(\alpha) - \alpha \cosh(\alpha)] - \alpha^2 \sinh(\alpha)},$$

where  $\alpha = \beta \sqrt{s}$  and  $\beta = (\sigma_s \mu_s)^{1/2}$ . Let us remark that in this case the expression of  $\alpha$  is identical to the one used for the definition of the coefficients  $a_0$  and  $b_0$ .

Using the inverse Laplace transform<sup>1</sup>, we can calculate the step-function response  $h(t)$  directly from the contour integral

$$h(t) = \mathcal{L}^{-1} \left\{ \frac{\chi(s)}{s} \right\} = -\frac{1}{2\pi i} \int_{c-i\infty}^{c+i\infty} \frac{F(s)}{G(s)} e^{st} ds, \quad (4.5)$$

where

$$F(s) = (2\mu_r + 1)[\sinh(\beta \sqrt{s}) - (\beta \sqrt{s}) \cosh(\beta \sqrt{s})] + \beta^2 s \sinh(\beta \sqrt{s}) \quad (4.6)$$

<sup>1</sup>The Laplace transform is a frequency-domain approach for continuous time signals irrespective of whether the system is stable or unstable. The Laplace transform of a function  $f(t)$ , defined for all real numbers  $t \geq 0$ , is the function  $\mathcal{L}(s)$ , which is a unilateral transform defined by

$$\mathcal{L}(s) = \int_0^{\infty} e^{-st} f(t) dt,$$

where  $s$  is a complex number frequency parameter.

and

$$G(s) = s[(\mu_r - 1)(\sinh(\beta\sqrt{s}) - (\beta\sqrt{s}) \cosh(\beta\sqrt{s})) - \beta^2 s \sinh(\beta\sqrt{s})]. \quad (4.7)$$

The only singularities of the integral in equation (4.5) are poles which occur in the  $s$  plane where  $G(s) = 0$ . It is evident that these poles are at  $s = 0$  and at  $s = s_n$  (for  $n = 1, 2, 3, \dots$ ) on the negative real axis. Setting  $\beta s_n^{1/2} = i\delta_n$ , we easily find that

$$\tan(\delta_n) = \frac{(\mu_r - 1)\delta_n}{\mu_r - 1 + \delta_n^2},$$

which yield real solutions for  $\delta_n$ .

From (4.6) and from (4.7), we can obtain a series representation for the function  $h(t)$  of equation (4.5),

$$h(t) = \sum_{n=1}^{\infty} \frac{12\pi\rho}{\mu_0\sigma} \frac{\delta_n^2}{(\mu_r + 2)(\mu_r - 1) + \delta_n^2} e^{-\frac{\delta_n^2}{\rho^2\mu\sigma}t}. \quad (4.8)$$

## 4.2 A nonlinear approximation problem

Let us write the step-function response (4.8) as

$$h(t) = \sum_{n=1}^{\infty} c_n e^{-d_n t}, \quad t > 0 \quad (4.9)$$

where

- $d_n = \frac{\delta_n^2}{\rho^2\mu\sigma}$  with  $\delta_n$  the  $n$ th zero of the following equation

$$\tan x = \frac{(\mu_r - 1)x}{(\mu_r - 1) + x^2}. \quad (4.10)$$

- $c_n = \frac{12\pi\rho}{\mu_0\sigma} \frac{\delta_n^2}{(\mu_r + 2)(\mu_r - 1) + \delta_n^2}$ .

and let us assume at first check the integer  $N$  such that

$$h(t) = \sum_{n=1}^{\infty} c_n e^{-d_n t} \simeq \sum_{n=1}^N c_n e^{-d_n t}.$$

To this end, we have investigated the behavior of the sum  $h(t)$  for some metallic materials whose values of their electrical conductivity and

the magnetic permeability are reported in Table 4.1. We can find more information about metallic materials in [8].

Metallic material	$\sigma$ (S/m)	$\mu$ (H/m)
Aluminum	$3.50 \times 10^7$	$1.256665 \times 10^{-6}$
Carbon Steel	$6.99 \times 10^6$	$1.26 \times 10^{-4}$
Ferritic stainless steel	$1.45 \times 10^6$	$2 \times 10^{-3}$
Iron	$1.00 \times 10^7$	$6.3 \times 10^{-3}$

**Table 4.1:** Electrical conductivity  $\sigma$  and magnetic permeability  $\mu$  of some metallic materials.

We represent in Fig. 4.2 and Fig. 4.3 the sum  $h(t)$  for each material and for  $N = 10, 100$ , while in Fig. 4.4 we display the behavior of  $h(t)$  as a function of  $N$  for each material and for  $t = 2 \times 10^{-6}$ .

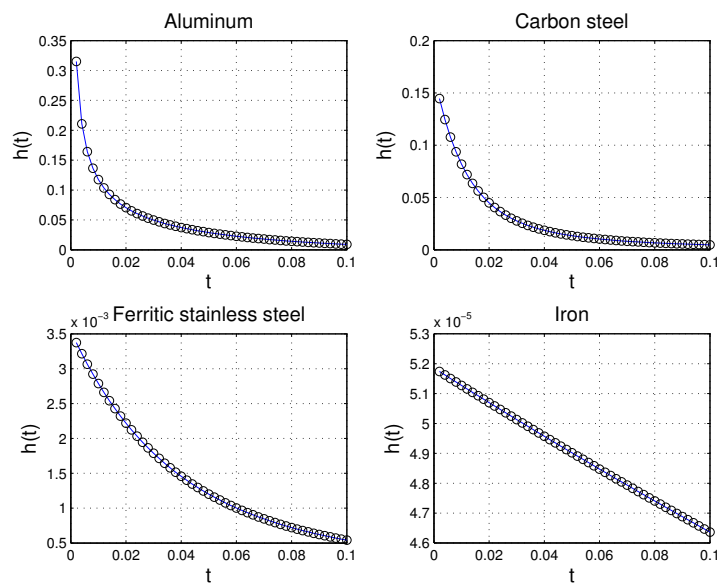


**Figure 4.2:** The behavior of the sum  $h(t)$  for different materials for  $N = 10$ .

4. Time domain electromagnetic (TDEM) response of a conductive permeable sphere

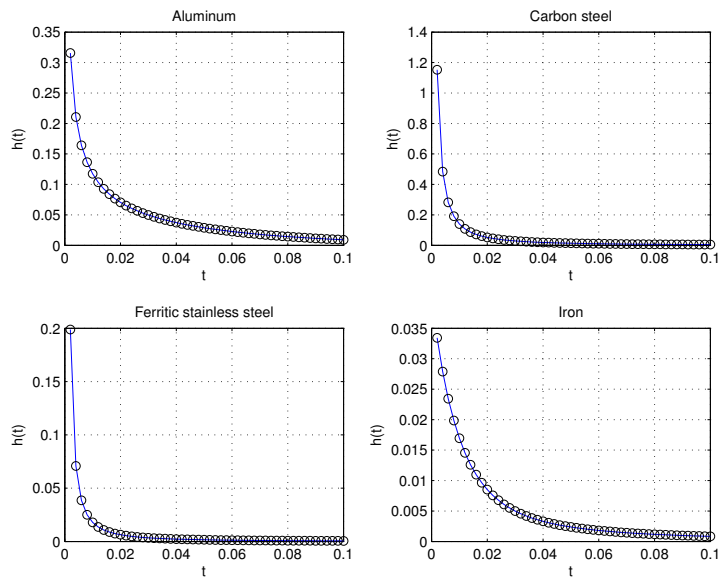


**Figure 4.3:** The behavior of the sum  $h(t)$  for different materials for  $N = 100$ .

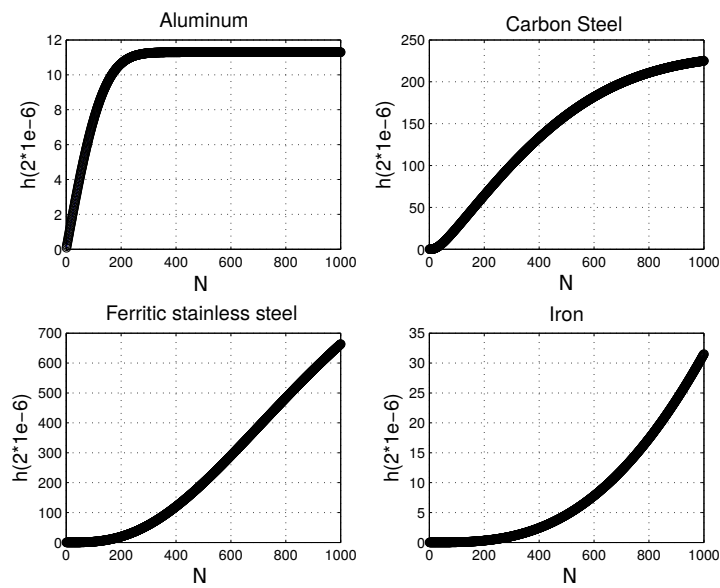


**Figure 4.4:** The behavior of the sum as function of  $N$  for different materials at  $t = 2 \times 10^{-6}$ .

From Fig. 4.4 we can deduce the value of  $N$  for our sum. For example, for the aluminum and for the carbon steel, it would make sense to fix  $N = 400$  and  $N = 1000$ , respectively, since if the sum has a number of terms greater than this value of  $N$ ,  $h(t)$  takes the same values. However, for Ferritic stainless steel and Iron we would need to plot the step-function  $h(t)$  for  $N$  bigger than 1000 in order to be able to choose  $N$  for the sum.

Now, we assume that we know the value of the function (4.9) in  $2N$  equispaced points  $t_j = jh$ ,  $j = 1, 2, 3, \dots$ . Our aim is to identify

1. the coefficients  $\{d_n\}_{n=1}^N$ ,
2. the parameters  $\{c_n\}_{n=1}^N$  and to recover  $\rho$ ,  $\sigma$  and  $\mu$ .

The two mostly used methods are the Prony-like (or polynomial) methods and the matrix-pencil methods. The first one are based on the paper by G. de Prony [58] who was the first to investigate this problem. The method is principally based on the solution of two linear systems characterized by a Hankel and a Vandermonde matrix, respectively. The first system furnishes the coefficients of a polynomial (the so-called Prony polynomial) whose roots  $z_n$  allow one to determine the parameters  $d_n$  (being  $z_n = e^{d_n}$ ), while the second system provides the coefficients  $c_n$ . Several extensions have been proposed (see [1, 70, 71, 83], and more recently [54, 55, 56, 57]) to apply this polynomial method also to the case where  $N$  is only approximately known or the data are affected by noise. The matrix-pencil technique has been developed more recently [19, 35]. As the Prony-like methods, one recovers the coefficients  $c_n$  by solving a Vandermonde system but the computation of the parameters  $d_n$  is reduced to only one step; see [64]. In fact, the matrix-pencil method allows one to estimate the zeros of the Prony polynomials and then  $d_n$  without passing through the computation of its coefficients. This is the main difference with the Prony-like methods and it makes this kind of method more computationally efficient.

Hereafter, we describe the well-known Prony method which is the technique we have applied until now to solve our problem. In the future, we will apply also the matrix-pencil method to our problem.

### Prony method

We rewrite

$$h(t_j) = \sum_{n=1}^N c_n e^{-d_n j h} \quad \Longrightarrow \quad h(j) = \sum_{n=1}^N c_n z_n^j, \quad z_n = e^{-d_n h},$$

and we see it as the general solution of a homogeneous linear difference equation of order  $N$  of the type

$$\sum_{k=0}^{N-1} p_k h(k+m) = -h(m+n), \quad m = 0, 1, \dots, N-1,$$

where  $p_k$  are the coefficients of the *Prony polynomial*

$$P(z) = \prod_{n=1}^N (z - z_n)^{m_n} = \sum_{k=0}^{N-1} p_k z^k, \quad p_N \equiv 1.$$

At this point, let us recover at first the zeros  $\{z_n\}_{n=1}^N$  and then the coefficients.

1. Computation of  $\{z_n\}_{n=1}^N$ .

- Identify the coefficients of the Prony polynomial by solving the following system whose matrix of coefficients is a Hankel matrix.

$$\begin{pmatrix} h(1) & h(2) & h(3) & \dots & h(n-1) \\ h(2) & h(3) & h(4) & \dots & h(n) \\ h(3) & h(4) & h(5) & \dots & h(n+1) \\ \dots & \dots & \dots & \ddots & \vdots \\ h(n-2) & h(n-1) & h(n) & \dots & h(2n-3) \\ h(n-1) & h(n) & h(n+1) & \dots & h(2n-2) \end{pmatrix} \begin{pmatrix} p_0 \\ p_1 \\ p_2 \\ \vdots \\ p_{n-2} \\ p_{n-1} \end{pmatrix} = \begin{pmatrix} -h(n) \\ -h(n+1) \\ -h(n+2) \\ \vdots \\ -h(2n-2) \\ -h(2n-1) \end{pmatrix}.$$

- Once we solve this system, by computing the eigenvalues of the following Companion matrix

$$C = \begin{pmatrix} 0 & 0 & 0 & \dots & -p_0 \\ 1 & 0 & 0 & \dots & -p_1 \\ 0 & 1 & 0 & \dots & -p_2 \\ 0 & 0 & 1 & \ddots & \vdots \\ 0 & 0 & \dots & 1 & -p_{n-1} \end{pmatrix},$$

we can recover the zeros  $z_n$  and then  $d_n = -\frac{\log z_n}{h}$ .

2. Computation of  $\{c_n\}_{n=1}^N$ .

The coefficients  $\{c_n\}$  are the solution of the following system having

a Vandermonde matrix of coefficients.

$$\begin{pmatrix} z_1^0 & z_2^0 & z_3^0 & \dots & z_n^0 \\ z_1^1 & z_2^1 & z_3^1 & \dots & z_n^1 \\ z_1^2 & z_2^2 & z_3^2 & \dots & z_n^2 \\ \dots & \dots & \dots & \ddots & \vdots \\ z_1^{n-1} & z_2^{n-1} & z_3^{n-1} & \dots & z_n^{n-1} \\ z_1^n & z_2^n & z_3^n & \dots & z_n^n \end{pmatrix} \begin{pmatrix} c_1 \\ c_2 \\ c_3 \\ \vdots \\ c_{n-1} \\ c_n \end{pmatrix} = \begin{pmatrix} -h(n) \\ -h(n+1) \\ -h(n+2) \\ \vdots \\ -h(2n-2) \\ -h(2n-1) \end{pmatrix}.$$

Once we get the parameters  $d_n$  and  $c_n$ , we can obtain the value of  $\sigma$  and  $\rho$  by solving

$$\begin{cases} d_n = \frac{\delta_n^2}{\rho^2 \mu \sigma}, \\ c_n = \frac{12\pi\rho}{\mu_0\sigma} \frac{\delta_n^2}{(\mu_r + 2)(\mu_r - 1) + \delta_n^2}. \end{cases}$$

In the following section we will show some numerical results about it.

### 4.3 Some numerical results

For our first numerical experiments we have assumed that the sphere is made of a certain material and we evaluate the step–function response

$$h(t) = \sum_{n=1}^N c_n e^{-d_n t}, \quad t > 0$$

in some points.

In order to find  $\delta_n \in (n\pi, n\pi + \frac{\pi}{2})$ , which are the zeros of (4.10), we apply the Newton method (see Section 1.1.2). However the presence of the asymptotes of the tangent function make unstable the method, in the sense that the zeros of (4.10) could be sometimes very close to them. This happens when the right–hand side of equation (4.10) is approaching to its maximal value, which is attained at  $x = \sqrt{\mu_r - 1}$ . In Fig. 4.5 we depict the behavior of the tangent function and the function  $g(x) = \frac{(\mu_r - 1)x}{(\mu_r - 1) + x^2}$  for different values of  $\mu_r$  and we can see, together with an empirical research, that if  $n\pi + \frac{\pi}{2} \leq 3\sqrt{\mu_r - 1}$ , the root of the equation is close to the asymptote giving place to an overflow.

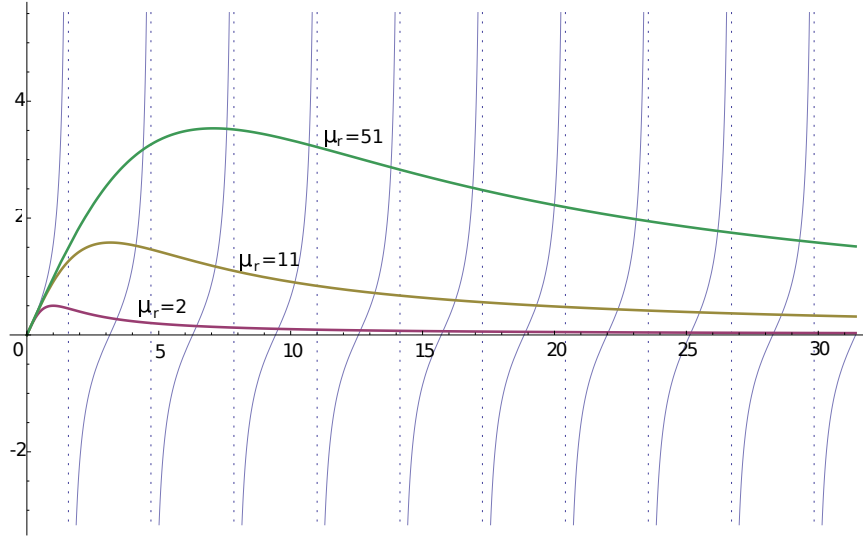


**Figure 4.5:** Plot of  $f(x) = \tan x$  (blue line) and  $g(x) = \frac{(\mu_r - 1)x}{(\mu_r - 1) + x^2}$  for  $\mu_r - 1 = 1, 10, 50$  (pink, yellow and green lines, respectively).

With the aim of overcoming these difficulties we solve the inverse equation of (4.10) when  $n\pi + \frac{\pi}{2} \leq 3\sqrt{\mu_r - 1}$ , that is:

- If  $n\pi + \frac{\pi}{2} \leq 3\sqrt{\mu_r - 1}$  we solve the equation

$$\cot x = \frac{1}{x} + \frac{x}{\mu_r - 1}.$$

- If  $n\pi + \frac{\pi}{2} > \sqrt{\mu_r - 1}$  we solve

$$\tan x = \frac{(\mu_r - 1)x}{(\mu_r - 1) + x^2}.$$

In Fig. 4.6 we show the behavior of  $\delta_n - n\pi$  as a function of  $n$  for  $n = 1, \dots, 100$  and for different values of the relative permeability,  $\mu_r = 1, 10, 50, 100, 200, 5100$ . We can see that for small values of  $\mu_r$ ,  $\delta_n - n\pi$  tends to zero while for bigger values of the relative permeability,  $\delta_n - n\pi$  tends to  $\frac{\pi}{2}$ .

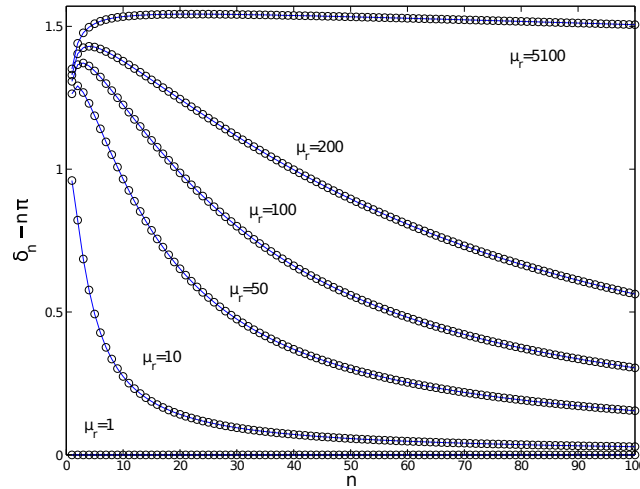


**Figure 4.6:**  $\delta_n$  as a function of  $n$  and parametrically as a function of the relative permeability  $\mu_r$ .

For the reconstruction of  $\sigma$  and  $\mu$ , we need to know, as we said at the beginning of this section, the values of  $h(t)$  in some points. To generate this synthetic data set, we choose a priori  $\sigma$  and  $\mu$  and then, once we compute the values of  $h(t)$ , we determine both the electrical conductivity and the magnetic permeability by the Prony method. In Table 4.1 we reported the electrical conductivity and the magnetic permeability of some metallic materials.

$d_n$	$\tilde{d}_n$	$\epsilon_n$
2.243954973008462e+01	2.243954973008579e+01	5.20e-14
8.975789563175007e+01	8.975789563180739e+01	6.38e-13
2.019551388008130e+02	2.019551388187708e+02	8.89e-11
3.590312792374512e+02	3.590312827371441e+02	9.74e-09
5.609863169416867e+02	5.609866405940118e+02	5.76e-07
8.078202519135250e+02	8.078279136080553e+02	9.48e-06
1.099533084152968e+03	1.098811780829547e+03	6.56e-04
1.436124813660015e+03	1.385496497352069e+03	3.52e-02
1.817595440434669e+03	1.597756993664808e+03	1.20e-01
2.243944964476928e+03	2.107856078732385e+03	6.06e-02

**Table 4.2:** Comparison of the exact  $d_n$  and its approximation  $\tilde{d}_n$ , and the corresponding relative error  $\epsilon_n$  for  $N = 10$ .

We apply the Prony method to the sum (4.9) in the aluminum case. As we said before, from the graph of the aluminum in Fig. 4.4, we can deduce that an acceptable value of  $N$  to reconstruct all the coefficients of the sum would be 400.

Starting with  $N = 10$ , we report in Table 4.2 the exact value of the coefficients vector  $d_n$  and its approximation  $\tilde{d}_n$  with the corresponding relative error. We can see that there is an error of order  $10^{-1}$ , which makes us think that the reconstruction of the parameters is not satisfactory. This happens because of the ill-conditioning of the involved matrices in Prony's method since they are Hankel and Vandermonde matrices. We see in Fig. 4.7 the representation of their singular values.

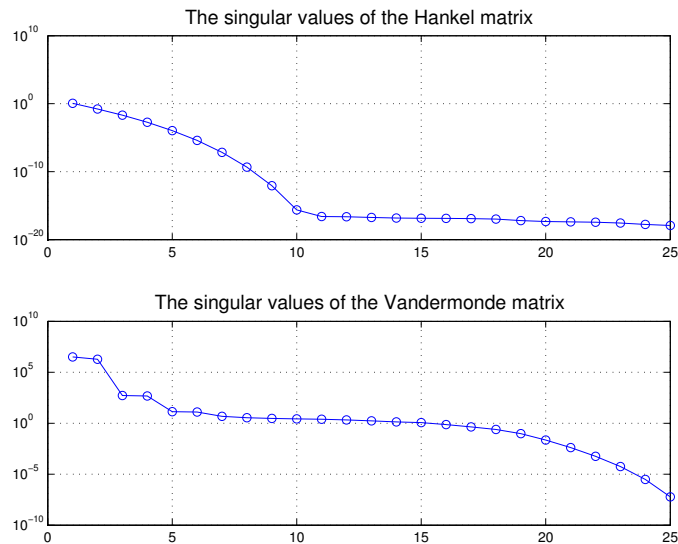


Figure 4.7: The singular values of the involved matrices.

We just saw that the reconstruction of the coefficients is not optimal for  $N = 10$ . If  $N = 400$  the dimensions of the matrices would increase and the condition number would be higher, so applying the Prony method for  $N = 400$  does not make sense. In order to address these difficulties, we are currently working on the implementation of a strategy based on the matrix-pencil method [14].

## Summary conclusion and further work

We have seen along this thesis diverse applications of inversion procedures to solve different problems in Geophysics. In this last section, we write some conclusions about each problem and some future work we plan to do.

For the **linear model** (see Chapter 2) we recover the electrical conductivity of the soil with respect to depth approximating a priori the conductivity by either a piecewise constant function or a linear spline. From the forward linear model we generate synthetic data set by the Gauss–Kronrod quadrature, and then we apply both the TSVD and the Tikhonov regularization to solve the ill–conditioned inverse problem. Comparing the results reported in the tables of Chapter 2, we conclude that, in general the TSVD is comparable to the Tikhonov regularization. In the near future, in order to compare our results we want to introduce other numerical methods based on the approximation of the conductivity by the Lagrange polynomials or by other polynomials which allow us to use equidistant nodes.

For the **nonlinear model** (see Chapter 3) we have proposed a regularized inversion method to reconstruct the electrical conductivity and the magnetic permeability of the soil with respect to depth, starting from electromagnetic data collected by a multi–frequency Ground Conductivity Meter (GCM). We applied a damped Gauss–Newton method with either the TSVD and the TGSVD. This inversion procedure is based on the low–rank approximation of the Jacobian of the nonlinear model, which depends on a relaxation parameter and a regularization parameter chosen by automatic procedures. Our numerical experiments have shown that the algorithm produces reasonable results for both the electrical conductivity and the magnetic permeability choosing a noise consistent with real situations. Until now, we have recover the electrical conductivity assuming that the magnetic permeability is known, and vice versa. In the future, we want to write an algorithm to detect both the electrical conductivity and the magnetic permeability at the same time.

The case of the **conducting sphere** (see Chapter 4) involves a work in progress which handles the estimation of the magnetic permeability,

the conductivity and the radius of a sphere imbedded in a uniform time-varying magnetic field via exponential sums. Until now, we have studied the behavior of the step-function response and, now we are trying to apply the Prony method or some modification of it. We also would like to apply the Matrix-pencil method to our sum.

## Bibliography

- [1] G. BEYLKIN AND L. MONZÓN, *On approximation of functions by exponential sums*, Applied and Computational Harmonic Analysis, 19 (2005), pp. 17–48.
- [2] A. BJÖRCK, *Numerical Methods for Least Squares Problems*, SIAM, Philadelphia, 1996.
- [3] J. BOAGA, M. GHINASSI, A. D’ALPAOS, G. P. DEIDDA, G. RODRIGUEZ, AND G. CASSIANI, *Unravelling the vestiges of ancient meandering channels in tidal landscapes via multi-frequency inversion of Electro–Magnetic data*. Submitted, 2016.
- [4] B. BORCHERS, T. URAM, AND J. HENDRICKX, *Tikhonov regularization of electrical conductivity depth profiles in field soils*, Soil Science Society of America Journal, 61 (1997), pp. 1004–1009.
- [5] G. A. CAMPBELL AND R. M. FOSTER, *Bell System Technical Journal*, (1929), p. 639.
- [6] G. CASSIANI, N. URSINO, R. DEIANA, G. VIGNOLI, J. BOAGA, M. ROSSI, M. T. PERRI, M. BLASCHEK, R. DUTTMANN, S. MEYER, R. LUDWIG, A. SODDU, P. DIETRICH, AND U. WERBAN, *Noninvasive monitoring of soil static characteristics and dynamic states: a case study highlighting vegetation effects on agricultural land*, Vadose Zone Journal, 11 (2012).
- [7] D. COLTON AND R. KRESS, *Inverse Acoustic and Electromagnetic Scattering Theory*, Springer-Verlag, New York, 2013.
- [8] A. I. M. P. D. COMMITTEE, *Electrical and Magnetic Properties of Metals*, Ohio, 2000.
- [9] P. CRAVEN AND G. WAHBA, *Smoothing noisy data with spline functions: estimating the correct degree of smoothing by the method of Generalized Cross Validation*, Numerische Mathematik, 31 (1979), pp. 377–403.
- [10] P. DEBYE, *Annalen der Physik*, (1909), p. 57.

- [11] G. DEIDDA, E. BONOMI, AND C. MANZI, *Inversion of electrical conductivity data with Tikhonov regularization approach: some considerations*, *Annals for Geophysics*, 46 (2003), pp. 549–558.
- [12] G. DEIDDA, C. FENU, AND G. RODRIGUEZ, *Regularized solution of a non-linear problem in electromagnetic sounding*, *Inverse Problems*, 30 (2014).
- [13] P. DIAZ DE ALBA, L. FERMO, AND G. RODRIGUEZ, *A collocation method for first kind integral equations applied to Geophysics*. In progress.
- [14] P. DIAZ DE ALBA, L. FERMO, AND G. RODRIGUEZ, *Recovering the electrical conductivity and the magnetic permeability of a conductive permeable sphere*. In progress.
- [15] P. DIAZ DE ALBA AND G. RODRIGUEZ, *Regularized inversion of multi-frequency EM data in Geophysical applications*. *Book Trends in Differential equations and Applications*, Springer, Switzerland, 2016.
- [16] P. DIAZ DE ALBA AND G. RODRIGUEZ, *Identifying the magnetic permeability in multi-frequency FDEM data inversion*. Submitted, 2017.
- [17] H. ENGL, M. HANKE, AND A. NEUBAUER, *Regularization of Inverse Problems*, Kluwer, Dordrecht, 1996.
- [18] C. ESTATICO, M. PASTORINO, AND A. RANDAZZO, *A Novel Microwave Imaging Approach Based on Regularization in  $L^p$  Banach Spaces*, *IEEE TRANSACTIONS ON ANTENNAS AND PROPAGATION*, 60 (2012), pp. 3373–3381.
- [19] L. FERMO, C. VAN DER MEE, AND S. SEATZU, *Parameter estimation of monomial-exponential sums*, *Electronic Transactions on Numerical Analysis (ETNA)*, 41 (2014), pp. 249–261.
- [20] W. GAUTSCHI AND S. E. NOTARIS, *Newton's Method and Gauss-Kronrod Quadrature*, vol. 85, Springer, West Lafayette, IN., U.S.A, 1988.
- [21] R. GEBBERS, E. LÜCK, AND K. HEIL, *Depth sounding with the EM38-detection of soil layering by inversion of apparent electrical conductivity measurements*, *Precision Agriculture '07*, (2007), pp. 95–102.
- [22] G. H. GOLUB, M. HEATH, AND G. WAHBA, *Generalized cross-validation as a method for choosing a good ridge parameter*, *Technometrics*, 21 (1979), pp. 215–223.

- 
- [23] I. S. GRADSHTEYN AND I. M. RYZHIK, *Table of integrals, series and products*, Academic Press, New York, London, Toronto, Sydney, San Francisco, 1980.
- [24] J. P. GREENHOUSE AND D. D. SLAINE, *The use of reconnaissance electromagnetic methods to map contaminant migration*, *Groundwater Monitoring & Remediation*, 3 (1983), pp. 47–59.
- [25] J. HADAMARD, *Lectures on Cauchy's Problem in Linear Partial Differential Equations*, Yale University Press, New Haven, 1923.
- [26] M. HANKE, *Limitations of the L-curve method in ill-posed problems*, *BIT*, 36 (1996), pp. 287–301.
- [27] P. C. HANSEN, *The truncated SVD as a method for regularization*, *BIT*, 27 (1987), pp. 543–553.
- [28] P. C. HANSEN, *Rank-Deficient and Discrete Ill-Posed Problems*, SIAM, Philadelphia, 1998.
- [29] P. C. HANSEN, *Regularization Tools: version 4.0 for Matlab 7.3*, *Numerical Algorithms*, 46 (2007), pp. 189–194.
- [30] P. C. HANSEN, T. K. JENSEN, AND G. RODRIGUEZ, *An adaptive pruning algorithm for the discrete L-curve criterion*, *Journal of Computational and Applied Mathematics*, 198 (2007), pp. 483–492.
- [31] P. C. HANSEN, J. G. NAGY, AND D. P. O'LEARY, *Deblurring Images. Matrices, Spectra, and Filtering*, SIAM, Philadelphia, 2006.
- [32] P. C. HANSEN AND D. P. O'LEARY, *The use of the L-curve in the regularization of discrete ill-posed problems*, *SIAM Journal on Scientific Computing*, 14 (1993), pp. 1487–1503.
- [33] J. M. H. HENDRICKX, B. BORCHERS, D. L. CORWIN, S. M. LESCH, A. C. HILGENDORF, AND J. SCHLUE, *Inversion of soil conductivity profiles from electromagnetic induction measurements: Theory and experimental verification*, *Soil Science Society of America Journal*, 66 (2002), pp. 673–685.
- [34] M. E. HOCHSTENBACH, L. REICHEL, AND G. RODRIGUEZ, *Regularization parameter determination for discrete ill-posed problems*, *Journal of Computational and Applied Mathematics*, 273 (2015), pp. 132–149.
- [35] Y. HUA AND T. K. SARKAR, *Matrix pencil method for estimating parameters of exponentially damped/undamped sinusoids in noise*, *IEEE Trans. Acoust. Speech Signal Process.*, 38 (1990), pp. 814–824.

- [36] H. HUANG, B. SANFILIPPO, A. OREN, AND I. J. WON, *Coaxial coil towed EMI sensor array for uxo detection and characterization*, *Journal of Applied Geophysics*, 61 (2007), pp. 217–226.
- [37] H. HUANG AND I. J. WON, *Automated anomaly picking from broadband electromagnetic data in an unexploded ordnance (UXO) survey*, *Geophysics*, 68 (2003), pp. 1870–1876.
- [38] E. JAHNKE AND F. EMDE, *Tables of functions*, Dover, 1945.
- [39] M. L. KRASSNOV, A. I. KISELEV, AND G. I. MAKARENKO, *Equazioni Integrali*, Edizioni Mir, 1983.
- [40] R. KRESS, *Numerical Analysis*, Springer, 1998.
- [41] R. KRESS, *Linear Integral Equation*, Springer, 1999.
- [42] E. LASCANO, P. MARTINELLI, AND A. OSELLA, *EMI data from an archaeological resistive target revisited*, *Near Surface Geophysics*, 4 (2006), pp. 395–400.
- [43] S. M. LESCH, D. J. STRAUSS, AND J. D. RHOADES, *Spatial prediction of soil salinity using electromagnetic induction techniques: 1. Statistical prediction models: A comparison of multiple linear regression and cokriging*, *Water Resources Research*, 31 (1995), pp. 373–386.
- [44] H. W. MARCH, *Bulletin of the American Mathematical Society*, 35 (1929), p. 455.
- [45] P. MARTINELLI AND M. C. DUPLAÁ, *Laterally filtered 1D inversions of small-loop, frequency-domain EMI data from a chemical waste site*, *Geophysics*, 73 (2008), pp. F143–F149.
- [46] J. D. MCNEILL, *Electromagnetic terrain conductivity measurement at low induction numbers*, Technical Report TN-6 Geonics Limited, 1980.
- [47] V. A. MOROZOV, *The choice of parameter when solving functional equations by regularization*, *Doklady Akademii Nauk SSSR*, 175 (1962), pp. 1225–1228.
- [48] V. A. MOROZOV, *Methods for solving Incorrectly Posed Problems*, Springer Verlag, New York, NY, 1984.
- [49] J. M. ORTEGA AND W. C. RHEINBOLDT, *Iterative Solution of Nonlinear Equations in Several Variables*, Academic Press, New York, 1970.

- 
- [50] A. OSELLA, M. DE LA VEGA, AND E. LASCANO, *3D electrical imaging of an archaeological site using electrical and electromagnetic methods*, *Geophysics*, 70 (2005), pp. G101–G107.
- [51] C. C. PAIGE AND M. A. SAUNDERS, *Toward a generalized singular value decomposition*, *SIAM Journal on Numerical Analysis*, 1 (1975), pp. 24–76.
- [52] J. G. PAINE, *Determining salinization extent, identifying salinity sources, and estimating chloride mass using surface, borehole, and airborne electromagnetic induction methods*, *Water Resources Research*, 39 (2003).
- [53] L. PELLERIN, *Applications of electrical and electromagnetic methods for environmental and geotechnical investigations*, *Surveys in Geophysics*, 23 (2002), pp. 101–132.
- [54] T. PETER AND G. PLONKA, *A generalized prony method for reconstruction of sparse sums of eigenfunctions of linear operators*, *Inverse Problems*, 29 (2013).
- [55] D. POTTS AND M. TASCHE, *Parameter estimation for exponential sums by approximate prony method*, *Signal Processing*, 90 (2010), pp. 1631–1642.
- [56] D. POTTS AND M. TASCHE, *Nonlinear approximation by sums of nonincreasing exponentials*, *Applied Analysis*, 90 (2011), pp. 609–626.
- [57] D. POTTS AND M. TASCHE, *Parameter estimation for nonincreasing exponential sums by Prony-like methods*, *Linear Algebra and Its Applications*, 439 (2013), pp. 1024–1039.
- [58] B. PRONY, *Essai expérimental et analytique sur les lois de la Dilatabilité des fluides élastiques et sur celles de la Force expansive de la vapeur de l’eau et de la vapeur de l’alkool, à différentes températures.*, *J. l’École Polytech.*, 18 (1981), pp. 398–405.
- [59] H. RAMSIN AND P. A. WEDIN, *A comparison of some algorithms for the nonlinear least squares problem.*, *BIT Numerical Mathematics*, 17 (1977), pp. 72–90.
- [60] L. REICHEL AND G. RODRIGUEZ, *Old and new parameter choice rules for discrete ill-posed problems*, *Numerical Algorithms*, 63 (2013), pp. 65–87.
- [61] G. RODRIGUEZ AND S. SEATZU, *Numerical solution of the finite moment problem in a reproducing kernel hilbert space*, *Journal of Computational and Applied Mathematics*, 33 (1990), pp. 233–244.

- [62] G. RODRIGUEZ AND D. THEIS, *An algorithm for estimating the optimal regularization parameter by the L-curve*, Rendiconti di Matematica, Serie VII, 25 (2005), pp. 69–84.
- [63] L. SAMBUELLI, S. LEGGIERI, C. CALZONI, AND C. PORPORATO, *Study of riverine deposits using electromagnetic methods at a low induction number*, Geophysics, 72 (2007), pp. B113–B120.
- [64] T. K. SARKAR AND O. PEREIRA, *Using the matrix pencil method to estimate the parameters of a sum of complex exponentials*, IEEE Trans. Antennas and Propagation, 37 (1995), pp. 48–55.
- [65] M. H. SCHULTZ, *Spline Analysis*, Pearson Education, Limited, University of Michigan, 1972.
- [66] D. D. SNYDER, SCOTTMACINNES, S. URQUHART, AND K. L. ZONGE, *UXO classification using characteristic modes of the broadband electromagnetic induction response*, Zonge International. Technology Development, (2000).
- [67] B. R. SPIES AND F. C. FRISCHKNECHT, *Electromagnetic sounding*, Electromagnetic Methods in Applied Geophysics. Volume 2: Application, Tulsa, OK, 1991.
- [68] J. THIESSON, M. DABAS, AND S. FLAGEUL, *Detection of resistive features using towed Slingram electromagnetic induction instruments*, Archaeological Prospection, 16 (2009), pp. 103–109.
- [69] L. N. TREFETHEN AND D. BAU, *Numerical linear algebra*, vol. 50, Siam, 1997.
- [70] M. L. VAN BLARICUM AND R. MITTRA, *A technique for extracting the poles and residues of a system directly from its transient response*, IEEE Trans. Antennas and Propagation, 23 (1975), pp. 777–781.
- [71] M. L. VAN BLARICUM AND R. MITTRA, *Problems and solutions associated with prony's method for precessing transient data*, IEEE Trans. Antennas and Propagation, 26 (1978), pp. 174–182.
- [72] C. F. VAN LOAN, *Generalizing the singular value decomposition*, SIAM Journal on Numerical Analysis, 13 (1976), pp. 76–83.
- [73] C. R. VOGEL, *Non-convergence of the L-curve regularization parameter selction method*, Inverse Problems, 12 (1996).
- [74] C. R. VOGEL AND N. E. OMAN, *Iterative methods for total variation denoising*, Siam JSC, (1986), pp. 227–238.

- 
- [75] G. WAHBA, *Practical approximate solutions to linear operator equations when the data are noisy*, SIAM Journal on Numerical Analysis, 14 (1977), pp. 651–667.
- [76] G. WAHBA, *Spline Models for Observational Data*, CBMS-NSF Regional Conference Series in Applied Mathematics, Vol. 59, SIAM, Philadelphia, PA, 1990.
- [77] J. R. WAIT, *A conducting sphere in a time varying magnetic field*, Society of Exploration Geophysicists, 16 (1951), pp. 666–672.
- [78] J. R. WAIT, *Geo-Electromagnetism*, New York: Academic, New York, NY, 1982.
- [79] J. R. WAIT AND K. P. SPIES, *Quasi static transient response of a conducting permeable sphere*, Society of Exploration Geophysicists, 34 (1969), pp. 789–792.
- [80] S. H. WARD, *A method for measuring the electrical conductivity of diamond drill core specimens*, vol. 18, Geophysics, 1953.
- [81] S. H. WARD AND G. W. HOHMANN, *Electromagnetic theory for geophysical applications. (In Electromagnetic Methods in Applied Geophysics)*, Society of Exploration Geophysicists, Tulsa, OK, 1987.
- [82] G. N. WATSON, *Theory of Bessel Functions*, Ed. Cambridge, 1944.
- [83] L. WEISS AND R. N. McDONOUGH, *Prony's method, Z-transforms and Padé approximations*, vol. 5, 1963.
- [84] R. YAO AND J. YANG, *Quantitative evaluation of soil salinity and its spatial distribution using electromagnetic induction method*, Agricultural Water Management, 97 (2010), pp. 1961–1970.